

# **Irradiation assisted corrosion of cast A360.1 and additively manufactured AlSi10Mg aluminum alloys in seawater environments.**

by

Victor Udochukwu Okoro

PGD., University of Lagos, 2014

B.Sc., Abia State University, 2009

A thesis Submitted in Partial Fulfillment of the Requirement for the Degree of

## **Master of Science in Engineering**

in the Graduate Academic Unit of Chemical Engineering

**Supervisor(s):** Derek H. Lister, PhD., Chemical Engineering.  
Mohsen Mohammadi, PhD., Mechanical Engineering.

**Examining Board:** Brian Lowry, PhD., Chemical Engineering, Chair.  
Guida Bendrich, PhD., Chemical Engineering.  
Huining Xiao, PhD., Chemical Engineering.  
Anna Ignaszak, PhD., Chemistry.

This thesis is accepted by the  
Dean of Graduate Studies

THE UNIVERSITY OF NEW BRUNSWICK

January 2021

© Victor Udochukwu Okoro, 2021

## ABSTRACT

This thesis seeks to compare the effects of irradiation in seawater solution on the corrosion of aluminum alloys produced using casting technique and additive manufacturing. Alloys of aluminum have been deployed as one of the basic materials (such as electrical insulation, scaffolding, and thermal columns) in the containment building of nuclear-powered systems. Thus, they are exposed to various ionizing radiation degrees, which tends to affect their corrosion behavior. The aluminum samples were irradiated with a gamma-ray while at the same time exposed to seawater solution to study the effect of radiation on corrosion. Nuclear irradiation influences the corrosion and surface reactions of metals by altering their properties and/or by changing the composition of the immersed solution.

A gamma-ray from a four (4)  $\mu\text{Ci}$  Co-60 source was transmitted through a 7 mm hole that served as a window into the corrosion test cell used for gravimetric analysis containing seawater at room temperature with a pH of 8.20 without any buffer. This experimental setup allowed radiolysis and corrosion to occur on the sample's surface in contact with the seawater environment. Samples were irradiated for 24, 72, 144, 240 hours. The formation and composition of the oxide were carried out by utilizing scanning electron microscopy (SEM) equipped with energy-dispersive X-ray spectroscopy (EDS), Raman Spectroscopy, and X-Ray Diffraction (XRD) techniques.

Ionizing radiation disintegrates water to create oxidizing ( $\text{OH}$ ,  $\text{O}_2$ ,  $\text{H}_2\text{O}_2$ ) and reducing ( $\text{e}^-$ ,  $\text{H}^*$ , and  $\text{H}_2$ ) chemical species. These radiolysis species react with disintegrated solutes and partake in surface reactions prompting a critical change in the redox condition and may form solid species. Seawater contains various solutes; dissolved solutes' presence

affects the constant state concentration of molecular water radiolysis species by rivaling radical species. In any case, the relative increment noticed comparatively with purified water relies on the concentration of solute and pH.

Weight changes for the Al alloys exposed to seawater solution have been obtained and recorded for 240 hours. The most prominent feature of the results obtained is the difference between the irradiated and the non-irradiated. The irradiated cast A360.1 Al alloy gained weight, while the irradiated additively manufactured (AM) AlSi10Mg lost weight. Similar behavior was experienced in the non-irradiated samples, but the weight changes in radiation presence were more remarkable than those in the absence of radiation. It was observed that the weight changes of irradiated samples increased initially and then leveled off as exposure continued. The irradiated AM samples' standard error measurements appeared much more significant than those of the cast ones.

**Keywords:** Additive manufacturing; Aluminum alloys; Gamma radiation; Corrosion; Microstructure; Gravimetric analysis; Gamma-ray energy spectrum.

## **DEDICATION**

This thesis is dedicated to my lord and personal savior – Jesus Christ, whose love and mercies endures forever. In all, his banner over us is **LOVE**.

Every finish line is the beginning of a whole new race.

## ACKNOWLEDGMENTS

I would like to appreciate my boss and supervisor, Dr. Derek Lister, for everything you have done for me in these past years. You brought me out from the miry clay and set my feet on the solid ground. Words alone are not enough to express my gratitude to you; thank you for all the opportunity you have given to me; I am super grateful.

My co-supervisor, Dr. Mohsen Mohammadi, thank you for all the encouragement and for always being there for me when I needed you most. Working with you these past years has instilled confidence in me and made me believe that you can achieve whatever you set your mind to do. Watching you turn around the MAMCE research group positively is something quite commendable. Thank you for everything, sir. I appreciate it.

My shout out goes out to all my teachers and those that allowed me to teach in their labs these past years. Dr. Guida Bendrich, Dr. Sharifvaghefi SeyyedMajid, Mr. Jamie Miles, and Dr. Wilailak Chanklin.; working with you these past years has helped me in developing confidence in my academic learning and teaching.

I have enjoyed my stay at UNB, and I have learned a lot. My time at UNB has come to an end, so my special appreciation goes out to everyone I have met throughout my UNB journey and all my friends, both distant and close. Special thanks to everyone at UNB nuclear research group and UNB MAMCE research group; it was a pleasant experience sharing the lab space with everyone. It is an experience I will not forget in a hurry. The entire team of the technical staff at the Chemical Engineering department, Adon Briggs, Carl Murdock, is appreciated for all your support and contributions to my entire stay in UNB and my project.

To my parents and siblings who have kept vigil for me all these years as I study in a foreign land a million miles away from home, I am grateful for everything and for believing in me to carry on. Thank you.

Thank you for having me in your space for these past years to my alma mater, the University of New Brunswick. I cherish every experience and knowledge gained while in this climate. You will always be home to me. Furthermore, to the province of New Brunswick, thank you for having me as part of this homely community. You are gratefully appreciated.

## Table of Contents

ABSTRACT .....	ii
DEDICATION .....	iv
ACKNOWLEDGMENTS .....	v
Table of Contents .....	vii
List of Tables.....	xi
List of Figures .....	xii
List of Abbreviations.....	xv
1. Introduction.....	1
2. Literature Review.....	6
2.1 Properties of Aluminum Alloys .....	6
2.1.1 Composition .....	6
2.1.2 Effect of Alloying Additions.....	7
2.1.3 Crystal Structure of Aluminum.....	9
2.1.4 Crystal Structure of Silicon.....	11
2.1.5 Phase Diagram of Al-Si Systems .....	12
2.2 Manufacturing Procedure .....	15
2.2.1 Die Casting.....	16
2.2.2 Additive Manufacturing Systems.....	17
2.2.3 Laser Powder Bed System (LPBF) .....	18
2.3 Aluminum Corrosion.....	19
2.3.1 Passivity of Aluminum.....	19
2.3.2 Pitting Corrosion .....	23
2.4 Radiation and Water Radiolysis .....	26
2.4.1 Radiation Chemistry .....	26

2.5	Irradiation Corrosion .....	30
2.5.1	Irradiated – Corrosion of Aluminum Alloys.....	30
2.6	Application of Research to Nuclear Powered System.....	32
3.	Experimental Techniques and Procedures .....	36
3.1	Materials.....	36
3.2	Irradiation Cell Design .....	37
3.3	Surface Characterisation.....	38
3.3.1	Scanning Electron Microscopy (SEM) with Energy Dispersive X-ray Spectroscopy (EDS).....	38
3.3.2	Raman Spectroscopy.....	39
3.3.3	X-ray Diffraction (XRD).....	39
3.4	Experimental Procedure .....	40
3.4.1	Solution Preparation.....	40
3.4.2	Polishing and Surface Preparation .....	41
3.4.3	Gravimetric (Weight Change) Test.....	41
4.	Result and Discussion .....	45
4.1	Surface Characterization of Aluminum Alloys Before Exposure .....	45
4.1.1	Cast A360.1 Aluminum alloy .....	45
4.1.2	Laser Powder Bed Fusion (LPBF) AlSi10Mg .....	49
4.1.3	Phase Analysis of cast A360.1 Aluminum Alloy.....	53
4.1.4	Phase Analysis of LPBF AlSi10Mg.....	54
4.1.5	Raman Spectrum of cast A360.1 Aluminum Alloy .....	56
4.1.6	Raman Spectrum of LPBF AlSi10Mg Aluminum Alloy.....	57
4.2	Gravimetric Analysis.....	59
4.2.1	Non-Irradiated and Irradiated cast A360.1 Results.....	59



4.2.2	Non-Irradiated and Irradiated LPBF AlSi10Mg Results .....	64
4.3	Corrosion Behaviour of cast A360.1 Exposed in The Absence of Radiation. ..	69
4.3.1	Surface Analyses of Non-Irradiated cast A360.1 After Exposure Using XRD And Raman Spectroscopy. ....	74
4.4	Corrosion Behaviour of Irradiated cast A360.1 Exposed in Artificial Seawater Solution. ....	76
4.4.1	Surface Analyses of Irradiated cast A360.1 After Exposure Using XRD And Raman Spectroscopy. ....	80
4.5	Corrosion Behaviour of LPBF AlSi10Mg After Exposure in the Absence of $\gamma$ - Radiation. ....	83
4.5.1	Surface Analyses of Non-Irradiated LPBF AlSi10Mg After Exposure Using XRD And Raman Spectroscopy. ....	86
4.6	Corrosion Behaviour of LPBF AlSi10Mg After Exposure in the Presence of $\gamma$ - Radiation. ....	88
4.6.1	Surface Analyses of Irradiated LPBF AlSi10Mg After Exposure Using XRD And Raman Spectroscopy. ....	92
4.7	Changes in pH During Corrosion of Aluminum Alloy at Room Temperature .	95
4.8	The Effect of Gamma Radiation on Aluminum Alloy Corrosion at Room Temperature .....	99
4.9	Relevance to Nuclear Powered Systems .....	105
4.9.1	Dose Rate .....	105
4.9.2	Longer Operating Time.....	107
4.9.3	Summary of the Relevance of this Research to Nuclear Powered Systems .....	108
5.	Conclusions and Future Work.....	110
5.1	Conclusions .....	110

5.2 Future Work .....	113
References .....	115
Appendix A: Gravimetric Analysis of cast A360.1 and LPBF AlSi10Mg .....	126
Appendix B: pH of solutions containing cast A360.1 and LPBF AlSi10Mg .....	137
Appendix C: NaI(Tl) Detector Peak Efficiency .....	138
Curriculum Vitae	

## List of Tables

Table 1: Chemical composition of LPBF AlSi10Mg block and A360.1 diecast.....	7
Table 2: Raw gravimetric measurements of cast A360.1 and LPBF AlSi10Mg .....	129
Table 3: Peak efficiency of a 3” x 3” NaI(Tl) detector.....	138

## List of Figures

Figure 1-1: A simplified hypothesized LOCA is occurring in the containment building [2]. .....	5
Figure 2-1: Closely packed FCC structure containing twice as many tetrahedral as octahedral [13]. .....	10
Figure 2-2: Crystal structure of silicon (a) Diamond cubic lattice (b) Crystal plane of silicon [15]. .....	12
Figure 2-3: The Al-Si binary phase chart, the red arrow indicates the point of formation and phase change of Al-10Si [17].....	14
Figure 2-4: Graphic illustration of the laser-based powder bed fusion method and equipment [21]. .....	19
Figure 2-5: Schematic diagram of oxide deposit on the aluminum alloy. ....	20
Figure 2-6: E-pH diagram for an aluminum-water framework at room temperature [25]. .....	22
Figure 2-7: Experimental E-pH chart of aluminum in seawater [26]. .....	23
Figure 2-8: Pitting corrosion of aluminum alloys [27]. .....	25
Figure 2-9: (a) Concentration of iron Crud, (b) Concentration of iron ions from 304 stainless steel in the presence of 20ppb O <sub>2</sub> with a flow rate of 0.33 mL/sec at 250°C.[45]. .....	32
Figure 3-1: Schematic of view of aluminum alloy (a) bulk aluminum alloy sample, (b) sliced extract of the aluminum alloy samples used for this study.....	36
Figure 3-2: Schematics of the Pb block <sup>60</sup> Co source holder with 4μCi <sup>60</sup> Co source placed inside the lead block.....	38
Figure 3-3: Schematic view of the radiation absorption technique.....	44
Figure 4-1: Typical microstructure of cast A360.1 aluminum alloy.....	45

Figure 4-2: Typical microstructure of LPBF AlSi10Mg (a) unetched featureless microstructure (b-c) etched microstructure showing different zones (d) high magnification of the three zones. ....	50
Figure 4-3: X-ray diffraction patterns of cast A360.1 aluminum alloy before exposure.	54
Figure 4-4: X-ray diffraction patterns of LPBF AlSi10Mg aluminum alloy before exposure. ....	55
Figure 4-5: Raman spectroscopy analysis areas.....	56
Figure 4-6: Raman spectrum of cast A360.1 aluminum alloy before exposure.....	57
Figure 4-7: Raman spectrum of LPBF AlSi10Mg aluminum alloy before exposure. ....	58
Figure 4-8: Weight change of cast A360.1 aluminum alloy. ....	59
Figure 4-9: Weight change of LPBF AlSi10Mg aluminum alloy.....	64
Figure 4-10: SEM images of cast A360.1 exposed in the absence of radiation.....	72
Figure 4-11: Surface analyses (a) XRD pattern of non-irradiated cast A360.1 (b) Raman spectrum of the corrosion product deposit of non-irradiated cast A360.1.....	76
Figure 4-12: SEM images of cast A360.1 exposed in the presence of radiation. ....	80
Figure 4-13: Surface analyses (a) XRD pattern of irradiated cast A360.1 (b) Raman spectrum of the corrosion product deposit of irradiated cast A360.1. ....	82
Figure 4-14: SEM images of LPBF AlSi10Mg exposed in the absence of $\gamma$ -radiation. (a) corrosion product deposit (b) result of descaled (a), (c) EDS results of LPBF AlSi10Mg alloy.....	85
Figure 4-15: Surface analyses (a) XRD of non-irradiated LPBF AlSi10Mg (b) Raman Spectrum of non-irradiated LPBF AlSi10Mg. ....	88
Figure 4-16: SEM images of LPBF AlSi10Mg after exposure in the presence of $\gamma$ -radiation .....	91
Figure 4-17: Surface analyses (a) XRD of irradiated LPBF AlSi10Mg (b) Raman Spectrum of irradiated LPBF AlSi10Mg. ....	93

Figure 4-18: The pH of seawater solution in the absence and presence of irradiation as a function of immersion time. .... 95

Figure 4-19: Changes in pH exposed to the environment without any aluminum sample in the presence and absence of  $\gamma$ -radiation. .... 99

Figure 4-20: Radiation counts for gamma rays as a function of energy. .... 103

## List of Abbreviations

AM	Additive Manufacturing
ASW	Artificial SeaWater
BWR	Boiling Water Reactor
CANDU®	CANada Deuterium Uranium – Trademark of Atomic Energy of Canada Ltd
CP	Corrosion Product
DI	De-Ionized Water
DMLS	Direct Metal Laser Sintering
ECCS	Emergency Core Cooling System
EDS	Energy Dispersive x-ray Spectroscopy
FEPA	Federation of European Producers of Abrasives
FE – SEM	Field Emission Scanning Electron Microscopy
HAZ	Heat Affected Zone
LET	Linear Energy Transfer
LOCA	Loss of Coolant Accident
MP	Melt Pool
NaI(Tl)	Sodium Iodide (Thallium)
LPBF	Laser Powder Bed Fusion
PWR	Pressurized Water Reactor
UNB	University of New Brunswick
XRD	X-Ray Diffraction
FCC	Face Centered Cubic

## 1. Introduction

Aluminum and its alloys have been utilized generally in a myriad of industries/enterprises due to their excellent characteristics, for example, high strength and reduced density, ease of formation and recycling, and corrosion resistance. Industrial application of aluminum alloys ranges from aerospace, surface coating, marine and shipbuilding industries, and advanced nuclear reactors. The excellent characteristics displayed by aluminum have made it one of the most consumed nonferrous metals and stand a chance to outplay heavier materials (steel and copper) in most industries. The presence of silicon as an alloying element strengthens and improves the ability of aluminum alloys to resist corrosion. The alloys produced from this combination make up all the cast components of aluminum generally utilized in automotive, aviation, and marine productions [1]. The neutron capture for aluminum is low, tending to possess excellent physical properties and great ability to resist corrosion, especially in water. These characteristics have projected aluminum alloys as a choice material for reactor containment buildings components. In nuclear reactors (pressurized, boiling water reactor – PWR, BWR, and Canada Deuterium and Uranium - CANDU)), aluminum alloys occur in (thermal insulations, ladders, scaffoldings, etc.) as found in the containment buildings [2].

In any nuclear-powered system, various safety designs are incorporated to shut down, to cool, and to hold volatile radioactive species in any episode of loss of coolant accident (LOCA) through the use of an emergency coolant from the emergency core cooling system (ECCS). The containment sump holds the coolant loss in the event of pipe leak or rupture, activating the ECCS process to cool and prevent fuel meltdown by reinjecting the



coolant back into the core. When there is a LOCA, the dislodgement of materials from coatings, pipe insulation, and concrete occur as a result of highly pressurized coolant. These materials are transferred to the sump, where aluminum, a containment material in the reactor containment building, also corrodes in the process [3]. The corrosion of aluminum in the process is a significant concern in the chemical environment of the containment building during a LOCA.

The reactor containment building is designed with a strainer to prevent LOCA debris from clogging and damaging the ECCS pumps and heat exchangers. The clogging of strainers was an issue on July 28, 1992, when insulating materials used previously in a scheduled test blocked the strainers of a Swedish BWR [4]. This clogging alerted nuclear regulators that a complete blockage of strainers can hinder the smooth operation of the ECCS system. Also, activated species can accumulate at the sump strainer, increasing the radiation field at the strainers and affecting their corrosion behavior as radioactive electrolyte contacts containment materials such as aluminum. The actual dose rate at the sump strainers is yet to be determined [5].

Several studies have been carried out on the causes of debris in reactor containment building and eradicating their possibility to clog and block the strainers affecting the successful operation of the ECCS system. Previous studies have shown that coolant released during LOCA is corrosive [6] and radioactive [7]; the post-LOCA coolant corrodes the containment materials saturating the coolant with soluble corrosion products and activated debris while forming solid-phase precipitates as shown in

**Figure 1-1** below. The containment material includes reactor system structural materials (piping, steam generator, reactor internal structures, heat exchangers, and reactor pressure

vessel), ECCS pump, valve, materials deposit on fuel cladding, intact insulation, and electrical materials [7]. The activated debris and corrosion products resulting from these components lead to the interruption of flow to the ECCS system. Other studies focused on the precipitation of aluminum hydroxide when spray/showers and sump water corrode aluminum alloys. The corrosion products resulting from this electrochemical reaction lead to a substantial head loss [8]. Similarly, Huang et al. [9] identified the release of intermetallic particles containing Fe widely present in the aluminum matrix into the coolant to be contributing to the clogging of the strainers as corrosion continues during LOCA and long term recirculation flow.

Many tons of aluminum alloy components exist in the reactor containment building. They contain a large quantity of intermetallic particles (IMP), which are released into the coolant system due to the selective dissolution effect, thereby contributing to the debris amount that blocks the strainers [9]. The presence of intermetallic particles could be ascribed to the manufacturing procedure of the alloys as they undergo different types of cooling and solidification behavior during the production process. Therefore, it is imperative to compare different manufacturing procedures for the same alloy with a similar composition to determine the contributing effect of IMPs. To that effect, different manufacturing procedures were deployed in producing aluminum alloys with similar compositions using conventional diecast process and additive manufacturing, especially laser powder bed fusion (LPBF).

This project is focused on the irradiation assisted corrosion of aluminum alloys manufactured using two different procedures to determine the effect of irradiation on each production process. The contribution of IMP particles from each manufacturing procedure

to the debris amount occurring in the containment in the presence of radiation will be investigated. Finally, develop microstructural characterization data to support the use of additively manufactured alloys as a replacement option in the industry. The microstructure and production process affect the properties and corrosion behavior of materials. We seek to understand how these two alloys behave when exposed to ionizing radiation.

Seawater, which is known to contain high aggressive ions such as chloride ions, sulfate ions, etc., which are corrosive to metals, is used as the corrosion medium due to its destructive effect on metals. Also, seawater may be used to help cool the reactor and keep the fuel rods from being uncovered under extreme conditions. This was observed in the Fukushima Dai-Ichi reactors when the pumps circulating the cooling water stopped working, and the reactor vessel coolant starts to turn to steam and boil away. Emergency workers were forced to pump and use seawater to replace the water that boils off [10] when other water supplies became unavailable. The experimental setup comprised an irradiated test cell investigating the corrosion and oxide deposits on the cast and LPBF aluminum alloys immersed in seawater solution in the presence of a low-dose gamma source.

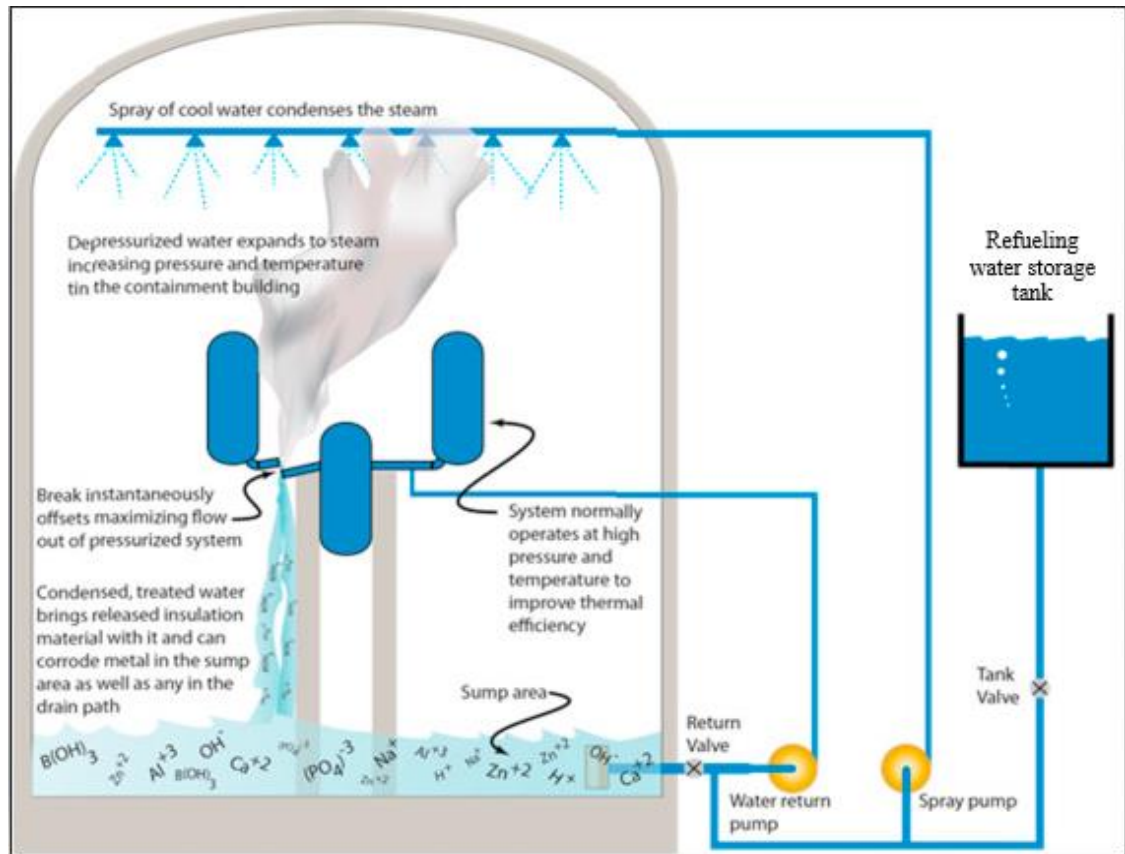


**Figure 1-1: A simplified hypothesized LOCA is occurring in the containment building [2].**

This project intends to understand the way gamma radiation affects the corrosion behavior of aluminum alloys manufactured using conventional casting and additive manufacturing in a simulated seawater solution. The second chapter presents the background relevant to this work. Chapter three describes the design and testing procedures where samples are irradiated with a gamma source exposed to the seawater environment, permitting studies into how radiolysis affects the corrosion behavior of aluminum alloys. The experimental result and discussion are presented in chapter four, and chapter five contains the concluding comments and recommendations for future works.

## 2. Literature Review

### 2.1 Properties of Aluminum Alloys

The behavior of aluminum alloys and their inherent properties is dependent on their microstructure and composition. Aluminum alloys can be classified into two types: wrought and cast. Further classification of these groups of alloys is dependent on the method of their development; for example, most of the wrought compositions are produced based on work hardening by combining other methods such as quenching, age hardening, etc., through mechanical reduction. The focus of this work is cast composition, which is not heat treatable and is deployed as an as-cast and its counterpart, the LPBF.

The Aluminum Association divides alloys into families for simplification; it assigns a digital method and a decimal value. The pure unalloyed aluminum is assigned the 1xx.x number. When copper is the chief alloying component, alloys are given the 2xx.x number. Alloys comprising silicon as the principal alloying element are assigned 3xx.x and 4xx.x. However, about 90% of all the shaped casting alloys are made from the 3xx.x series with copper and magnesium specification. The 5xx.x has magnesium as a major alloying element, etc.

The specific application of aluminum determines the type of alloying element to be incorporated for its performance, including increased strength, good corrosion behavior, and easy machinability.

#### 2.1.1 Composition

The content of the two alloys utilized for this investigation is presented in **Table 1**. The key alloying components for the two alloys are silicon and magnesium. These alloys

contain about 10.0% silicon content by weight (wt.) and 0.5 wt.% magnesium content. The presence of silicon improves the castability, fluidity, and ability of both alloys to resist corrosion.

Magnesium assists with improving the casting characteristics and properties of the silicon-aluminum alloy when incorporated into the microstructure. Al-Si alloys are generally utilized industrially because of their excellent ability to resist corrosion [11].

**Table 1: Chemical composition of LPBF AlSi10Mg block and A360.1 diecast.**

	Si	Fe	Cu	Mn	Mg	Ti	Zn	Al
AlSi10Mg	9.0-11.0	<0.55	<0.05	<0.45	<0.20-0.40	<0.15	<0.10	Balance
A360.1	9.0-10.0	1.30	0.60	0.35	0.40-0.60	-	0.50	Balance

### 2.1.2 Effect of Alloying Additions

In strengthening the microstructure of these alloys, certain elements were added due to their unique properties. Elements such as:

**Copper:** This element is added to aluminum due to its solubility and extensive strengthening effect owing to the characteristics age-hardening imparts to aluminum. Depending on its desired use, the concentration can range between 1 and 10%. Copper tends to reduce the corrosion resistance of most aluminum alloys and can accelerate the vulnerability of the alloy to stress corrosion depending on the composition of copper contained in the alloy's microstructure [11].

**Iron:** During die casting, iron helps to mitigate the die sticking. The high quantity of iron in the aluminum microstructure reduces the ductility of the alloy. It prompts the arrangement of particular intermetallic phases such as Al<sub>3</sub>Fe, Al<sub>6</sub>FeMn, and  $\alpha$ -SiAlFe,

which are detrimental to microstructure as a result of the low attachment of these phases to the  $\alpha$ -Al network. These phases' insolubility strengthens the alloy and leads to embrittlement of the microstructure when the iron content increases with an increase in the insoluble fractions [12].

**Manganese:** This alloying element has partial solubility in aluminum and acts as extra additions in both heat-treatable and non-heat-treatable alloys to strengthen the aluminum alloy. The concentration in aluminum is <1%, and it is controlled to a low level in most gravity cast compositions. The combination of iron with manganese is considered isomorphous, forming less detrimental intermetallic phases. The presence of this element in the melt helps to modify the morphology, the nature of intermetallic formed and reduces the formation of detrimental iron phases listed above like SiAlFe through the formation of  $\alpha$ -Si<sub>2</sub>Al<sub>15</sub>(FeMn)<sub>3</sub> and (FeMn)Al<sub>16</sub> phases, which improves the mechanical and corrosion properties of the alloy [12].

**Silicon:** This is one of the major alloying elements for the 3xx.x series used for this study. The concentration can range from 1 – 20% depending on its desired use, but the silicon range in the alloy used for this project is 9 – 10%. Silicon helps lower the melting point of aluminum and, at the same time, increase the melt fluidity. Silicon also helps to improve the casting features of the alloy. Aluminum alloys containing silicon tend to have high resistance to solidification cracking displaying excellent castability, which helps to reduce shrinkage porosity [12].

**Magnesium:** For the strength and hardness of an aluminum alloy containing silicon, magnesium is added. Magnesium is combined with other elements to improve its strengthening ability. For example, magnesium and silicon consolidate to form Mg<sub>2</sub>Si,

which helps in the age hardening of the cast alloys. The  $Mg_2Si$  phase shows a suitable solubility limit range of 0.70% Mg, and past this point, the disintegration of the alloy occurs. The composition of magnesium is  $< 0.5\%$  in the alloy used for this study [12].

### 2.1.3 Crystal Structure of Aluminum

Aluminum is widely known to contain a face-centered cubic (FCC) crystal structure, packed closely. For structures closely packed, many tetrahedral gaps and octahedral gaps exist in the structure, as shown in **Figure 2-1**. The FCC unit cell below contains a primitive rhombohedral cell that contains only one atom. Also contained in the primitive cell are two tetrahedral gaps at the two ends of the octahedral one. There are periodic repetitions of primitive cells found in the structure used to describe the crystal structure of aluminum, thereby making the ratio of two tetrahedral to one octahedral repetition applicable to the bulk material and making up the bulk of materials [13].

The stacking of these structures is in the sequence of ABC. These (A, B, C) are the center sites of an atom to a layer closely packed. For aluminum with an FCC arrangement, we have eight atoms at each corner of the cube, then each face of the cube contain one atom at the center; therefore, the total atom contained in FCC aluminum is  $(8 \text{ corner atom} \times \frac{1}{8}) + (6 \text{ face atom} \times \frac{1}{2}) = 4 \text{ atoms}$ .



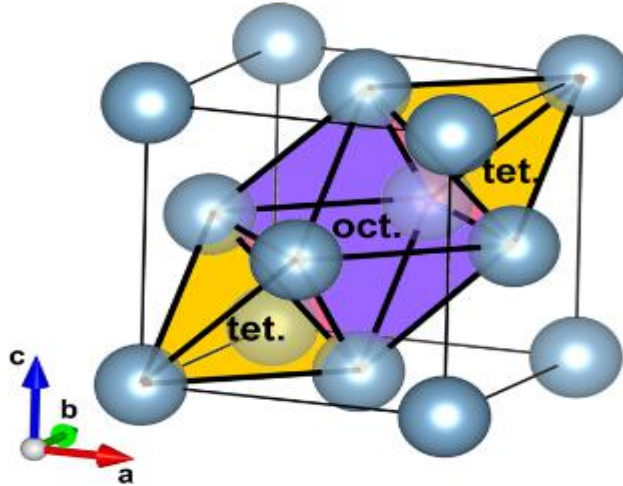


**Figure 2-1: Closely packed FCC structure containing twice as many tetrahedral as octahedral [13].**

**Figure 2-1** shows the FCC to contain about two parallel planes in four sets, and previous studies have shown that parallel planes with a similar atomic arrangement are comparable; therefore, an FCC structure has four equally close-packed planes. The use of Miller indices is the best method to describe the atomic planes and direction in a crystal lattice. Note that marking a plane with  $(hkl)$  means that only the plane is contained in it, and when it is marked with  $\{hkl\}$  means all planes are in the same family.

Directions are stated in square brackets as  $[hkl]$ , and they are vertical to the plane, while the direction's family is expressed as  $\langle hkl \rangle$ . Therefore, applying the Miller indices present aluminum in  $\{111\}$  planes meaning that the FCC aluminum has four  $\{111\}$  planes that are near packed; also, a three close-packed direction can be drawn as well belonging to the  $[110]$  directions placed diagonally across the cube faces. In general, three  $\langle 110 \rangle$  directions are known to exist for each  $\{111\}$ , making the FCC structure to contain a

possible mixture of  $\{111\}$  and  $\langle 110 \rangle$ . The FCC structure of aluminum contains  $\{111\}$  planes closely packed in a  $\langle 110 \rangle$  directions [14].

#### 2.1.4 Crystal Structure of Silicon

The crystal structure of silicon is a diamond cubic with the atoms covalently bonded, as shown in **Figure 2-2a**. Silicon tends to possess a lattice spacing of 5.42Å. The silicon atoms follow the FCC Bravais lattice with eight atoms in a unit cell at a vector location, usually associated with this structure. This means that four atoms that are equally spaced surround each atom in a tetrahedral arrangement. Silicon has a density packing factor of 34%, which is quite loose compared with other FCC lattice (e.g., aluminum) whose packing factor is 74%, and body-centered cubic structure (pure iron at room temperature) with packing density of 68%. An octahedral hole is the biggest space found in a diamond cubic structure, and it can occupy 41% of the atomic size of the host atom.

In a crystal lattice of silicon, there are several planes and directions. Miller indices are utilized to interpret these atomic planes and directions. For silicon that is cubic, the lattices' axes are orthogonal, and the various parameters in all directions (x, y, z) tend to be identical. In miller indexes (hkl), the reciprocals of the intercept points are accounted for. For example,  $a/a$ ,  $a/\infty$ ,  $a/\infty$  or (100), plane (110) shows that the intercepting points are  $a,0,0$ ,  $0,a,0$ , and  $0,0,\infty$ , and the same goes for (001) plane, as shown in **Figure 2-2b** [15].

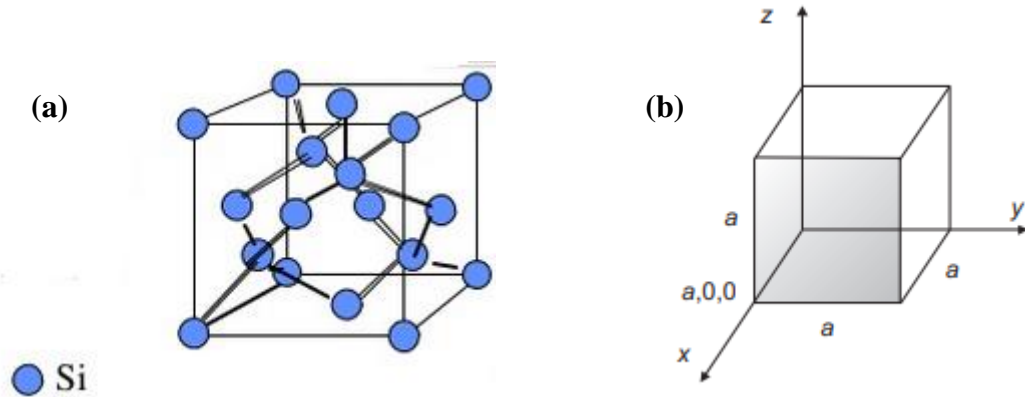


**Figure 2-2: Crystal structure of silicon (a) Diamond cubic lattice (b) Crystal plane of silicon [15].**

### 2.1.5 Phase Diagram of Al-Si Systems

In order to understand the alloying element's behavior and the modalities of the alloying system, phase diagrams are used. We can determine how compositions changes in phase relationships at equilibrium conditions considering temperature as a function from the phase diagram. Alloys containing between 5 and 11.7 wt.% Si is called hypoeutectic, then those with a higher amount of silicon greater than 11.7 wt.% Si is referred to as hypereutectic; the eutectic point for this phase diagram is at 11.7wt.% Si, as shown in

**Figure 2-3.** From the phase diagram, the melting point of the Al is 660.37 °C, while that of Si is at 1414 °C.

Two solid solution phases are present on this phase diagram, such as the FCC  $\alpha$ -Al phase and diamond cubic Si, liquid phase (L), and three other mixed phases: liquid L +  $\alpha$ -Al, liquid L + (Si), and  $\alpha$ -Al + Si. A great understanding of this phase diagram helps guide the control of processing parameters for any alloyed system.

Analyzing the phase chart in

Figure 2-3 shows the tight zone between 500 °C and Al melting point at 660.37 °C (0 wt.% Si) to be the FCC  $\alpha$ -Al solid solution, the diamond cubic Si solid solution is formed around 500 °C and 660.37 °C (0 wt.% Al). The liquid phase is formed at the eutectic point of 11.7 wt.% Si at 580 °C. In order to interpret the three mixed regions starting from the bottom  $\alpha$ -Al + Si, the region ranges from 0 to 100 wt.% Si with a temperature range of 500 °C to the eutectic temperature of 580 °C. The second mixed region is the liquid L +  $\alpha$ -Al, which occurs around 0 – 12.5 wt.% with a ranging temperature from 580 °C eutectic point to Al melting point of 660.37 °C. Finally, the liquid L + Si phase starting from the eutectic point at 580 °C to the melting point of Si 1414 °C and at 100 wt.% Si [16]

The elements of Al and Si tend to have a low solubility in each other. As shown in the phase chart, 1.65 wt.% is the maximum solubility of Si in Al, which occurs at the eutectic temperature. The general Al-Si eutectic has a soft Al matrix containing a Si phase known to be hard and brittle.

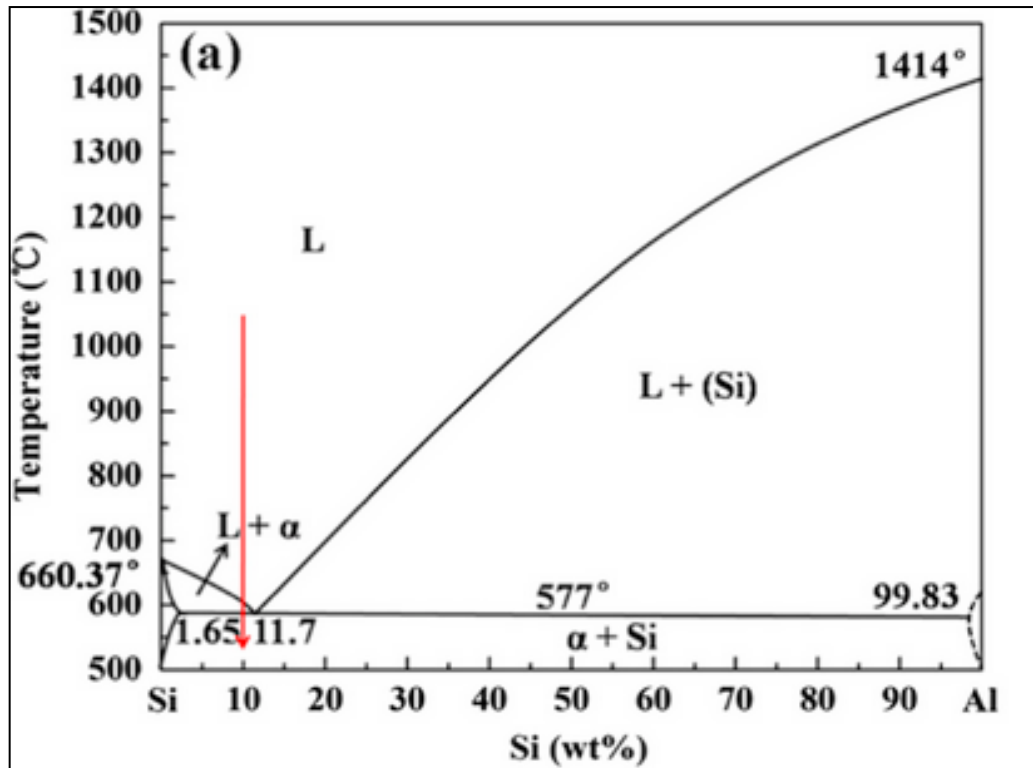


**Figure 2-3: The Al-Si binary phase chart, the red arrow indicates the point of formation and phase change of Al-10Si [17].**

As reported earlier, varying the overall composition and temperature of a mixture results in different shapes and structures of phases as the melt (mixture) cools down to room temperature. The Y-axis of the phase chart shows the different temperature ranges indicating that a mixture of alloying elements will not melt at a specific temperature but tends to either melt or solidify as they experience a temperature change through heat application and/or removal of heat. Solidification or melting can only occur at the eutectic point.

The redline appeared at the left of the eutectic point, indicating that the alloy formation is in the hypoeutectic region. At a temperature of 1050 °C, the mixture of Al and Si is maintained in the liquid phase due to high temperature. The mixture remains in the liquid

state on continuous cooling down until the redline touches the liquid equilibrium line; at this point, solidification of the  $\alpha$ -Al phase takes place. Dendrites are formed as  $\alpha$ -Al solidifies and continues to grow as various grains of  $\alpha$ -Al are formed. Before the eutectic temperature as continuous cooling occurs, more nucleation sites tend to exist in the liquid mixture. Here, the liquid mixture will contain pulpy lumps at the L +  $\alpha$ -Al region of the phase chart. The L +  $\alpha$ -phase contains mainly Al atoms (with a small amount of Si in solid solution); the remaining liquid is enriched with Si on continuous cooling of the melt as shown by the liquid line.

There tends to be a continuous growth of the  $\alpha$ -Al phase and rearrangement of the phase composition until most Al atoms have been removed. At this point, the melt's composition is that of eutectic composition; this is the point the redline crosses the eutectic line. At this eutectic composition, the  $\alpha$ -Al phase stops forming, and the remaining mixture solidifies into a lamellar structure with a eutectic composition (having different layers of  $\alpha$ -Al + Si). The lamellar structure will continue to grow with even distribution of Al atoms to the  $\alpha$ -Al phase and Si atoms to the Si phase in the eutectic region [18].

## **2.2 Manufacturing Procedure**

Although the essence of this investigation is to compare the corrosion behavior of aluminum alloys produced using conventional casting method and additive manufacturing, it is necessary to look at the alloys' manufacturing procedures to find common similarities or differences to help interpret their behavior when exposed to irradiated seawater solution.

### **2.2.1 Die Casting**

The production of aluminum alloys using the die casting method is to produce a high volume of cast aluminum alloys with a perfect surface finish. Pressure die casting is the manufacturing procedure used to produce the cast A360.1 alloy. As with every machine, the machines for die casting differ in capacity, type, and size. Die-casting comprises of two types, such as hot and cold chamber operation. The hot chamber operation is currently not in the commercial application; therefore, all die casting production for aluminum is through the cold chamber. Water-cooled dies are used for this production by injecting molten metals under pressure; this pressure is maintained until all parts are solidified. The dies are usually uninsulated, and lubricants help to separate the casting from the die surface.

Major defects in the microstructure of diecast alloys such as air entrapment, fragmentation, and turbulence can be reduced by accounting for the geometry using sustained pressure to promote internal soundness. Entrapped gases affect the quality of the cast alloys, and techniques can be used to reduce the volume fraction of the internal porosity by increasing pressure during the solidification phase. The cast alloy used for this study was manufactured through this process, as its low copper content offers an excellent resistance to corrosion and castability.

The magnesium content is minimal and helps to reduce oxidation and high production of oxides during the casting process. The presence of iron helps to facilitate ejections after casting, reduce soldering, and maintain an optimum temperature strength. After production, the cast A360.1 alloy used for this study contained many voids, which could be attributed to hydrogen precipitation from liquid solution or solidification shrinkage.

Hydrogen is soluble in aluminum, and its solubility changes as the square root of pressure and temperature changes; solubility tends to rise as temperature rises.

The voids/pores found after production could be attributed to the precipitation of the excess hydrogen in molecular form during the slow cooling and solidification process. The presence of hydrogen in the mold could be moisture dissociation in the atmosphere or combustion products in the furnace atmosphere allowing the diffusion of atomic hydrogen into the melt [12].

As calls for replacement parts continue to rise due to increased demand for materials resulting from an increase in the world's population, calls for improved complex casting materials with high quality at a lower cost continue to upsurge. Industry experts have been working to satisfy these demands leading to the development and promotion of additively manufactured machines for specialized applications and mass production with enhanced performance.

### **2.2.2 Additive Manufacturing Systems**

One of the challenges of the conventional casting process for manufacturing aluminum alloys is the difficulty of producing cast alloys close to the finished product eliminating any surface finishing requirement like machining due to hot tearing, voids, etc. Additive Manufacturing (AM), with its numerous advantages against the conventional manufacturing process, tends to solve these problems to produce complex components of any shape to the desired product.

AM has the edge over the conventional manufacturing process due to its design flexibility and geometry, reduced materials and energy, cost and time efficiency, environmental



friendly and high productivity, etc. [19]. AM is also a form of casting but on a micro-level, so understanding the conventional casting process resulted in great insight into the additive process.

Therefore, additive manufacturing is an advanced technique for manufacturing a complex but high valued metal layer by layer by utilizing computerized aided design data. First, the required design is generated using a design model based on the required specifications. The file is uploaded into an additive system. The additive system divides the design into manageable sizes of two-dimensional layers. Finally, two-dimensional layers produce three-dimensional parts [20].

Numerous technologies can be deployed to produce AM components, such as the powder feed system, wire feed system, and powder bed system. The alloy used for this study was produced through the laser powder bed system and will be the focus of our discussion.

### **2.2.3 Laser Powder Bed System (LPBF)**

This system utilizes powder prepared in tiny deposits and joined together by a laser as a feedstock. In the alloy production for this study (AlSi10Mg), the powder is consolidated through a liquid phase by a complete melting-solidification mechanism, as shown in **Figure 2-4**. A laser powder bed fusion is controlled under a protective atmosphere containing argon. On the building platform's working surface, powder layers of a measured thickness are spread uniformly over the entire surface. The laser beam's irradiation of specific areas takes place by computer-aided design data. After each melting or sintering, the height of the powder bed platform is lowered, depending on the powder thickness and design specification.

The original layer tends to have a higher thickness than the last combined layer's thickness because of volume reduction to solid bulk material from loose powder. As we keep on descending the construct stage, another powder layer is placed on the former layers. This process continues until the required shape from the computer-aided design is built [21].

The schematic diagram is shown below:

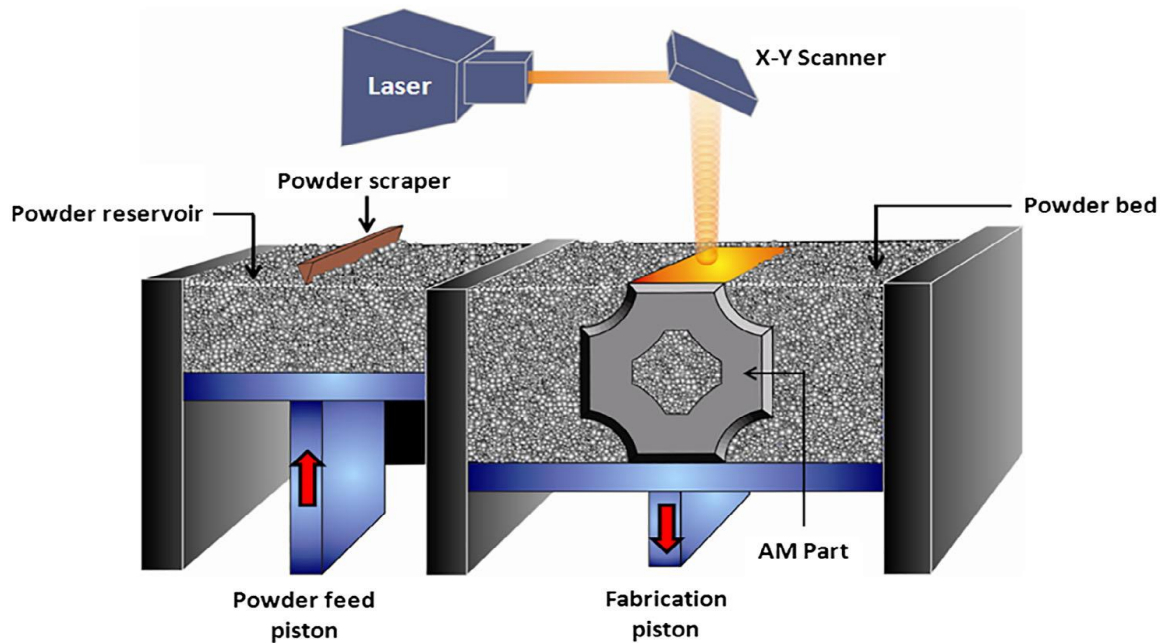


**Figure 2-4: Graphic illustration of the laser-based powder bed fusion method and equipment [21].**

## 2.3 Aluminum Corrosion

### 2.3.1 Passivity of Aluminum

Thermodynamically, aluminum is a reactive metal yet tends to possess excellent corrosion resistance when exposed to natural atmospheres, seawater, freshwater, etc. The resistance of aluminum alloys to corrosion is dependent on their ability to form barrier oxide film firmly attached to its surface. On exposure to air, the thickness of the oxide film found on

the surface is about 5 nm (50Å), and a much thicker film tends to form when exposed to water [22]. There is a tendency for the film formed on the surface to break. In some cases, the film reforms to protect the alloy, while in other cases, it does not reform, depending on the environment.

When the film cannot re-form, the metal tends to corrode; this is depicted in **Figure 2-5**. As mentioned earlier, exposing aluminum to natural atmospheres (air) leads to film formation on the alloy surface; two types of film, such as the inward oxide layer and the external oxide layer, are formed. The inward oxide deposit is formed directly on the metal surface, and the thickness is dependent on the temperature of the environment. The inner layer happens to be a compact amorphous layer.

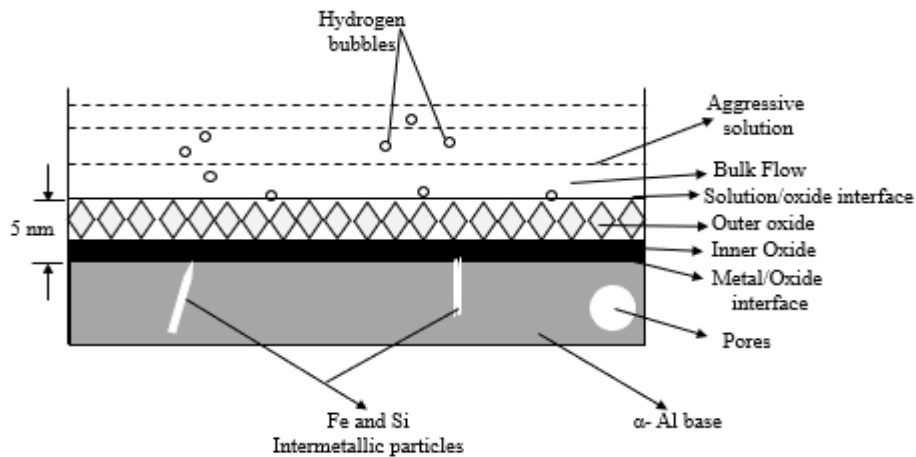


**Figure 2-5: Schematic diagram of oxide deposit on the aluminum alloy.**

The depth of this layer can be limited by the presence of oxygen or moist air. After the internal layer, the external layer is formed, which covers the internal layer. The external layer tends to be thicker and more permeable. The outer layer's behavior depends on the oxide layer's chemical properties and the intermetallic particles inherent in the alloy. The oxide film formed on the alloy exterior can be ascribed to the dynamic equilibrium

between contrasting forces relating to either development of an oxide deposit that is thick or the inability of the oxide deposit formed to be adherent.

Different elements can add to the disintegration of the oxide layer, such as oxygen and chloride ions. In the presence of aggressive ions, for example, chlorides, the oxide film is destabilized, and the metal surface is prone to localized corrosion [11]. Previous studies have established that the presence of an existing defect on the alloy surface can be a catalyst to the breaking down of passive films formed on the alloy surface. This is because chloride ions are aggressive and react directly to the metal [23]. As a result of this direct contact between aggressive ions, an electrochemical reaction is initiated on the oxide metal interface. Hydrogen blisters prone to rupture are formed due to this electrochemical reaction.

The point defect model [24] projected that the migration of aggressive ion (chloride ion) to the interface between metal/oxide results in failure of the passive films formed on the alloy surface. The chloride ion penetrating through the oxide layer leads to displacement in the oxygen vacancies, producing cation vacancies at the solution/oxide interface, thereby damaging the oxide film.

Pourbaix diagram is utilized for expressing the thermodynamic stability of the oxide film. Aluminum is known to form a passive film in the pH region of 4 to 9, and the limitations to this vary with temperature, environment, presence of intermetallic and soluble complexes. The Pourbaix diagram shown in **Figure 2-6** is for an aluminum-water system, and it is saddled with some drawbacks. Pitting corrosion found in aluminum alloys is not considered in the Pourbaix chart below, which is the main form of corrosion occurring due to the breakdown of the passive films.

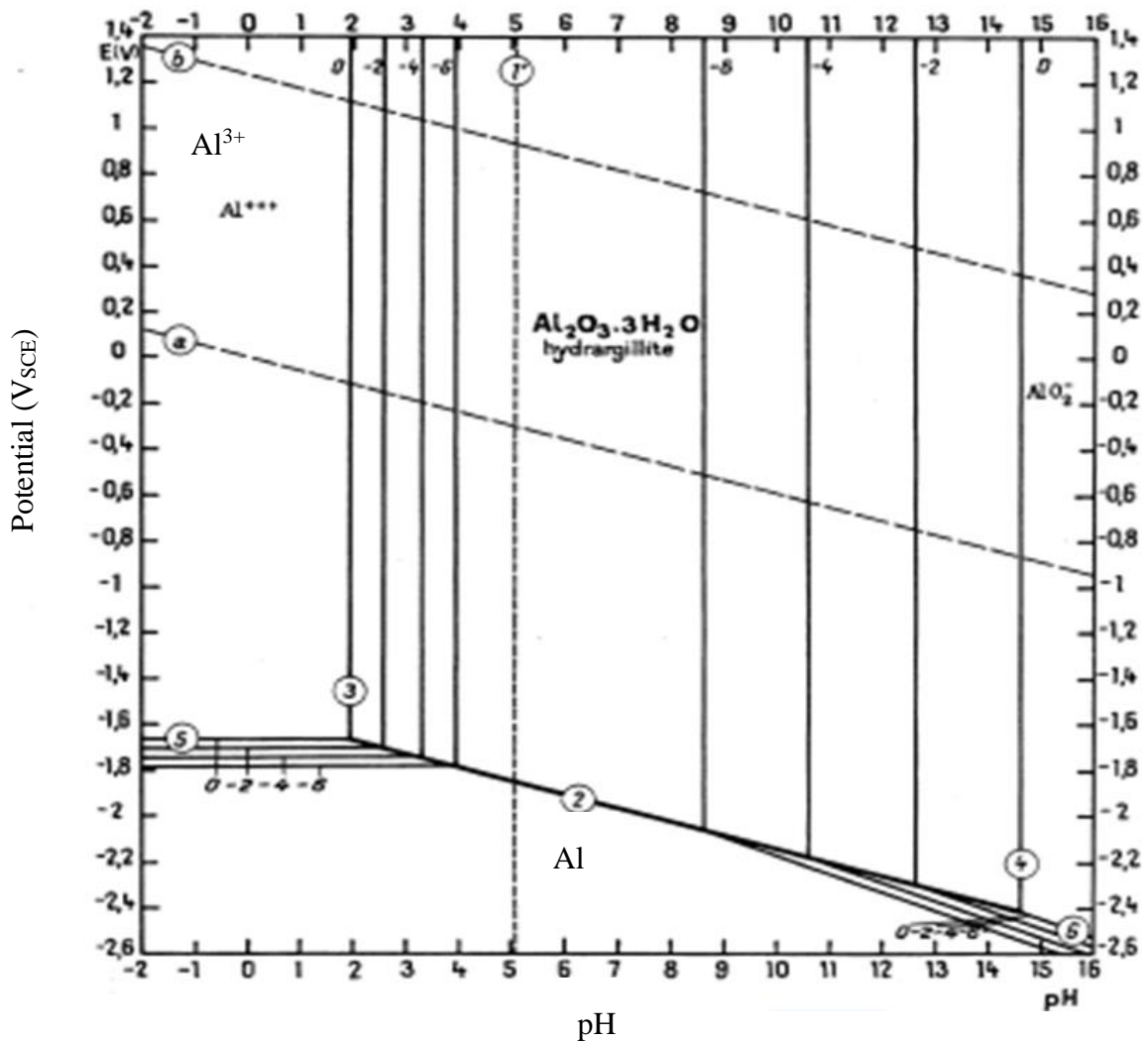


**Figure 2-6: E-pH diagram for an aluminum-water framework at room temperature [25].**

For an environment with high chloride content as seen in seawater, the above theoretical Pourbaix diagram is practically useless as aluminum tends to corrode in its theoretical immunity area while pitting occurs in the theoretical passivity areas. An experimental Pourbaix diagram could be used to account for the pitting corrosion of aluminum in seawater applicable to a marine environment, as shown in **Figure 2-7** [26].

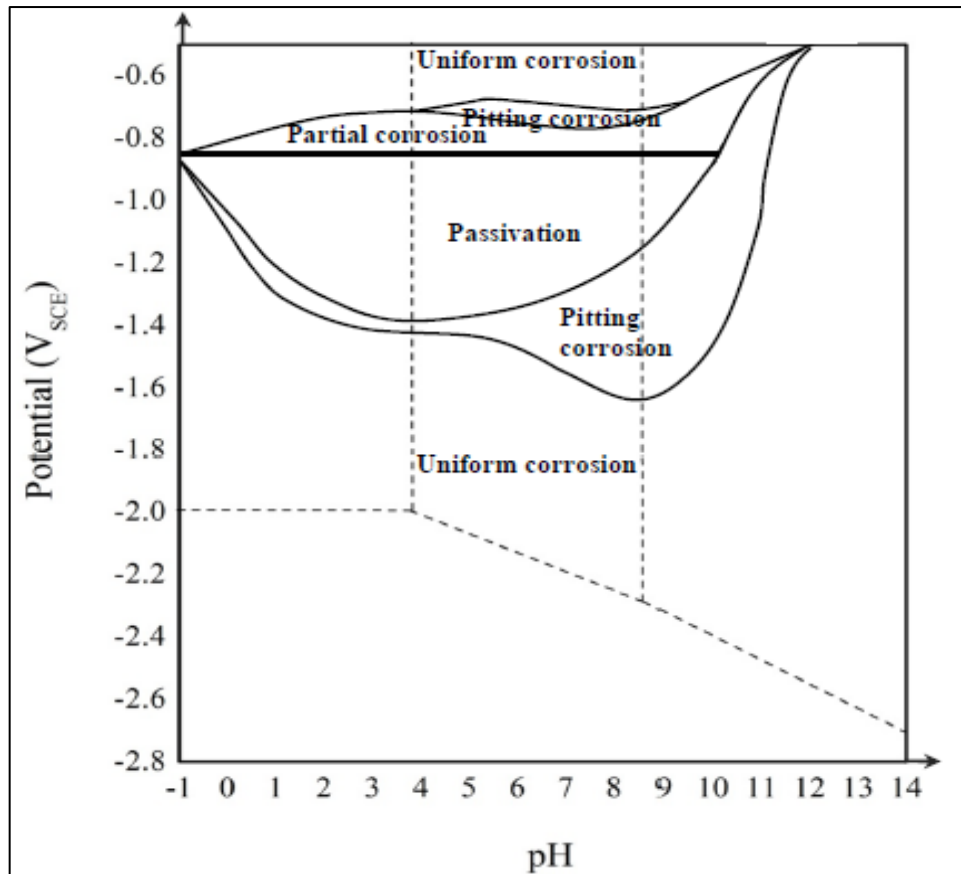


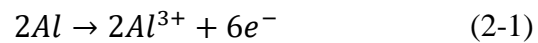
Figure 2-7: Experimental E-pH chart of aluminum in seawater [26].

### 2.3.2 Pitting Corrosion

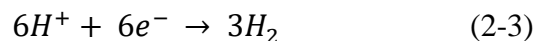
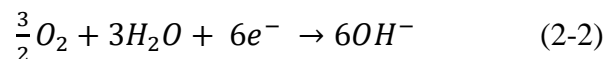
The aluminum alloys used for this study tend to undergo various forms of localized corrosion such as pitting. It can affect the integrity of the material due to the environment (seawater) to which it is exposed. The pit cavity formed on the aluminum surface is irregularly shaped, its depth and diameter depending on the aluminum alloy, electrolyte, experimental conditions, and manufacturing procedure. The pits formed on aluminum alloys are usually covered with oxide deposits. The diameter of the pits on the surface might be so small on the surface but huge in the underlying layer, most times going unnoticed until the material fails.

This form of corrosion happens in two stages: initiation and propagation. In the initiation stage, there is a high tendency that aggressive ions such as chloride will be retained with the oxide film exacerbating the failure of the oxide films and new development of microcracks around the intermetallic particles in the nanometer scale range. Pits tend to stop growing after a short time, and they are known as metastable pits. Metastable pits are parts of the pits formed as a result of exposure of aluminum alloys to a chloride-containing solution, the next type formed is the stable pit.

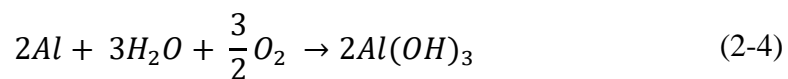
The corrosion damage on aluminum alloys does not result from metastable pits, but stable pits formed from the coalescing of metastable pits. Oxygen reduction takes place at the cathodic sites containing intermetallic phases beneath the oxide layer. If the oxide layer cracks, oxidation of aluminum occurs, leading to the formation of complex intermediate chloride  $AlCl_4^-$ . At the propagation stage, oxidation of aluminum occurs at the anode at the pit bottom



While cathodic reduction takes place outside the pit hole



The reaction above forms  $OH^-$  ions and consumes  $H^+$  ions, thereby forming an excess of the  $OH^-$  ions. The final pitting corrosion of aluminum becomes:



Aluminum dissolves at the bottom of the pit, forming  $\text{Al}^{3+}$ ; this allows the transfer of chloride ions to the bottom of the pit. Chloride ions are very mobile due to the small diameter of the ions. Aluminum chloride ( $\text{AlCl}_4^-$ ) is formed at the bottom of the pit as a result of this interaction, and further hydrolysis of the aluminum chloride leads to the pit's bottom acidification. The electrolyte at the bottom of the pit becomes aggressive, leading to pitting auto propagation, as shown in **Figure 2-8** [27].

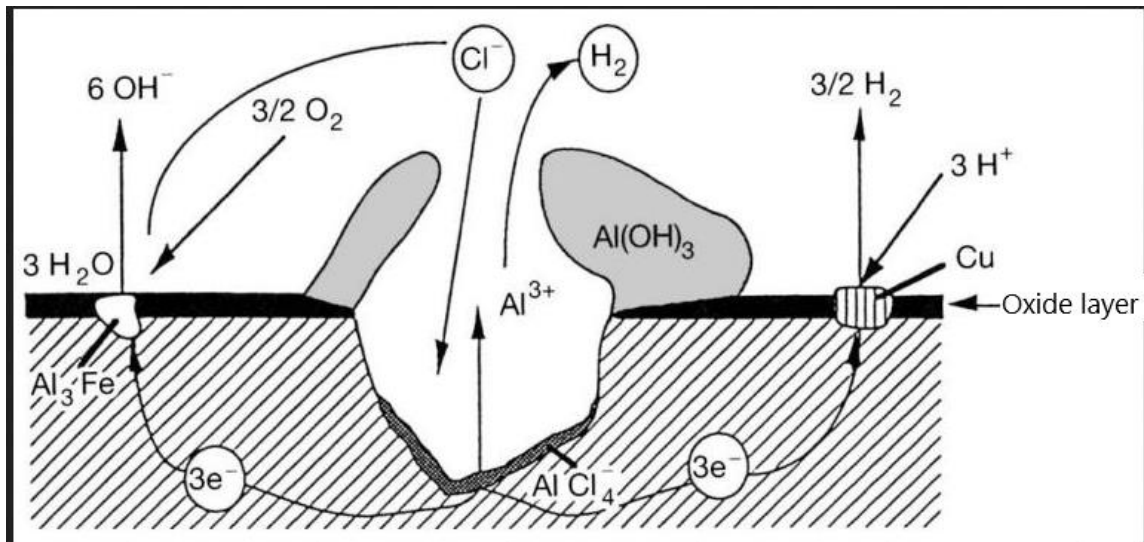


**Figure 2-8: Pitting corrosion of aluminum alloys** [27].

Seawater is known to contain a high amount of chloride ions, which is aggressive to aluminum alloys leading to a localized form of corrosion called pitting [28]. From the passivation and re-passivation point of view, the processes pitting corrosion undergoes makes it competitive as the metal surface deteriorates. There tends to be a high tendency to form protective films (re-passivation). One barrier for the re-passivation of films on aluminum alloys is the adsorption of chloride ions [29].



Therefore, exposing aluminum alloys to seawater increases the dissolution rate resulting in localized corrosion such as pitting. The experimental setup is expected to be open to air as no nitrogen/argon will be bubbled over the solution, so oxygen availability is another factor that can affect the corrosion behavior. Oxygen dissolved in the solution plays a vital role in the corrosion process in water as an oxidant [30]. The oxygen content in the solution might be limited as the sustenance of the film repair on the alloy will be slow because of the high content of chloride ions in the seawater, hindering pitting re-passivation [31].

## **2.4 Radiation and Water Radiolysis**

Having discussed the nature of the aluminum alloy and various corrosion principles of aluminum corrosion, we will consider the impact of radiation on this alloy. The impact radiation has on metallic corrosion can be explained vis-à-vis (a) the alloy itself, (b) the oxide layer (c) the electrolyte.

In the first part, the alloy itself, the interaction of radiation with the alloy leads to displacement damage leading to vacancies, interstitials, and thermal spikes. This occurs when the radiation source is neutrons, which is beyond the scope of this work. The impact of radiation on the oxide layer and electrolyte results from chemical changes as gamma rays disrupt the chemical bonds in water.

### **2.4.1 Radiation Chemistry**

The chemistry of radiation seeks to understand the chemical effects in a system exposed to ionizing radiation (high or low). Various types of ionizing radiation that could be in consideration include the energetic particles (alpha ( $\alpha$ ), protons, fast electrons/beta( $\beta$ ))

particles, and other heavy particles). The high energy photons ( $x$  and  $\gamma$ -rays) cause ionization (with a few excitations) of molecules in a medium. Acceleration of charged particles to higher energy or radioactive nuclei decay (from fission of nuclear materials or occurring naturally) leads to the generation of various forms of ionizing radiation.

The disintegration of  $^{60}\text{Co}$  leads to the emission of  $\gamma$ -rays in the energy level of 1173.2 and 1332.5 keV, and  $\beta$ -particles from this disintegration possessing energies in the range of 0.1 MeV to 5 MeV. The energies produced in this range cannot incite a nuclear reaction, but they are higher than the energy required to ionize atoms and molecules [32].

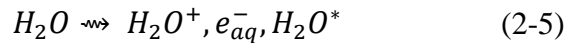
For radiation that ionizes, energy is transferred to the interacting medium (artificial seawater) by few phases of energy transfer called tracks. These interactions resulting in energy transfer depend on electrons in matter colliding with radiation particles. Thus, the amount of energy received by a medium is dependent on its thickness.

Therefore, for systems that are diluted, we discuss radiation chemistry in terms of solvent oriented process. The rate of radiation interaction is relative to the amount of energy a specific medium absorbs and the strength of incoming ionizing radiation [33].

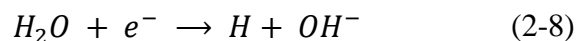
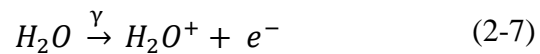
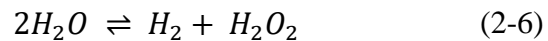
Ionizing radiation tends to exert chemical effects when it traverses a medium, which can be determined by the rate at which energy is transferred for every unit volume of the medium, called the linear energy transfer (LET) rate since chemical reactions depend on concentration. The interacting medium and nature of radiation determine the LET rate. The  $\alpha$ -particles show the highest LET (because of their huge size and charge) at that point, followed by the  $\beta$ -particle, with the least being the  $\gamma$ -photons [34].

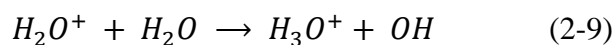
This results in different penetration depths for each particle or photon. Penetration depth for  $\alpha$ -particles is 20 – 25  $\mu\text{m}$ ,  $\beta$ -particles has a penetration depth of 0.5 – 1 cm, and  $\gamma$ -photons have many cms of penetration depth; all these are for water at 25°C. These penetration depths show the rate of reduction of these species to half of their original strength. The LET rate determines the concentration of ions and electronically energized atoms formed along the radiation track [35].

The first interaction of ionizing radiation with water molecules yields excitation or ionization of the water molecules forming an ion pair ( $\text{H}_2\text{O}^+$  and  $e_{\text{aq}}^-$ ) or an energized specie ( $\text{H}_2\text{O}^*$ ) towards the tracks of radiation, as shown below:



The  $e_{\text{aq}}^-$  known as the hydrated electron can form a second ion pair and excited species if it possesses enough energy. The new ionized species produced by  $e_{\text{aq}}^-$  will be within the locality of the first ionization, as 2-3 ionized and energized species cluster around the collision spot. Clustering of excited species and 2-3 ion pairs is called spur [33]. Furthermore, irradiated water decomposes to molecular products of hydrogen ( $\text{H}_2$ ) and hydrogen peroxide ( $\text{H}_2\text{O}_2$ ) as shown in equation (2-6), and decomposes to radical products such as hydrated electron ( $e_{\text{aq}}^-$ ), hydrogen (H) and hydroxide (OH) as shown in equation (2-7) - (2-9) below:

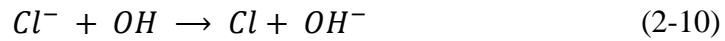




The radicals form at different concentrations along the particle track, and depending on the zone, they tend to react with each other forming  $H_2$  and  $H_2O_2$  to a certain extent. Conversely, some radicals escape from their zones reacting with  $H_2$  and  $H_2O_2$  molecules in the solution leading to water re-formation. Therefore, there is a high tendency to attain a steady-state when pure water is irradiated. This occurs when the product back reaction of  $H_2$  and  $H_2O_2$  to re-form water is equivalent to their production rate from water [36].

As the reacting medium is seawater, the interactions of radiation with seawater are assumed to be the same as those with pure water, leading to water radiolysis products at a steady state. The products of water radiolysis formed at this stage can be called the primary radiolysis products formed at a time scale of  $10^{-7}$  s in water, despite the fact they are not the principal species formed during irradiation. These radiolysis products occurring down to that time scale of  $10^{-7}$  s are,  $H_2O^+$ ,  $e^-$  occurring at (less than  $10^{-14}$  s), and  $H$ ,  $HO$ ,  $H_2$ ,  $e_{aq}^-$ ,  $H^+$ ,  $H_3O^+$ ,  $H_2O^-$  occurring at ( $10^{-14}$  -  $10^{-12}$  s). At the end of these reactions in the solution, the following species appear stable, such as  $HO$ ,  $H_2O_2$ , and  $HO_2$ , after  $10^{-7}$ s. These radiolytic products tend to further combine on continuous exposure or escape into the whole bulk solution forming oxygen ( $O_2$ ) as the per hydroxyl radicals ( $HO_2$ ) decompose.

Although the irradiation of seawater is modeled against pure water, the dissolved solutes in the solution tend to have some interfering effect. The presence of these solutes capable of redox reaction tend to destroy the radicals as they react with the solute as shown below:



## 2.5 Irradiation Corrosion

### 2.5.1 Irradiated – Corrosion of Aluminum Alloys

Aluminum alloys occur in the reactor containment building as thermal insulation materials, scaffolding materials, etc. They interact with the ECCS coolant as it washes over equipment during a LOCA before draining to the sump. Due to its utilization as a containment material, this alloy encounters various ionizing radiation, affecting the alloy's corrosion behavior. Several authors have studied how ionizing radiation tends to affect the corrosion behavior of the alloy. There has been much conflict in agreeing how radiation affects the corrosion of materials; some researchers believe that ionizing radiation does not affect the corrosion behavior of aluminum alloys in water, while others have a contrary opinion that irradiation accelerates the corrosion of aluminum alloys.

Simnad et al. [37] reported that the existence of  $\gamma$ -radiation reduces the corrosion rate of aluminum at room temperature in water. KRENZ [38] studied the corrosion of aluminum with alloying materials such as nickel, iron, and silicon for several hours in a water-cooled reactor at a high temperature and discovered that irradiation marginally affected the corrosion of aluminum.

Similarly, there have been indications that radiation accelerates the corrosion of aluminum, as reported in the literature. Borasky et al. [39] reported accelerated corrosion of aluminum alloys in hot water irradiation in a reactor as an increase in radiation intensity increased the corrosion rate. Stobes et al. [40] described reactor radiation to have increased

the corrosion of aluminum alloy. Kanjana et al. [41] stated that gamma irradiation accelerated aluminum oxide development on the alloy surface due to the increased density of oxide with extended irradiation and dose time.

Aluminum is readily oxidized, and its corrosion resistance is dependent on the passive film formed on the alloy. Radiation having the tendency to destroy the oxide film can reduce the ability of this alloy to resist corrosion as aggressive ions present in the solution tend to bypass through the film defect affecting the alloy matrix. For a neutral solution, there is a high chance of radiation contributing to the increased oxide deposit on the alloy, making it impossible for the aggressive ions to penetrate through these films to affect the integrity of the alloy.

Aside from aluminum alloys, studies have been carried on the impacts of radiation on many other metals, for example, stainless steel, carbon steel, Alloy 800, etc. Kawaguchi et al. [42] reported a thick oxide deposit on stainless steel when the solution was exposed to gamma radiation. The oxide layer thickness was about four times higher than the unirradiated samples. Also, Ishigure et al. [43] studied how CRUD is released from 304 stainless steel when exposed to gamma radiation (Co – 60 source). CRUD is metallic oxide particles depositing on the claddings of nuclear fuel rods. Ishigure discovered that irradiation increased CRUD formation significantly and reduced the formation of aqueous Fe ions [44], as shown in **Figure 2-9**.

The increase in alloys' oxide formation in various studies is expected as radiolysis tends to accelerate the creation of oxidizing species such as OH, O<sub>2</sub>, and H<sub>2</sub>O<sub>2</sub>. This combines with the metal forming insoluble products such as ferric hydroxide and haematite for

stainless steel and aluminum oxide and aluminum hydroxide for aluminum alloys; these account for the increase in CRUD formation and oxide deposition, respectively.

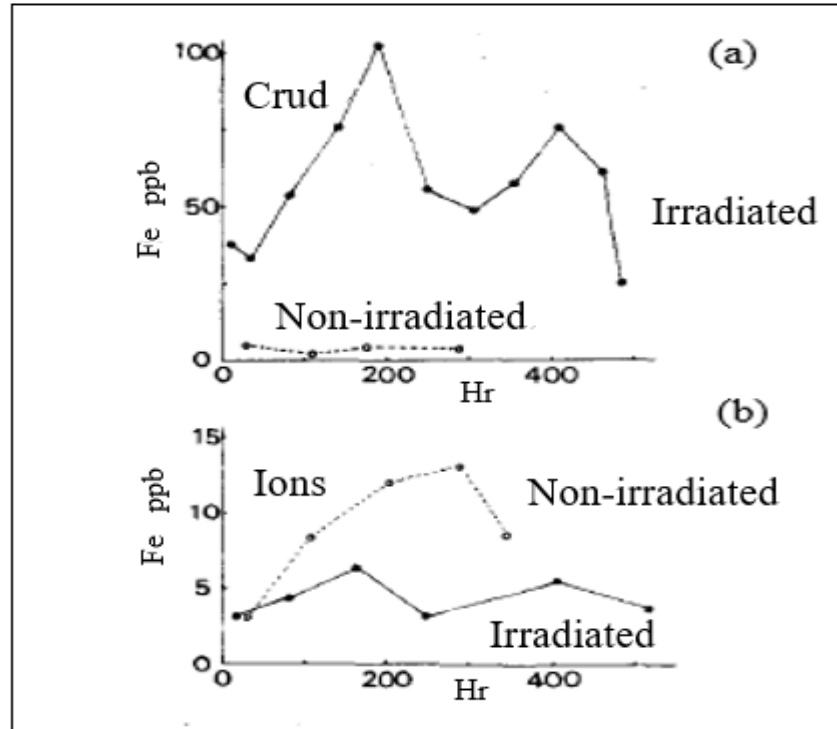


**Figure 2-9: (a) Concentration of iron Crud, (b) Concentration of iron ions from 304 stainless steel in the presence of 20ppb O<sub>2</sub> with a flow rate of 0.33 mL/sec at 250°C. The solid line represents the irradiated exposure, while the dashed line represents non-irradiated exposure [44].**

## 2.6 Application of Research to Nuclear Powered System.

The corrosion of aluminum alloys in the reactor containment has been noted to impact the performance of ECCS of a nuclear-powered system. When an accident occurs in the plant, the excess heat generated at the reactor core needs to be maintained. The ECCS system generates cooling water from the storage tanks and maybe the containment floor, which is pumped through the primary cooling system to reduce the heat generated in the reactor core by using the splash framework [45]. The recirculation pump gathers the containment

spray, reactor coolant, and borated water as the ECCS drain to the containment building floor. The content of aluminum in the containment could be as high as 90%, depending on the reactor type. Previous studies have shown that aluminum corrodes more in post-LOCA solutions than other materials present in containment systems such as ferrous alloy, copper, galvanized zinc and steel, etc. [46].

The corrosion product generated by the corrosion of aluminum coupled with different debris created by the LOCA prompts the obstruction of the sump strainers and recirculation pump, thereby destroying the ECCS [45]. Also, there is a high tendency for triggered fragments to pile-up at the sump strainer and aggravate the dilapidation of the strainers through radiolysis. This occurs when radionuclides in fixed locations (fuel and core structures) or free and movable (either as solids or as broken up species) inside the mixing coolant are emitted. They impinge on these circulating coolants, solutes, solid materials distributed by the coolant, and materials in contact with the streaming coolant. The radiolysis of these coolants produces numerous reactive species, which can affect the redox potential and pH of solid-bearing aqueous solutions resulting after a LOCA [7].

As described in section 2.4.1, water radiolysis results in the production of radicals such as ( $\text{HO}$  and  $\text{H}^+$ ) which will, in general, react with themselves or with other broken up species (e.g.,  $\text{Cl}^-$ , and  $\text{N}_2$ ), forming hydrogen peroxide ( $\text{H}_2\text{O}_2$ ), chlorate ( $\text{ClO}_3^-$ ), hypochlorite ( $\text{ClO}^-$ ), hypochlorous acid ( $\text{HOCl}$ ), nitric acid ( $\text{HNO}_3$ ), and hydrogen gas ( $\text{H}_2$ ). The presence of these radiolysis products affects the debris corrosion rates and containment materials by fluctuating the pH or redox potential of the containment pool.

Nevertheless, the containment pool contains buffer systems that help to keep up the pH somewhere in the range of 7 and 10, accordingly deactivating the pH change of the



radiolysis species. The ECCS provides adequate cooling to the containment, thereby preventing massive fuel failures; therefore, fuel destruction and circulation of fuel particles to the containment pool is not expected. So, the radiolysis encountered here is only related to those activation products distributed by the reactor coolant system, contained solutes, and the particle transported through the flawless fuel and structural materials of the activated core. The dose rate of gamma radiation encompassing the fuel in the reactor vessel is relied upon to be in the range of  $10^4$  Gy/h [7].

The spallation of corrosion products tends to introduce activated species such as  $^{51}\text{Cr}$ ,  $^{58}\text{Co}$ ,  $^{60}\text{Co}$ ,  $^{56}\text{Mn}$ ,  $^{59}\text{Fe}$ ,  $^{63}\text{Ni}$ , etc., to the containment pool. As a result, they accumulate at the sump strainers impacting their corrosion behavior. The dose rate at the sump strainers remains unknown but projected to about  $10^1$  Gy/h. We have about 100 ppm chloride ions present in the ECCS water; various products are formed as radiation interacts with these aggressive ions present in ECCS water, which tends to alter the pH and redox potential of the ECCS. Chloride is an integral part of the post-LOCA coolant and is created by the radiolytic disintegration of electrical cable insulation in the containment building. This electrical cable contains a jacket of Hypalon, which is chlorosulfonated polyethylene having a range of 24 to 43 wt.% chlorine based on the type of Hypalon used [5].

Therefore, if radiolysis species, for example, hydrogen peroxide  $\text{H}_2\text{O}_2$ , chlorate ( $\text{ClO}_3^-$ ), hypochlorite ( $\text{ClO}^-$ ), hypochlorous acid ( $\text{HOCl}$ ), and hydrogen ( $\text{H}^+$  ions and  $\text{H}_2$  molecules) are created in large amounts to modify the redox potential or surpass the pH of the buffering in the containment, an acceleration of the corrosion of debris, and core containment is possible. When a sufficient amount of corrosion occurs because of LOCA,

the increased volume of solids may hinder the sump strainers and impede ECCS performance [7].

To simulate the behavior of these radiolysis products with solutes that may be present in the containment pool, seawater was irradiated with an appropriate gamma radiation field to determine the effect of these radiolysis products on one of the materials (aluminum) present in the containment building. The impacts of radiation can be concentrated tentatively in a post-LOCA condition by presenting the anticipated species resulting from radiolysis based on literature resources [7].

### 3. Experimental Techniques and Procedures

#### 3.1 Materials

The LPBF aluminum sample used in this thesis was produced utilizing a gas atomized AlSi10Mg powder manufactured by EOS GmbH, with a particle size of  $8.8 \pm 7 \mu\text{m}$  on average [47]. For this research, rectangular cuboid AlSi10Mg samples (20 mm x 20 mm x 40 mm) were additively manufactured as shown in **Figure 3-1a** from the powder above utilizing an EOS M290 metal 3D printing machine through the LPBF method (Additive Metal Manufacturing, Inc. (AMM), Concord, ON, Canada).

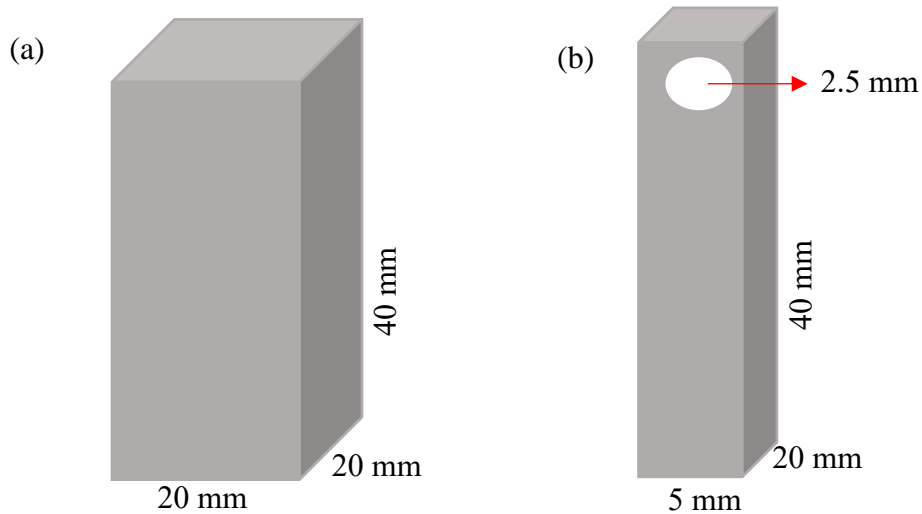


**Figure 3-1: Schematic of view of aluminum alloy (a) bulk aluminum alloy sample, (b) sliced extract of the aluminum alloy samples used for this study.**

The machine used a 400-W Yb-fiber laser, having a spot dimension of  $100 \mu\text{m}$ , with a building dimension of 250 mm x 250 mm x 325 mm size platform. To help reduce the internal stress and oxidation that can occur during manufacturing, the building platform was kept at  $200 \text{ }^\circ\text{C}$  and in argon (oxygen content of 0.1%). The process parameters include

laser power of 370W, scanning speed of 1300 mm/s, hatching distance of 190  $\mu\text{m}$  with the thickness of the powder at 30  $\mu\text{m}$  when strip scanning strategy is used. The rotation for the laser beam is at  $67^\circ$  [47].

Furthermore, a sample cut from the same dimensions (20 mm x 20 mm x 40 mm) aluminum A360.1 diecast ingot block was used for comparative study. The chemical composition of the diecast A360.1 is the closest to AlSi10Mg among all the available aluminum cast alloys. After that, the LPBF samples were machined into four equal parts (5 mm x 20 mm x 40 mm); three were used for the experimental run, while one was kept as a control sample for the descaling. Consequently, the cast block was machined into four equal sizes of (5 mm x 20 mm x 40 mm) and used to perform the experiment, as shown in **Figure 3-1b**.

### 3.2 Irradiation Cell Design

The Irradiation cell was built using various lead (Pb) block shapes at UNB nuclear lab. The source holder was built by cutting a 5 cm thick Pb block, and a rectangular block was made from it, as shown in **Figure 3-2**. The  $4\mu\text{Ci } ^{60}\text{Co}$  was placed inside the Pb block source holder; the source holder has a Pb plug at the back to keep the  $^{60}\text{Co}$  source in a vertical position. Also, a small plug was used to cover the 7 mm hole (not shown in the schematics) to provide adequate shielding when the source was not used and cut down background radiation.

The 7 mm hole created on the Pb block source holder transmits the gamma rays and provides a narrow beam directed to the test cell (beaker), placed 5 cm away. Some of the transmitted rays are absorbed by the test cell; only a small amount of the transmitted rays is subtended by the NaI(Tl) detector.

For appropriate shielding during the experiment, the source holder was housed in a 5 cm thick Pb chamber. The 3" x 3" NaI detector was housed in a Pb castle to minimize background radiation for an accurate reading. The detector was accessed through a Pb door for adjustments, and the Pb  $^{60}\text{Co}$  source holder was placed in line with the NaI detector, as shown in

**Figure 3-3.** It is assumed that the gamma rays penetrating through the test cell (beaker) will fall on the surface of the NaI detector for effective counting.

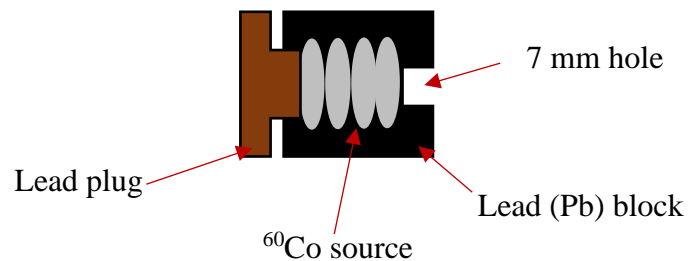


**Figure 3-2: Schematics of the Pb block  $^{60}\text{Co}$  source holder with  $4\mu\text{Ci}$   $^{60}\text{Co}$  source placed inside the lead block.**

### 3.3 Surface Characterisation

#### 3.3.1 Scanning Electron Microscopy (SEM) with Energy Dispersive X-ray Spectroscopy (EDS)

This is a surface analysis technique utilized to examine surface topography and characterize exposed aluminum surfaces and oxides on the surfaces. The elemental analysis was done using the EDS technique, which detects the x-rays emanating from samples bombarded with an electron beam. Field Emission – Scanning Electron Microscopy (FE-SEM) (Hitachi SU-70, Hitachi, Japan) was used to characterize the corrosion attack morphology after corrosion exposure to determine the attack's location relative to the underlying microstructure. (FE-SEM) used an accelerating voltage of 15

kV. Images were acquired using Hitachi PC-SEM software. EDS data were collected with an Oxford INCA X-act SDD detector at 15 kV and a 15 mm working distance. The FE-SEM/EDS imaging was completed at diverse magnifications. A scale bar is displayed on each image.

### **3.3.2 Raman Spectroscopy**

The Raman spectroscopy was utilized to determine the vibrational modes of molecules and describe the chemical composition of aluminum oxidation in seawater conditions. Raman employs a scattering technique to detect how electron cloud changes around the molecule as they encounter light. The source of light which excites an electron to the virtual energy state is monochromatic [48]. The intensity of Raman peaks cannot reliably indicate quantitative amounts of the oxide species. Regardless of this limitation, Raman spectroscopy is a suitable and effective technique for defining oxide species present in the scale, showing great insight into thermodynamic conditions during oxide growth [49]. A Laser Raman Microscope with a 633 nm He-Ne laser (inVia Raman Microscope, Renishaw, UK) was used to analyze the oxide deposit.

### **3.3.3 X-ray Diffraction (XRD)**

X-ray diffraction was employed in this project to ascertain the ratio of secondary phases present within the matrix of AlSi10Mg and A360.1. A Bruker D8 Advance mass spectrometer determined x-ray diffraction patterns for the aluminum block surface with oxide deposits. The metal block was placed and centered on the sample holder such that the surface area was in-plane with the three reference pins of the sample stage. X-ray source was a closed, 2.2 kW copper electron tube, kept at a working voltage of 40 kV and a current of 25 mA.

A computer was used to control the goniometer with autonomous stepping motors and visual encoders for the  $\theta$  and  $2\theta$  circles. Samples scan is within the range of  $10-90^\circ 2\theta$ . A stage size of  $0.02^\circ$  and a stage time of 1.0 sec were utilized throughout the measurements. A Peltier-cooled solid-state [Si(Li)] detector (Sol-X) with a suitable energy range of 1 to 60 KeV was used as the detector.

No rectification was created for K $\alpha$  radiation. A collection of  $2^\circ$  Soller slits were utilized to bring down horizontal beam divergence. The software suite for information assortment and analysis was windows-based. Information assortment was a physically controlled JOB program that utilizes a DQL parameter file. The raw data acquired from the spectrometer were examined and refined by the program EVA (Bruker) [46].

### **3.4 Experimental Procedure**

#### **3.4.1 Solution Preparation**

For solution preparation, deionized water, and analytical grade reagents were used to prepare the solutions used for this study. The sea salt crystals purchased from Carolina Biological Supply Company were added to the deionized water in a necessary volume to make an artificial seawater solution similar to the natural seawater with a pH of 8.20.

The undissolved crystals in the solution were left to settle at the bottom for 20 minutes. The solution was decanted; the undissolved crystals left at the bottom of the beaker were dissolved using 40 ml of dilute concentration of 1:100 (HCl: H<sub>2</sub>O) solution. The pH of the solution was adjusted to 8.20 by the addition of a few drops of sodium hydroxide. All the pH measures were made by the Fisher brand Accumet (AR20) pH/conductivity meter.

### 3.4.2 Polishing and Surface Preparation

Cutting of the LPBF AlSi10Mg blocks was carried out along the building plane (x-y plane) and the building direction (z-direction) into four (4) equal sizes of (5 mm x 20 mm x 40 mm) as shown in **Figure 3-1b**. Similarly, the same sample size (5 mm x 20 mm x 40 mm) was cut from aluminum diecast A360.1 ingot having close chemical composition. The surface was sequentially ground using a Nanotom 1000T Pace Technologies grinder and Struers SiC abrasive paper up to FEPA P# 4000 grit. It was immersed in water and polished to a mirror surface finish using different sizes of 6, 3, 1  $\mu\text{m}$  Buehler diamond paste on polishing cloth Struers MD Mol™. The specimens were rinsed with deionized water, ultrasonicated in acetone to remove debris, and air-dried.

Etching of the surface of the LPBF AlSi10Mg was done using the Keller's reagent (2.5 ml  $\text{HNO}_3$ , 1.5 ml  $\text{HCl}$ , 1 ml of  $\text{HF}$ , and 95 ml  $\text{H}_2\text{O}$ ) for 15 seconds to reveal the microstructure. The diecast A360.1 surface was unetched as the microstructure was visible without etching. The microstructures and composition of the samples were observed and examined using different surface analysis techniques like (FE-SEM), XRD, and Raman Spectroscopy.

### 3.4.3 Gravimetric (Weight Change) Test

Tests were conducted in a one-liter glass beaker containing artificial seawater (ASW) solution of pH 8.20 at room temperature, magnetic stirrer, and sample holders. The magnetic stirrer was used to simulate flowing water. Before exposure, samples were polished and rinsed with deionized water (DI) water, ultrasonicated in acetone for 30 mins (to remove debris from the surface and pores), and dried in the desiccator for 24 hours.

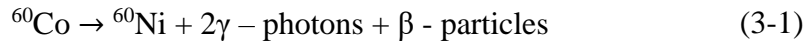


In the absence of radiation, the four-duplicate cast A360.1 samples were suspended into the ASW solution using sample holders insulated with Teflon tubes. The corrosion exposure was for different hours, 24, 72, 144, and 240 hours. The aerated test solution was covered with parafilm to reduce the solvent evaporation and contamination from the environment. The procedure was repeated with three duplicate LPBF AlSi10Mg samples. The samples were weighed pre-and post-exposure to determine weight change and kept in the desiccator after corrosion exposure and surface analysis. Furthermore, the weighed samples were descaled after 240 hours of exposure using (50 ml of  $H_3PO_4$  + 20g of  $CrO_3$  in 1000 ml deionized water and heated to 90°C for 10 min) to determine the total corrosion. A blank sample, which is a bare unexposed sample, was immersed into the descaling solution alongside the exposed samples; corrosion of the blank during the descaling process results in blank correction for the sample measurement. After descaling, the samples were rinsed with abundant deionized water, dried, and then re-weighed. Calculations were carried out to determine the total corrosion of the corroded samples, and blank corrections were applied by subtracting the value of the blank from the corroded sample. Each experimental run was repeated three times to verify the consistency of the results. Surface analyses were carried out at 24 and 240 hours after exposure.

In the presence of radiation, the same exposure sequence was repeated, but the test section was positioned in between the gamma source and a NaI detector, as shown in

Figure 3-3. At the conclusion of each test, samples were taken out from the irradiation test cell for gravimetric analysis and surface analyses. The radiation source was a low dose of  $^{60}Co$  with a dosage rate of 0.40  $\mu Gy/h$  (1 Gy = 1 J retained per kg of water) after the experiment due to radioactive decay and determined by calculations from NaI detector net

peak areas.  $^{60}\text{Co}$  has a half-life of 5.27 years and is known to emit two types of  $\gamma$ -photons with energies of 1173.2 keV and 1332.5 keV.



The  $\beta$ -particle is known to have energy around 318 keV. According to decay rate law, the strength of the  $^{60}\text{Co}$  sources decreases with time; therefore, the absorption dose rate will decrease with time. The dose rate varied from 0.58  $\mu\text{Gy/h}$  to 0.40  $\mu\text{Gy/h}$  for 1008 days as determined from the net peak area calculation using NaI detector [34].

During irradiation exposure, as gamma rays penetrate through a material, some interaction occurs in the material's atom, which slows down the strength of the gamma-ray. The transmission and absorption of gamma rays are based on detecting radiation intensities by the NaI detector with and without the material (test section). The 3" x 3" NaI (TI) scintillation detector (Canberra) and the gamma source are placed on opposite sides of the material on the same axis. The detector and a digital gamma spectrometer count the initial intensity ( $I_0$ ) emitted from the source without any material to calculate the detector response. The materials used for the experiment in the gravimetric cell setup are placed between the source and detector to measure the absorbed dose and intensities transmitted. The absorbed dose for each material is computed and interpreted during the final absorption calculation. The schematic view of the gamma-ray absorption technique is presented in **Figure 3-3**:

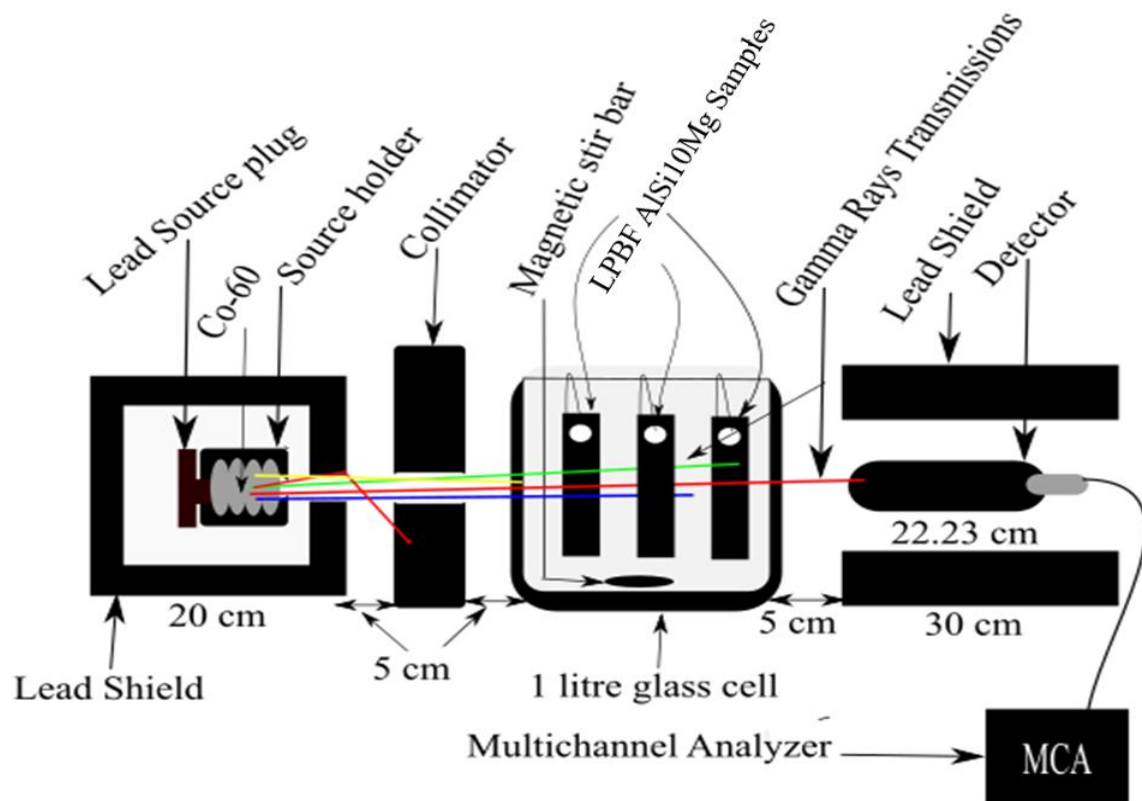


Figure 3-3: Schematic view of the radiation absorption technique.

## 4. Result and Discussion

### 4.1 Surface Characterization of Aluminum Alloys Before Exposure

The surface analysis of aluminum alloys used for this experimental study is described below, starting with the cast A360.1 alloy followed by its counterpart, the LPBF AlSi10Mg alloy.

#### 4.1.1 Cast A360.1 Aluminum alloy

**Figure 4-1** shows the microstructural SEM images of cast A360.1 alloy obtained to determine the various phases inherent in the alloy.

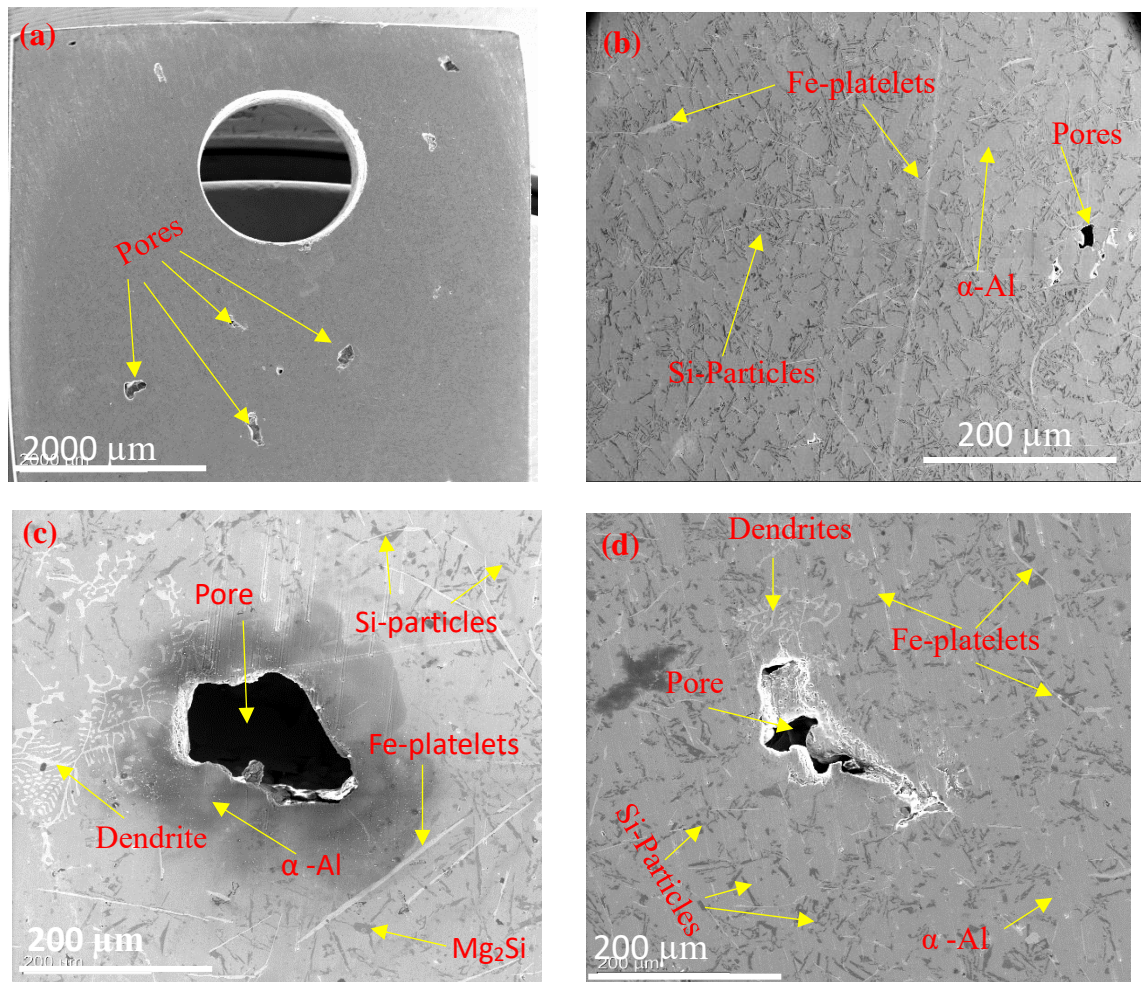


**Figure 4-1: Typical microstructure of cast A360.1 aluminum alloy.**

**Figure 4-1a** shows the SEM images of the cast A360.1 Al alloy in the longitudinal direction. The composition of the alloy presents them in the hypoeutectic range. The base metal  $\alpha$ -Al is formed with dendrites, then the  $\alpha$ -Al + Si solidifies in the process.

The properties of alloys are dependent on the individual physicochemical properties and structure of the main phase ( $\alpha$ -aluminum and silicon particles) and other phases resulting from the alloying element (SiAlFe, SiAlFeMn, Mg<sub>2</sub>Si, SiAlFeMg). Several studies have shown that the subordinate phases are known to affect the strength of the cast alloys and how they resist corrosion when exposed to an environment [50]. The careful alloying and heat treatment help produce the ideal mechanical properties of many aluminum alloys [51]. An undesirable result of this process is that the alloying additions tend to exhibit electrochemical behaviors quite differently from those of the alloy matrix, making the alloy vulnerable to numerous localized corrosion varieties.

One of the primary phase components, silicon, is known to have a low solubility in aluminum, forming coarse precipitates that possess different properties (chemical and mechanical), as shown in **Figure 4-1b and d**. Silicon behaves differently in an aluminum-rich matrix; thus, in the presence of aggressive ions such as chloride, localized corrosion is formed around the interface between Si-particle and aluminum [11]. Dark needle silicon crystals were widely present on the surface of the cast A360.1 at various magnifications.

Iron is present in the microstructure of cast A360.1 as an impurity forming Si-Al-Fe compounds. The volume of silicon in the alloy determines the crystallization behavior of these compounds [50]. Among the various Fe-intermetallic particles formed on cast A360.1, the first to be identified due to the hypoeutectic nature of the alloy is the  $\beta$ -SiAlFe phase. This phase crystallizes as large needles and/or platelets, as shown in

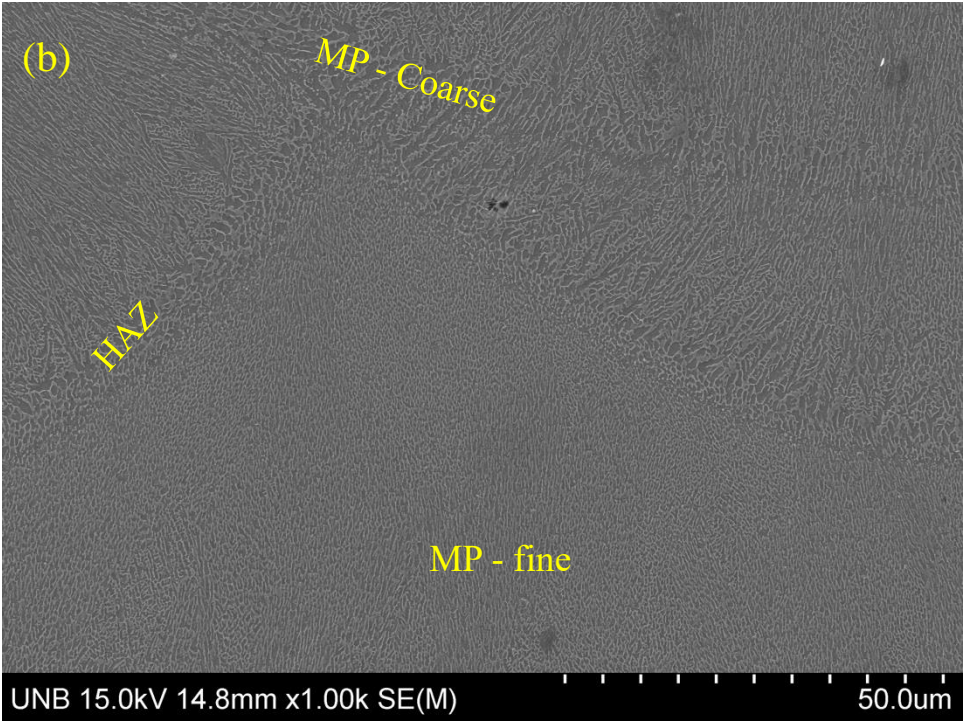
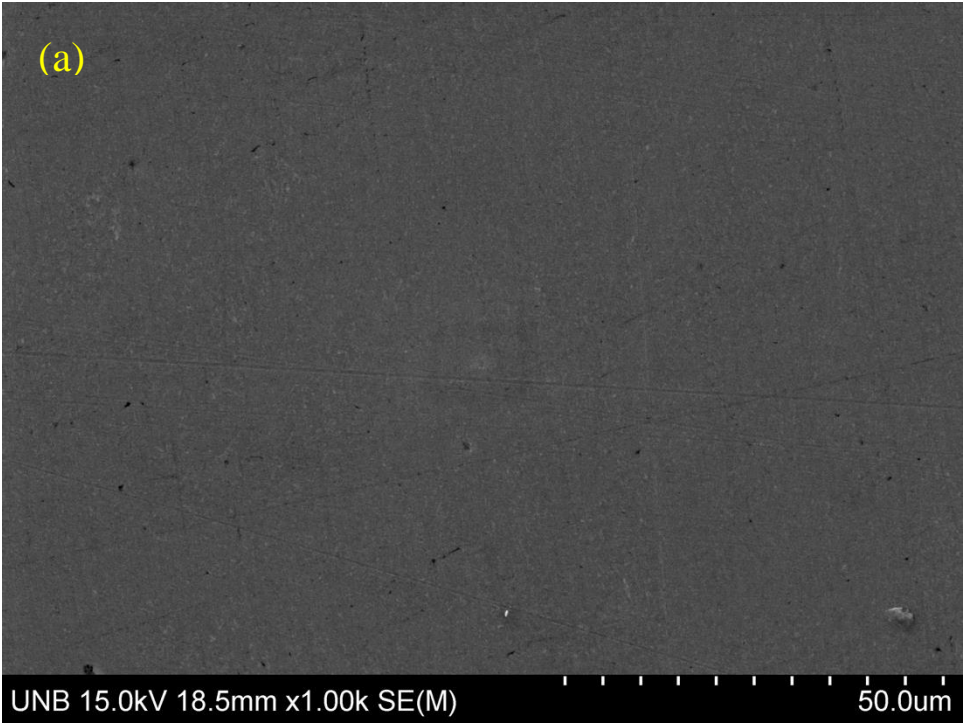
**Figure 4-1b and c**, and the iron content in the microstructure determines the shapes of these platelets. The fragile nature of this phase in the aluminum matrix makes it unstable, contributing to the weakness of the material [52]. In aqueous media, the  $\beta$ -SiAlFe phase is nobler than the Al base, increasing the vulnerability of the alloy to localized corrosion. The incorporation of manganese helps counterbalance the impact of iron on the cast A360.1 and reduce its brittle nature. Many manganese compounds form as a result of this addition, but iron replaces these compounds without any change to the crystal type formed. The most common manganese compounds formed in the absence of copper are SiAlFeMn, (FeMn)Al<sub>6</sub>, and in the presence of copper (CuFeMn)Al<sub>6</sub> and Si<sub>2</sub>Al<sub>15</sub>(CuFeMn)<sub>3</sub>. These compounds have been identified as equiaxed and can solidify in the form of dendrites, as shown in **Figure 4-1c**, thereby eliminating most of the iron embrittling effect. Manganese additionally diminishes the cathodic effect of iron-bearing intermetallic, prompting less strong galvanic couples when equated with other Fe-bearing intermetallic without manganese addition.

Among the effects iron has on the mechanical properties of an alloy, the huge iron-rich needles known to form immediately during the hardening cycle process prevents the movement of fluid metal through feeding channels into the casting compartment, causing unsoundness and porosity, as depicted in **Figure 4-1c and d**. Previous studies have shown that intermetallic compounds, as found in cast A360.1, may regularly show up-close contact with porosity. The compounds formed as a result of Fe bearing intermetallic interaction (SiAlFe and SiAlFeMn) types favor the development of shrinkage porosity by hindering the interdendritic feeding channels of hypoeutectic aluminum-silicon alloys.

This accounts for the numerous pores widely present on the cast A360.1, as shown in **Figure 4-1d**, as well as excess hydrogen present in the molds [52].

Additive manufacturing technologies have been developed to prevent and minimize the precipitation of intermetallic compounds containing iron and will be discussed in detail within the next section. Combining silicon with magnesium is another way of strengthening the diecast A360.1 alloy; this forms the  $Mg_2Si$  phase identified by its spherical shape in **Figure 4-1c**. The  $Mg_2Si$  phase tends to be anodic in the alloy matrix, thereby forming a localized corrosion site as they dissolve into the solution. Magnesium tends to segregate as Si-Al-Fe-Mg, which grows in the shape of dendrites. These newly formed compounds tend to behave better than the compounds that are Mg free in terms of yield strength and hardness. Also, like every Fe-bearing compound, they behave differently from the  $\alpha$ -Al matrix though less harmful than AlFe, SiAlFe, and SiAlFeMn IMPs because of magnesium.

4.1.2 Laser Powder Bed Fusion (LPBF) AlSi10Mg





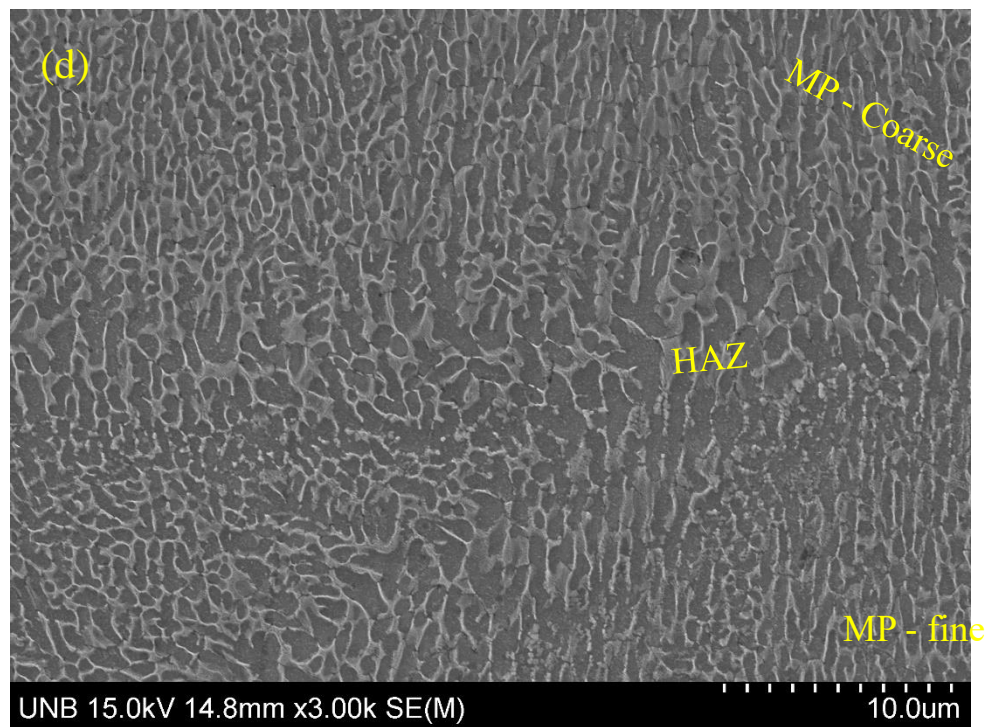
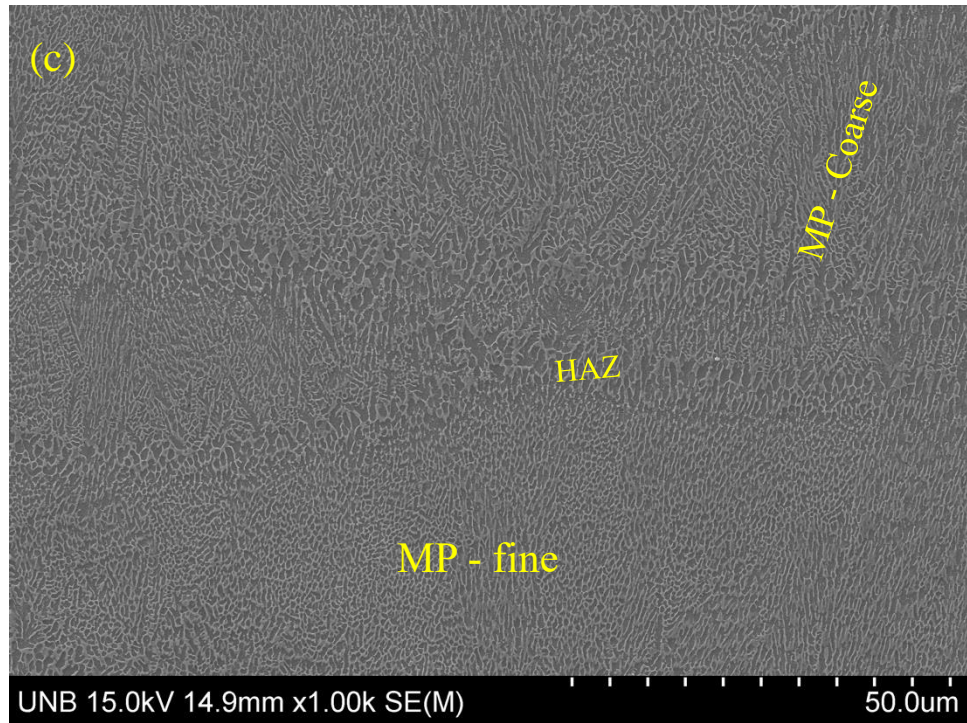


**Figure 4-2: Typical microstructure of LPBF AlSi10Mg (a) unetched featureless microstructure (b-c) etched microstructure showing different zones (d) high magnification of the three zones.**

As shown in **Figure 4-2**, the SEM images reveal the microstructure of LPBF AlSi10Mg to be different from that of the diecast A360.1 described in section 4.1.1. The unetched microstructure shown in **Figure 4-2a** had a featureless surface with no pores or intermetallic particles (IMP) present. The absence of pores or intermetallic particles is because of the quick cooling and hardening behavior of the laser powder bed fusion process ensuing in the formation of the expected hardening structure of a cellular mixture of silicon with  $\alpha$ -aluminum. The presence of IMP as described on the cast A360.1 in section 4.1.1 results in various localized corrosion forms experienced by the cast alloy. In the LPBF samples, the dimensions of such IMP are too minute to influence the corrosion behavior of the alloy; just silicon assumes a role in the corrosion resistance of the alloy.

The alloy was etched using Keller's reagent as described in section 3.4.2 to reveal the microstructure. The detailed microstructural characterization on the longitudinal section of the sample was observed, as shown in **Figure 4-2b-c**. The trails of the melt pool showed discontinuous trails resulting because of the halfway re-softening of the previously deposited powders and non-uniform heat transmission, which leads to depth and shape variation in the melt pool, forming a semicircle-shaped meltpool. The microstructure is described via a cell dendritic structure made from  $\alpha$ -Al solid solution and interdendritic Si particles.

As shown in **Figure 4-2b-c**, three distinct areas with specific microstructures were observed over the melt pool in the longitudinal direction after etching. They are the region formed towards the center of the melt pool with finer microstructure (MP-fine). Regions where a coarse cellular structure (MP-coarse) formed, and areas coarsening the Si phase into idiomorphic crystal formed from the already set layer comprising the broken

intercellular system – heat-affected zone (HAZ). These three zones can be described as follows:

- (a) Fine zone – this shows most of the total fine-grained melt pool. At the center of the trails formed by the laser radiation are cellular dendrites.
- (b) Coarse zone – the coarse zone is formed at the edges of each melt pool. They contain a larger grain size of the silicon network but are usually broken and widely distributed on the matrix of the  $\alpha$ -Al cells [53].
- (c) Heat affected zone (HAZ) – the HAZ is the region where the grains experience variations in temperature changes below the melting temperature. Most of the network formed is broken at the intercellular phases, but we can still locate the networks and tracks formed by the laser radiation [54].

In a critical assessment of the microstructure over the melt pool, the LPBF alloy exhibits a unique microstructure due to a high cooling rate and temperature changes when this alloy solidifies. The  $\alpha$ -Al phase shows a stretched dendritic microstructure across the longitudinal area, and the size of the microstructure is because of the quick cooling rate and thermal gradients.

The coarse zones in **Figure 4-2d** are formed as a result of these two reasons below:

1. The Gaussian movement of the laser radiation changes the rate at which the melt pool remains in liquid form below the solidification point. At this point, various chunks of different sizes start to form, contributing to the formation of the alloy's microstructure. In general, changes in temperature (G), rate of solidification (R), and undercooling ( $\Delta T$ ) provide insight into the shape and size of microstructure. The fine

nature of the melt pool is determined by the  $G * R$ -value, which prompts the coarse zones to form at the melt boundary. [54], [55].

2. As a result of the continuous melting and solidification of the materials, the size of the melt pool continues to increase [56]. Liu [56] opines that the semi-solid state might cause the coarse zone formation during the melting of the next layer. There is a change to a globular structure by the primary  $\alpha$ -Al phase dendrite, and the small structure of the fine zones emanates from the absence of the secondary dendrites. The coarse nature of the base metal stems from the reheating of the semi-solid metal. The HAZ temperature is lower than the solidus, and the laser beam does not affect the base metal. Maintaining a high temperature is short for the base metal because of the laser speed and the high cooling rate. The Si cell's microstructure changes only in tiny regions affected by the high temperature.

**Figure 4-2d** displays the microstructure LPBF AlSi10Mg at a higher magnification. The face-centered cubic aluminum cells were covered with a persistent Si pool network formed around the intercellular area coming about because of high cooling rates. These Si networks with coarse dendritic microstructure helped improve the corrosion resistance of alloys manufactured using the LPBF process.

#### **4.1.3 Phase Analysis of cast A360.1 Aluminum Alloy**

**Figure 4-3** displays the X-ray diffraction shapes of as-cast A360.1 alloy. The diffraction peaks of  $45^\circ$ ,  $65^\circ$ , and  $78^\circ$  indicate the presence of the aluminum phase. The x-ray peaks for silicon particles appeared at  $28^\circ$ ,  $47^\circ$ ,  $55^\circ$ , and  $88^\circ$  ( $2\theta$ -angle). The intensity of the aluminum peaks is higher than that of silicon peaks due to the small grains of silicon particles and the more random orientation of the eutectic Si. Intermetallic particles are

widely present on the cast microstructure, but the peaks corresponding to these IMPs have lower intensity due to their low volume fractions. It was not possible to detect the IMP peaks using XRD because they are assumed to be below the detection limits.

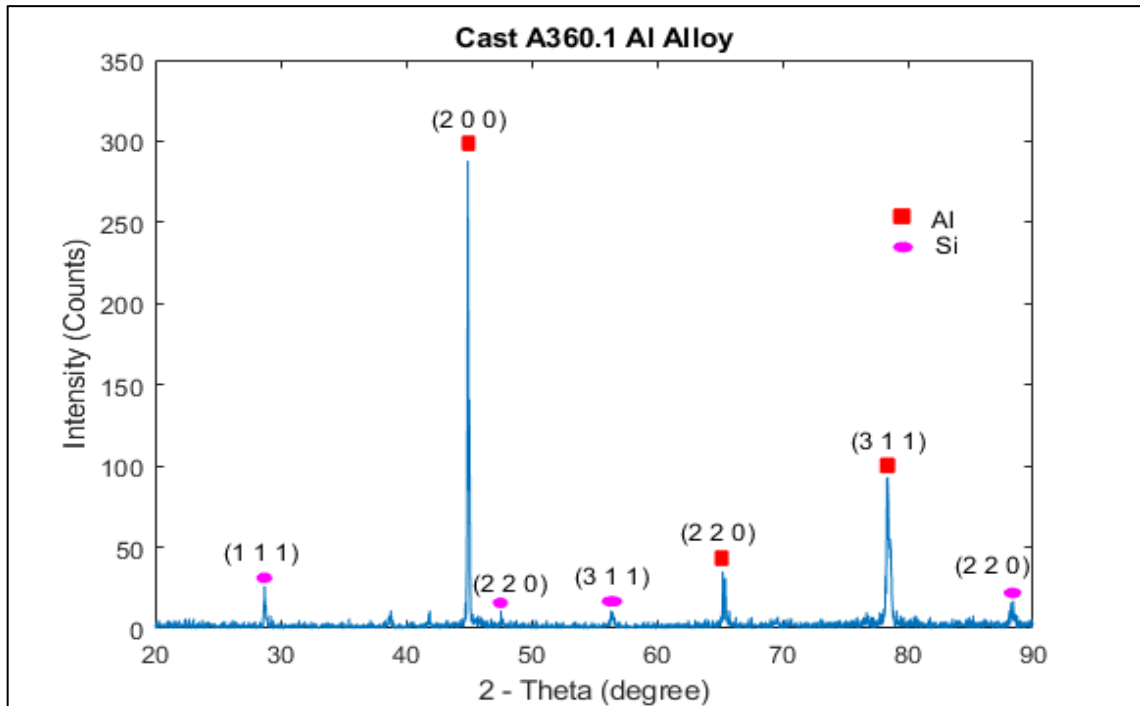


**Figure 4-3: X-ray diffraction patterns of cast A360.1 aluminum alloy before exposure.**

#### 4.1.4 Phase Analysis of LPBF AlSi10Mg

The phase composition of LPBF AlSi10Mg samples was determined by X-ray diffraction analysis utilizing a Bruker D8 Advance spectrometer. As seen in

**Figure 4-4**, aluminum and silicon peaks are shown in the same pattern as other XRD patterns widely reported in the literature for the LPBF AlSi10Mg components [47], [57], [58]. The peaks of the Si diffractions appeared to be weak and broad, suggesting a proportion of the Si content is retained in the  $\alpha$ -Al matrix. The XRD pattern taken from a

different position on the alloy surface is identical to those obtained from previous studies. In all cases, the Al (111) peak showed the highest intensity after the Al (200) peak, with the Al (220) and Al (311) planes having lower peaks.

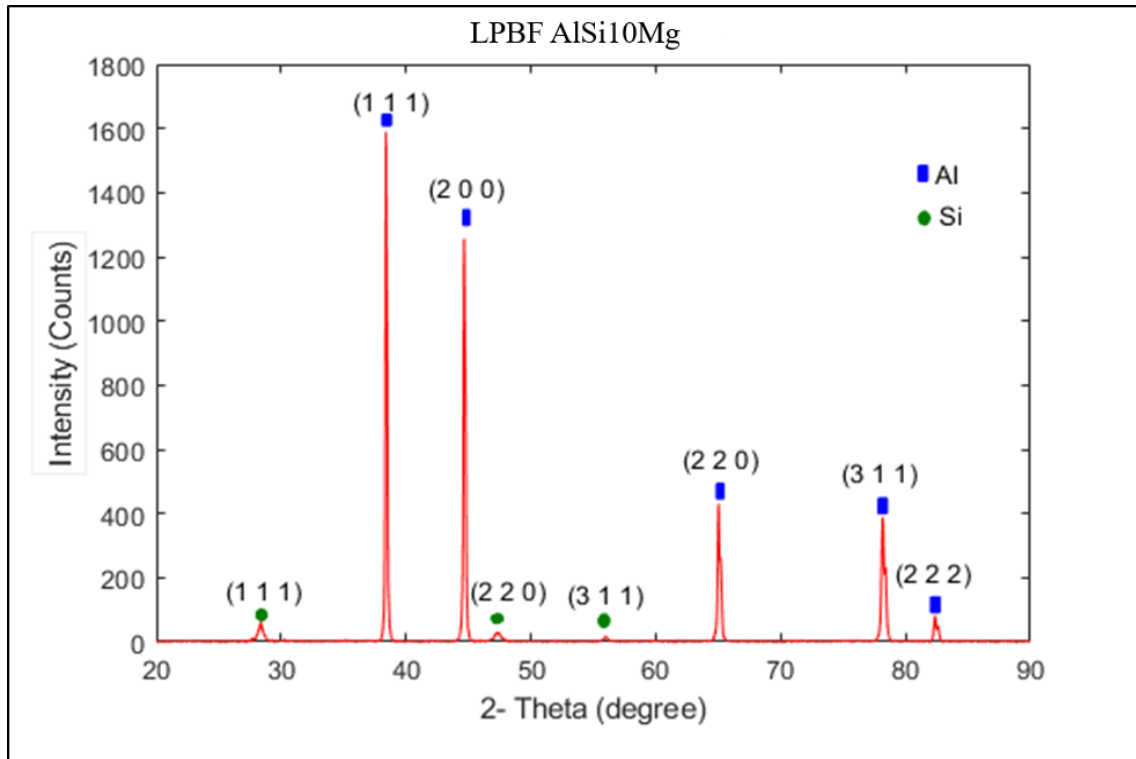


**Figure 4-4: X-ray diffraction patterns of LPBF AlSi10Mg aluminum alloy before exposure.**

#### 4.1.5 Raman Spectrum of cast A360.1 Aluminum Alloy

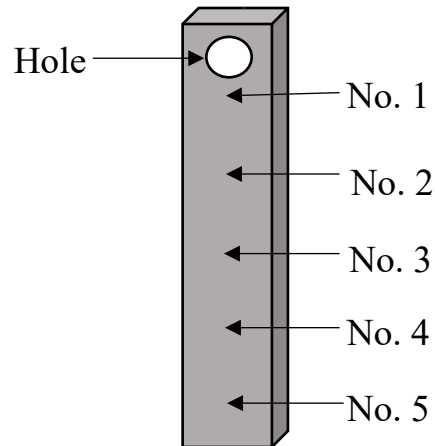


**Figure 4-5: Raman spectroscopy analysis areas.**

Several Raman spectra analyses were obtained from the sample surface areas, as shown in **Figure 4-5**. The dominant peaks from these five analyzed areas were (522, 1556, and 2330  $\text{cm}^{-1}$ ). **Figure 4-6** shows a representative Raman spectrum of one of the regions analyzed for a polished cast A360.1 before exposure to the ASW solution. The Raman peak at 520  $\text{cm}^{-1}$  is attributed to monocrystalline Si, but a slight peak shift moved the peak position to a slightly higher position of 522  $\text{cm}^{-1}$ , as shown in **Figure 4-6**. These peak shifts could be attributed to the solidification behavior of the alloy resulting in the coarse microstructure and numerous pores on the surface of the alloy. The peak at 1556  $\text{cm}^{-1}$  could be assigned to graphitic carbon [59], while peak 2330  $\text{cm}^{-1}$  remains unidentified.

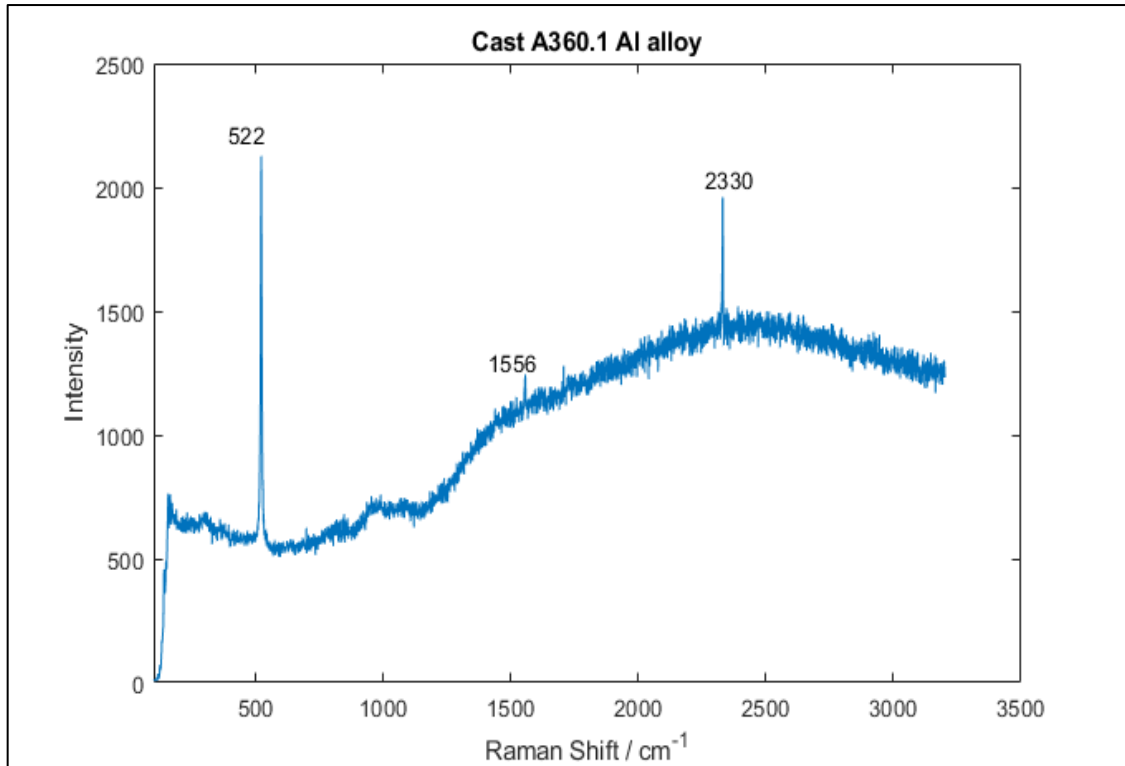


**Figure 4-6: Raman spectrum of cast A360.1 aluminum alloy before exposure.**

#### **4.1.6 Raman Spectrum of LPBF AlSi10Mg Aluminum Alloy.**

The representative Raman spectrum of polished LPBF AlSi10Mg alloy is presented in **Figure 4-7** below, as several spectra were obtained from different areas on the sample, as depicted in **Figure 4-5**. The Si peak at  $520\text{ cm}^{-1}$  was absent on this alloy. This may result from LPBF alloy solidifying rapidly and particles being evenly distributed within the alloy matrix. Therefore, the silicon particles appear Raman-inert in this. The absence of Si peaks on the Raman spectrum looks strange as the Si network tends to form on the alloy microstructure improving its corrosion resistance. Peak  $1556\text{ cm}^{-1}$  is assigned to carbon impurities depositing on the alloy from the polished materials [59], while peak  $2330\text{ cm}^{-1}$  remains unidentified.



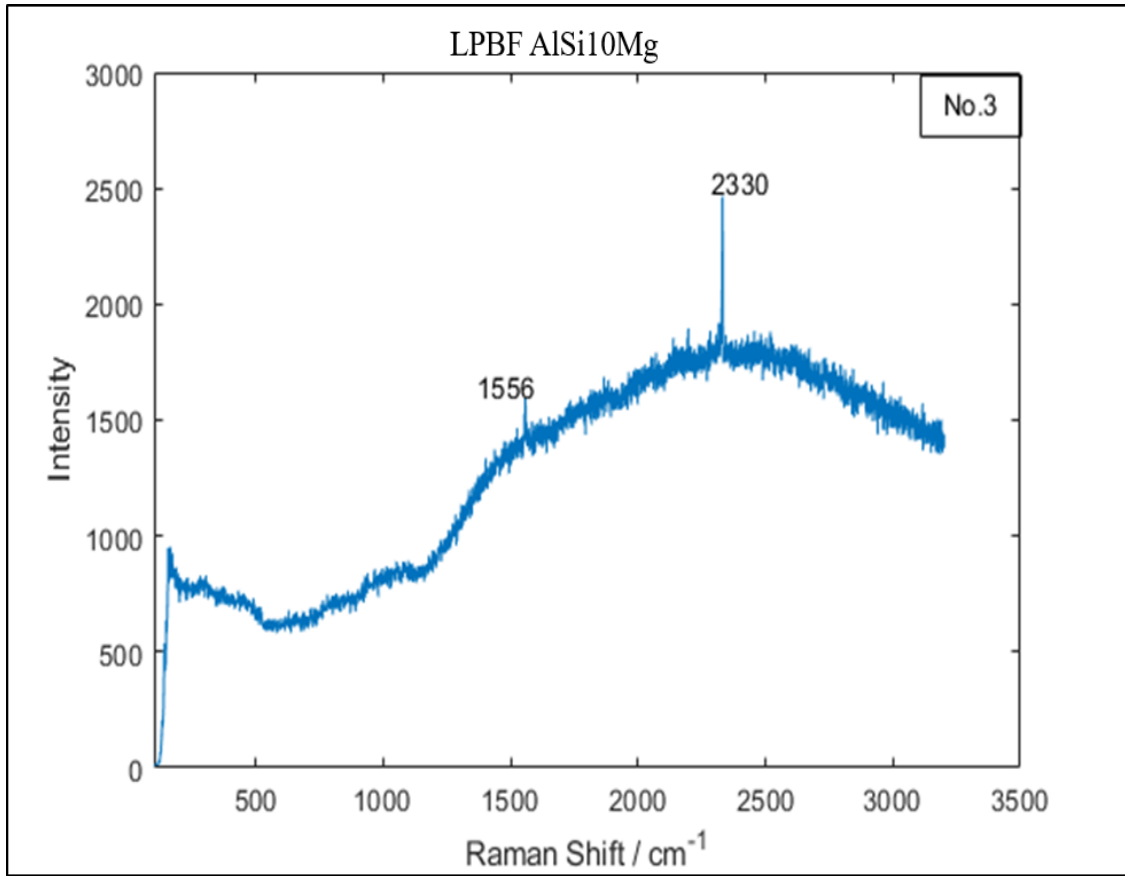


**Figure 4-7: Raman spectrum of LPBF AlSi10Mg aluminum alloy before exposure.**

## 4.2 Gravimetric Analysis

### 4.2.1 Non-Irradiated and Irradiated cast A360.1 Results

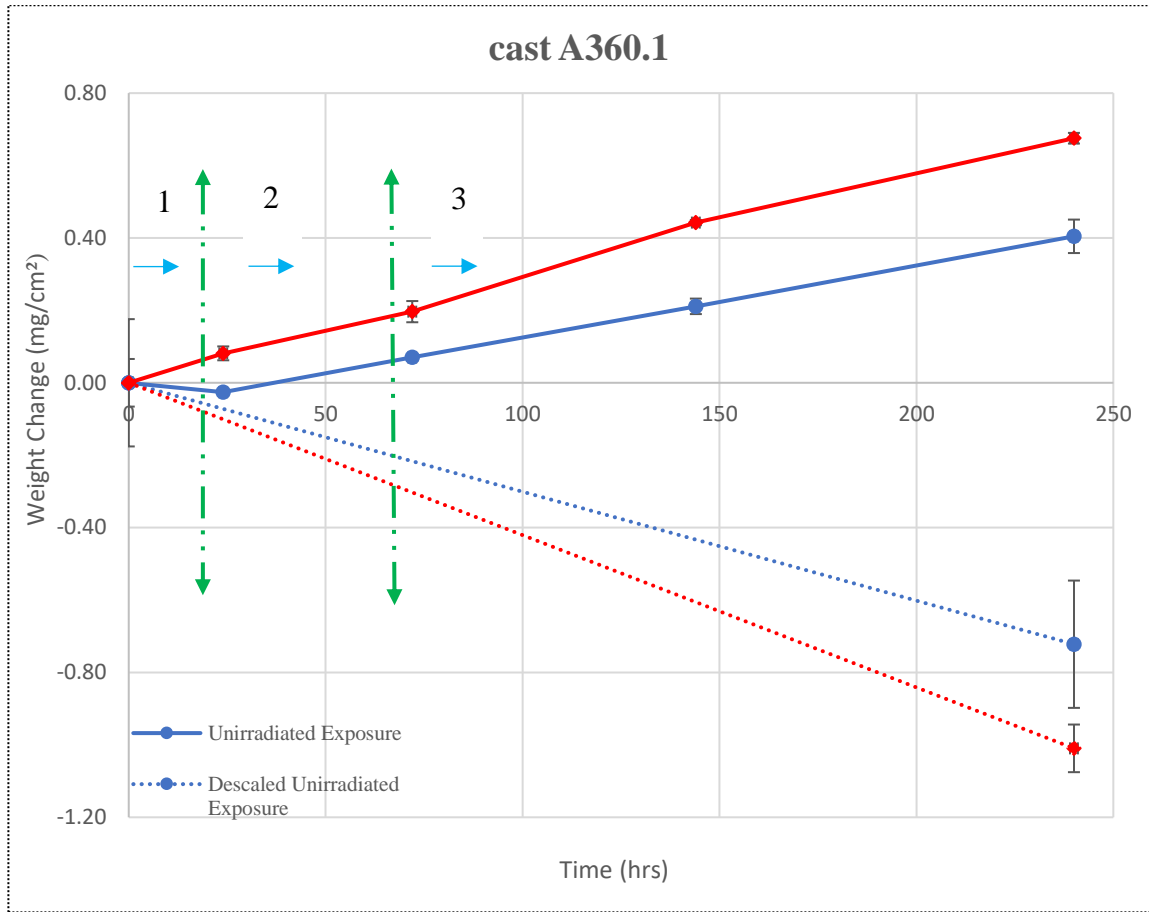


**Figure 4-8: Weight change of cast A360.1 aluminum alloy. The solid line represents experiment data; the dashed line without arrows represents descaled results, and the dashed thick green lines with arrows represent the zones. Some error bars are smaller than the graphs point size, while others are not.**

The result for the cast A360.1 in the presence and absence of radiation is presented in **Figure 4-8** above. The obtained results show the alloy to be corroding under three different zones, and these zones behaved differently in the absence and presence of radiation.

In the absence of radiation, the cast A360.1 alloy showed a gradual weight loss within the first 24 hours of exposure representing the first zone. This behavior could be ascribed to the aggressive attack of the intermetallic particles present in the alloy on exposure to artificial seawater solution before protective oxides are formed on the alloy surface. This finding was buttressed by the work of Brown et al. [60], who stated that exposing aluminum to an aerated solution leads to an initial rapid attack in the first exposure. A reduced attack is noticed when film forms on the aluminum surface, reducing the diffusion rate of dissolved oxygen and aggressive ions to the metal matrix.

The gradual build-up of an oxide deposit, which started in the second zone (72 hours exposure), is expected to reduce these attacks. Scattered non-uniform oxide patches are formed on the alloy surface as oxygen begins to approach the alloy surface from the aerated seawater, but the oxides formed are still tiny to mitigate these attacks. On continuous exposure at the third zone, starting from 144 hours and continued to 240 hours, consistent oxide flakes formed on the alloy surface leading to an increased weight gain on the alloy. This increased weight gain may reduce oxygen diffusion to the metal surface, slowing metal corrosion. However, there is a high chance of penetrative attacks by aggressive ions present in seawater with small diameters (such as chloride ions, etc.), enables it to penetrate through layers at the end of the second stage. After 240 hours of exposure, the oxide deposit continued to increase; it is expected that the oxygen diffusion to the alloy surface will be limited. The insoluble oxide deposits began to spall off and fall into the solution as a result of the constant flow of the solution. The penetration of aggressive ions to metal surfaces continues at this stage as the oxide deposit is not uniform as some parts of the samples remained visibly bare.

The plots above contained the values of descaled samples in the absence and presence of radiation. In the absence of radiation depicted as the dashed blue line on the plot, the sample was descaled as described in section 3.4.3 with reagents after 240 hours of exposure. The result showed an increased attack by the aggressive ions present in seawater. As the oxide deposit on the alloy continued to increase after 24 hours, one would think the oxide deposit was preventing the alloy from further corrosion, as reported by Ezuber [61], but that was not the case here. The oxide deposit was not uniform on the alloy surface as it had many defects, which allowed attacks from aggressive ions in the seawater to continue. These aggressive ions penetrate through oxide defects and react with the metal/oxide interface, resulting in some local corrosions, such as pitting and intragranular corrosion. Some of these aggressive ions in seawater, such as chloride ions, etc. are known to have a small diameter in the nanometer scale, allowing for easy penetration and interaction with the metal surface [62]; this explains the increased forms of aggressive attack seen on the alloy interface after descaling. A blank correction was applied to the corroded samples to determine the rate of attack from the descaling reagent. The result of the blank correction was insignificant as the descaling reagent did not affect the metal matrix.

After each exposure time, experimental runs were stopped, samples weighed, stored in the desiccator awaiting the next experimental run. Each of the points noted on the weight increment against the time graph above shows an average of four samples of similar dimensions for three experimental runs, and the standard error bars of these runs are shown in the plots above.

In the presence of radiation, the alloy exhibited a different behavior in the first 24 hours of exposure representing the first zone; a higher oxide deposit was formed on the sample compared with non-irradiated samples. This increased oxide deposit in the first few hours of exposure could be attributed to the interaction with the product of water radiolysis as the oxygen diffusion rate increased due to radiolysis. As noted earlier in section 2.4.1, the interaction of radiation with water breaks down water molecules, which recombine after a few seconds based on the intensity of the radiation. This breakdown prompts the formation of oxidizing species such as ( $O_2$ ,  $H_2O_2$ ,  $OH$ ,  $HO_2$ ) and reducing species ( $H_2$ ), which further recombines with the solutes present in the solution forming the increased oxide deposit as noticed from zone 1 of the plot above.

The second zone occurred at 72 hours of exposure; it showed a steady increase in the oxide deposit but not as rapid as was noticed in the first stage due to the behavior of the long-lived oxidizing agents formed in the solution. The long-lived oxidizing agent continues to accumulate in the solution to the extent it becomes saturated and levels off at longer exposure hours. The long-lived reducing agents ( $H_2$ ) continue to be released into the gaseous phase.

In the last zone occurring between 144 hours to 240 hours of exposure, the oxide growth on the alloy continues to grow at a steady pace. The type of irradiation used for this experiment does not cause any structural defects on the alloy. However, it causes defects in the oxide film by changing the passive films' chemistry formed on the alloy surface. Due to this impact in the oxide film, the diffusion rate of aggressive ions through the oxide defects increased as they combined with water radiolysis products; this was noticed on the alloy surface after descaling.

After descaling, an increased form of localized corrosion attack was revealed on the alloy surface more than noticed in the absence of radiation, which can be attributed to increased radiolytic attack on the alloy surface because of deformities in the oxide deposit. Aluminum alloys are readily oxidized and corrosion-resistant based on the oxide deposits or film formation on the alloy. However, based on the thickness of the oxide deposits, the strong resistance of aluminum to corrosion was stifled due to defects formed on the oxide deposits leading to the transport of aggressive ions to the metal/oxide interface forming various forms of localized corrosion. This aggressive attack was evident after descaling as the irradiated alloy was corroding ~ 40% more than the non-irradiated alloy while accumulating ~49% more corrosion product.

In conclusion, the curves proved that the nature of the attack on both alloys exposed under the different conditions followed a similar pattern. They showed that the oxidation of aluminum alloys in seawater is affected by low dose  $\gamma$ -radiation. The irradiated samples showed an increased weight gain after exposure, meaning that irradiation increased the thickness of the oxide deposit on the sample more than non-irradiated samples. The irradiated oxide layer formed on the sample appeared uniform compared with the nonuniform film formed by non-irradiated samples, but this does not prevent increased attack by the aggressive ions, as discovered after descaling. The irradiated sample showed a ~ 40% corrosion after descaling more than the non-irradiated and accumulated ~ 49% more corrosion product. The result showed that despite the increased deposition of the corrosion product due to radiation, the alloy still corroded more than the non-irradiated alloy. The rate of attack along the grain boundary layers increased.

#### 4.2.2 Non-Irradiated and Irradiated LPBF AlSi10Mg Results

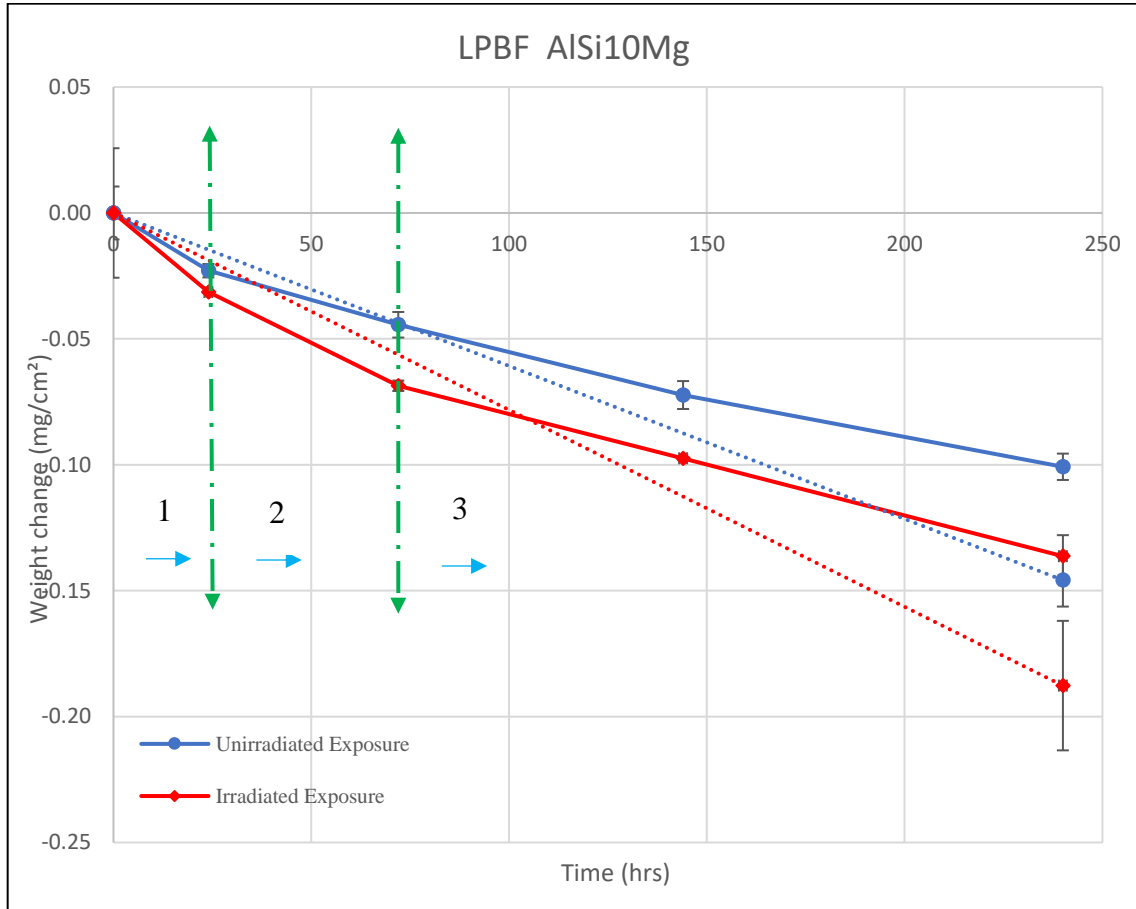


**Figure 4-9: Weight change of LPBF AlSi10Mg aluminum alloy. The solid line represents experiment data; the dashed line without arrows represents descaled results, and the dashed thick green lines with arrows represent the zones. Some error bars are smaller than the graphs point size, while others are not.**

**Figure 4-9** above shows the weight loss results of the LPBF AlSi10Mg aluminum alloy after 240 exposure hours in an artificial seawater solution (ASW). The figure above shows the corrosion behavior of LPBF to be different from its cast counterpart because the cast alloys showed a high weight gain. The LPBF alloy corroded in three stages, as shown above, in the presence and the absence of radiation.

In the absence of radiation, the LPBF AlSi10Mg Al alloy showed an initial weight loss of few milligrams as a result of the interaction of the alloy with aggressive ions present in seawater as no protective oxide film formed at this zone also reported by Brown et al. [60]. After polishing, the alloy showed a mirror-like surface finish but lost its metallic luster as thin-film grayish-yellow colorations began to form on the alloy surface at this first zone. The grayish-yellow coloration forming on the alloy surface observed visually was not distributed uniformly on the alloy but could be seen sparsely distributed at these alloys' solidification layers when some layers were still visible.

On further exposure, the second zone of this experimental run begins at 72 hours of exposure. The film intensity increased slightly in the second stage because the characteristic luster was lost as the yellowish coloration disappeared, leaving a grayish layer on the metal surface. Thin films appeared on the surface of the alloy. They could not prevent the alloy from further corrosion as the aggressive ions were still able to penetrate through the layer and further increased the LPBF AlSi10Mg surface's deterioration.

The third zone of this trial took place at 144 hours of exposure and continued until the termination of the trial at 240 hours. At this stage, the alloy further deteriorated, and the darkening of the alloy surface became very evident and more intense compared with previous exposure hours because it became difficult to see the polishing lines and solidification layers. The result indicates that some forms of localized corrosion occur on the alloy surface even though no pitting was visible to the naked eye during all these exposure hours. Aluminum is known to form thin films on exposure to air or aqueous medium, which tend to be protective [29], but the film formed on the alloy surface, which appeared so dark after 240 hours, was so thin and uniform.



Aggressive ions such as chloride and sulfate ions break down these passive films easily, attacking the alloy substrate,  $\text{Al}^{3+}$  is highly soluble, and interaction with aqueous medium prompts the degradation of the alloy surface. The small diameter of chloride ions allows penetration through thin films, accelerating the corrosion of this alloy [63].

In summary, the data plot of the LPBF AlSi10Mg in the absence of radiation showed a steady weight loss, which could be credited to the inability of the alloy to form a thicker protective film limiting the transport of aggressive ions to the metal/oxide interface. In determining the extent of this attack, the LPBF alloy was descaled, and the result obtained shows a corrosive attack on the alloy surface after descaling.

As depicted in **Figure 4-9** above, the alloy exhibited similar behavior in the presence of radiation, and the rate of deterioration followed the three-zone pattern. There was a slight increase in attack at each exposure zone. At zone 1, the interaction of the alloy with seawater and radiation leads to an increased presence of oxidizing and reducing agents in the solution reacting with the alloy. The interaction of LPBF alloy with radiolytic products and aggressive ions present in seawater further increased the surface attack. The thicker oxide deposit experienced by the cast A360.1 alloy in the presence of radiation was absent on the LPBF AlSi10Mg. An increased weight loss was noticed when compared to the absence of radiation in the LPBF AlSi10Mg sample. The microstructure of the LPBF-AlSi10Mg is composed of  $\alpha$ -Al phase and interdendritic Si-network without any impurities, as found in the cast alloy. This could be one reason for an increased attack at the alloy surface because the presence of radiolytic products increased the transport of redox agents to the metal matrix, increasing the attacks around the Si-networks.

Zone 2 of exposure, occurring at 72 hours, showed an increased attack on the alloy surface. The second stage is controlled by oxygen diffusion, as described by Melchers [64]. It is expected that an oxide deposit becomes visible at this stage with increased thickness preventing the penetration of oxygen to the alloy surface. For an LPBF alloy, films formed on the alloy surface were too thin to stop the migration of oxidizing agents to the metal surface, leading to a continuous weight loss of the samples due to increased oxidant in the seawater solution. As described in (section 2.4.1), the radiolysis of aqueous solutions forms long-lasting oxidizing agents such as  $O_2$ ,  $H_2O_2$ ,  $OH$ , and  $HO_2$  radicals and reducing agents  $e_{aq}$ ,  $H$ , and  $H_2$ , etc. Water radiolysis products can form at any site in the solution, even at the diffusion layer, where the mass transfer occurs. The radical concentration in the bulk solution tends to increase; the reaction between the molecules of dissolved substances and radicals occurs due to the nature of the diffusion process. This explains the further deterioration of the alloy surface at zone 2 of this trial.

Therefore, radiation accelerated the corrosion of LPBF AlSi10Mg alloy exposed to seawater solution due to increased redox products present in the solution. These redox products facilitated the cathodic process, increasing the concentration of substances acting as cathodic depolarizers [65].

At Zone 3 of this experimental trial (144 - 240 hours), there was a continuous increase in metal corrosion, as shown in the data plots in **Figure 4-9**. There was a steady increase in the presence of irradiation when compared with non-irradiated exposure of the two exposure hours, which can be attributed to the leveling off of radiolytic species at longer exposure hours. The continuous weight loss encountered at this stage could be attributed to irradiation continuously influencing the thin film produced on this alloy.

The thin film became darker at this stage compared with previous exposures due to saturation and stability of radiolytic species like  $\text{H}_2\text{O}_2$  at longer exposure hours. The continuous effect on the thin film means there is an increased diffusion of various constituents through the film as spalling takes effect, thereby increasing the weight loss. Components like oxygen, chloride ions with their low diameter can easily penetrate through this film, increasing the deterioration of the alloy surface. Chloride ions can accept free radicals forming various products of oxidized chlorine such as chlorate ion ( $\text{ClO}_3^-$ ), hypochlorite ( $\text{ClO}^-$ ) and hypochlorous ( $\text{HOCl}$ ). The corrosion rate of the alloys can be affected by changes in the pH and redox potential of aluminum alloys when radiolytic species are present. Irradiation had a small effect on the pH of the solution, as described in section 4.7. The cast A360.1 alloy experienced this behavior as well.

The overall effect of these radiolytic products on the alloy surface can be determined by descaling the LPBF alloy after 240 hours of exposure and blank correction applied to determine the impact of descaling reagent on the metal matrix. The results of the descaled samples showed an increased attack on the alloy surface. There was a ~ 29% increase in weight loss after descaling and accumulating a total corrosion product of ~ 14% on the alloy surface. Thus, it confirms that the darker film formed on the alloy surface as exposure time increased was not enough to inhibit the deterioration of the alloy. The blank sample results showed no significant attack on the metal matrix from the descaling reagent, and the results were negligible.

To sum up, water radiolysis products facilitated the cathodic processes and the anodic evolution of hydrogen into the gaseous phase because the experiment was exposed to the atmosphere. This further accelerated the corrosion of the LPBF alloy from the first

exposure time to the end of the trial. As reported above, chloride ions react with free radicals forming various types of oxidized chlorine and other likely constituents, enabling the ionization of anodes and increased dissolution of the alloy.

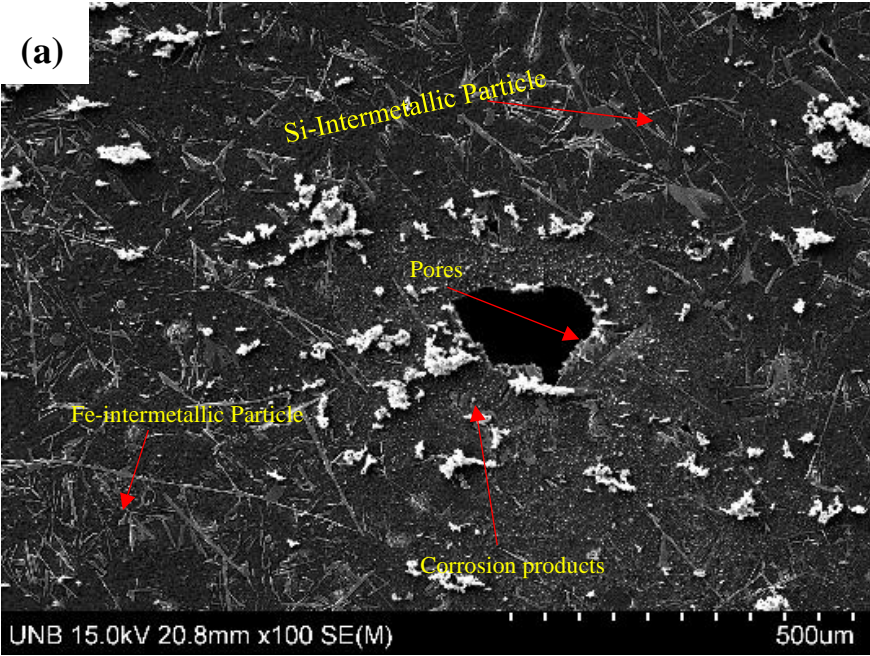
When all these effects react with a highly reactive cathode, it leads to significant deterioration of this alloy, as noticed after the descaling of the alloy. The results revealed the extent of the attack and accelerated effects of radiolytic products on the aggressive ions already present in the alloy solution. Therefore, the behavior of both alloys (LPBF and cast A360.1) in the presence of radiation is different, with the LPBF alloys showing a consistent weight loss and its cast counterpart showing an increased weight gain. The difference in the behavior of both alloys can be attributed to the different manufacturing procedures used, resulting in different microstructures of the alloys. Further explanation of the various forms of localized corrosion found on this alloy is in section 4.3.

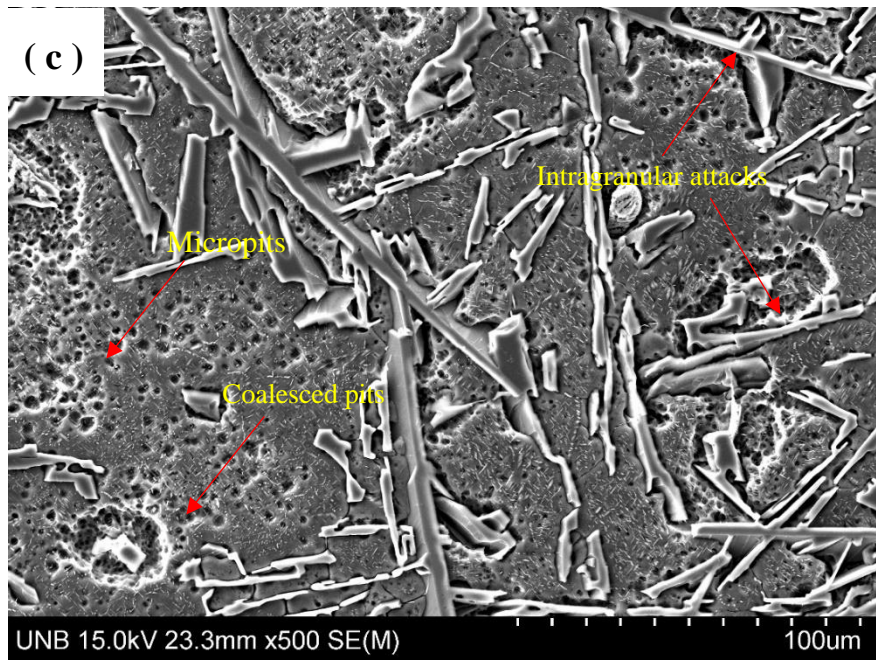
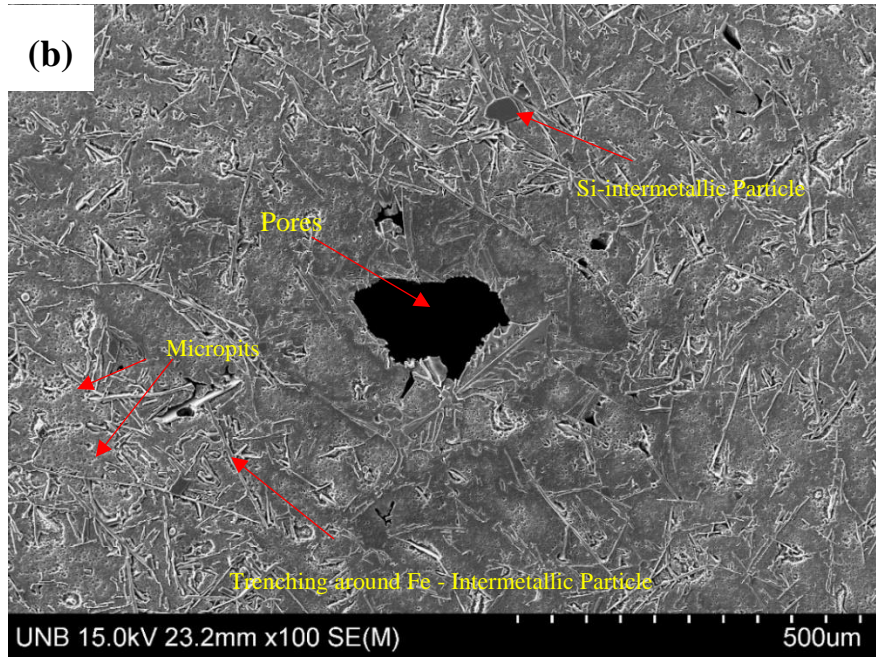
#### **4.3 Corrosion Behaviour of cast A360.1 Exposed in The Absence of Radiation.**

This section shows the surface analyses and micrographs of cast A360.1 aluminum alloy exposed to seawater solution in the absence of radiation. It intends to compare the different morphological features after seawater exposure to comprehend the corrosion pathways of the alloy. The surfaces of the samples at the end of 240 hours exposure are shown in **Figure 4-10**; the samples were cleaned with acetone to remove loosely attached deposits.

**Figure 4-10** micrographs show the corrosion features of cast A360.1 aluminum alloy in the absence of radiation. The cast A360.1 lost its original bright metallic color, with spots visually identified as corrosion products (CP) distributed on the surface, as found in **Figure 4-10a**. The corrosion product deposits on the alloy surface appeared to be

amorphous, porous, and scattered, which can aid the adsorption of bicarbonates in the seawater, forming various types of CP deposits on the alloy surface. It is widely reported that exposing aluminum to air leads to the development of a thin, uniform, and compact oxide film [62]. The SEM images show that CP deposits on the alloy surface do not follow this pattern as the surface deposits are not uniform. The greater part of the surface appears visually not to have any deposit.





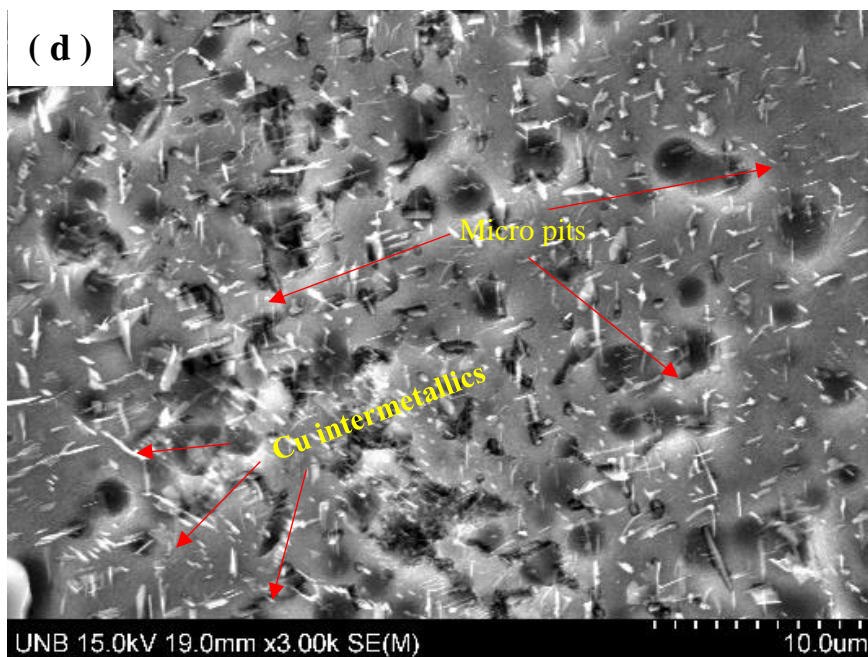


**Figure 4-10: SEM images of cast A360.1 exposed in the absence of radiation. (a) corrosion product deposit after 240 hours exposure, (b) result of descaled (a), (c) high magnification image of intermetallic particles, (d) higher magnification image of micropores and Cu intermetallic.**

The thickness of the CP deposits increased with immersion time in seawater and continued to increase until the end of the experiment at 240 hours, as depicted by the weight change result in **Figure 4-8**. It was observed that some of the loosely attached deposits start to spall off and fall into the solution as exposure continued due to the continued stirring of the solution. Owing to the CP deposit on the alloy surface, marginal dissolution/or trenching of the matrix nearby the cathodic second phase particles were not visible. Descaling of CP deposit was performed to study the degree of attack on the sample matrix from aggressive ions after gravimetric testing. The samples were dipped in a descaling solution, as described in (**section 3.4.3**).

The SEM images of the cast A360.1 alloy after the descaling are shown in **Figure 4-10b**; SEM image analysis showed the development of micro pits and peripheral dissolution around the  $\alpha$ -Al matrix adjacent to the cathodic second phase particles. These second phase particles, such as  $\alpha$ -SiAlFeMg dendrite structure,  $\beta$ -SiAlFe IMP, and Si phase, lead to the development of micro galvanic cell in the  $\alpha$  - Al matrix leading to intragranular attacks experienced by this alloy, as shown in **Figure 4-10b**. The magnesium in a magnesium silicon IMP is anodic in the  $\alpha$  - Al matrix when exposed to an aggressive solution. It dissolves into the solution as it was not detected by EDS analysis on the surface after exposure.

In strengthening the materials, alloying elements like Cu, Mg, and Mn are added and help mitigate needle-like SiAlFe. These results create a different type of IMP, such as  $\text{Si}_2\text{Al}_{15}\text{FeMg}$ ,  $\text{Si}_7\text{Al}_4\text{Mg}_8\text{Cu}_2$  phases forming the various localized corrosion experienced by the alloy shown in **Figure 4-10c**. These IMPs have been identified to exhibit alternating corrosion behavior on the alloy matrix using some electrochemical studies.

Some of these IMP are iron-rich, which has high potential forming the cathodic sites compared with the aluminum matrix being the anodic leading to selective dissolution at the periphery between the iron-rich IMP and aluminum matrix. The corrosion sites are visible on the alloy after descaling close to the iron IMP, 3

occurring on the alloy matrix adjacent to these iron IMPs, leading to micro-pits formation, as seen in **Figure 4-10b-d**, and dealloying of these IMPs was also revealed. Similarly, Yasakau [66] reported that  $\text{Si}_7\text{Al}_4\text{Mg}_8\text{Cu}_2$  possesses a reduced corrosion potential (more negative) than the  $\alpha$  - Al matrix, and  $\text{Si}_2\text{Al}_{15}\text{FeMg}$  is cathodic compared with the  $\alpha$  -Al matrix. Also, Jain [67] reported that Fe bearing intermetallic conductivity is higher than



its silicon counterpart. Therefore, corrosion damage ought to be more severe at the  $\alpha$ -Al/Fe-containing phase than the Si/ $\alpha$  - Al interface, as seen in **Figure 4-10c**.

Shallow pits were found on the cast alloy after exposure to ASW due to the continuous corrosion of the alloy matrix around the vicinity of intermetallic particles. On continuous exposure, the particles detach, leaving a cavity. As new pits start at the periphery of re-passivated pits, older and shallow pits will, in general, combine and become broader and wider, as seen in **Figure 4-10d**. Some extreme pit/pores were observed on the alloy surface, and it is viewed that pitting was steady at the base, where the ceaseless disintegration of base aluminum is sustained. This could be because of localized anoxic conditions present under built-up corrosion products. **Figure 4-10d** shows the copper intermetallic presence in small amounts scattered in the alloy matrix and negatively affects the alloy surface.

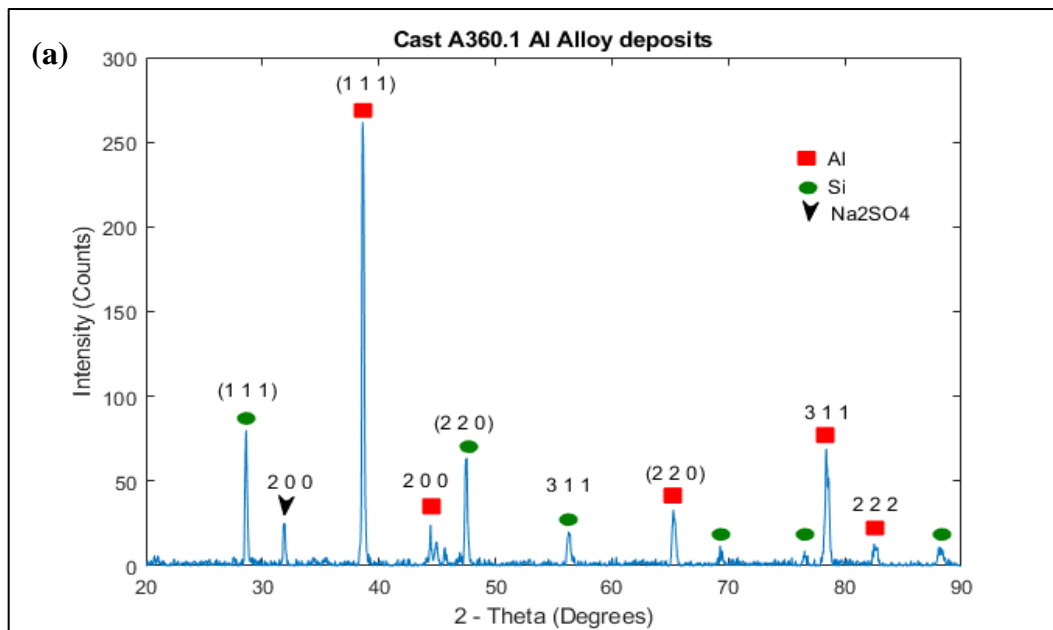
#### **4.3.1 Surface Analyses of Non-Irradiated cast A360.1 After Exposure Using XRD And Raman Spectroscopy.**

**Figure 4-11a** displays the XRD spectra of cast A360.1 after exposure to ASW in the absence of  $\gamma$ - radiation. The dominant phase in this XRD data presented below is  $\alpha$ -Al, whose intensity is slightly affected due to a few patches of oxide deposit on the alloy surface.

The next primary phase in the Al-Si-Mg alloy is the Si eutectic phase, possessing a smaller grain size and more random orientation, whose intensity was also affected by an oxide deposit. A single peak belonging to the sulfate group could be identified on the XRD results, which may be due to the adsorption of sulfate ions from the ASW solution on cast

alloy. The cast A360.1 contains several pores and intermetallics, which were revealed due to trenching effects in the alloy microstructure when they react with seawater solution, as shown in **Figure 4-10a**. However, no peak corresponding to intermetallics could be identified by XRD analysis. Therefore, aside from the peak intensities, no significant changes took place on the cast alloy used for this study after ten days of exposure in seawater due to the corrosion product deposits' low volume fractions.

Similarly, the Raman spectrum of the cast A360.1 is represented in **Figure 4-11b**. The silicon peak position at  $520\text{ cm}^{-1}$  remains the same with a slight shift of  $1 - 2\text{ cm}^{-1}$ , but there is a difference in intensities compared with **Figure 4-6**. All other peaks in the spectrum are single phases without any interference from intermetallic particles. The peaks of  $1107\text{ cm}^{-1}$  can be attributed to the sulfate stretching groups. The ASW solution contains sulfate ions, which adsorb on the aluminum surface [68]; this feature was identified by XRD results above. The dominant Raman peaks at  $1219$  and  $1592\text{ cm}^{-1}$  are assigned to the graphitic carbon [59].



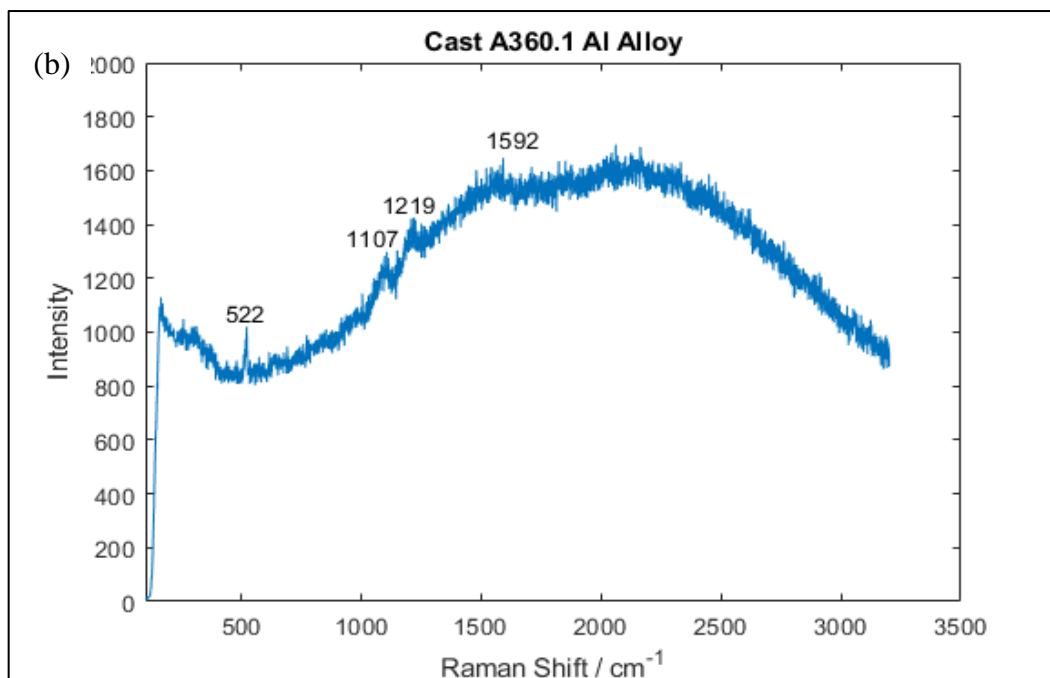


**Figure 4-11: Surface analyses (a) XRD pattern of non-irradiated cast A360.1 (b) Raman spectrum of the corrosion product deposit of non-irradiated cast A360.1.**

#### **4.4 Corrosion Behaviour of Irradiated cast A360.1 Exposed in Artificial Seawater Solution.**

The interaction of gamma radiation with seawater followed a similar pattern for radiation chemistry of pure water and described in the previous sections. However, the presence of aggressive ions such as  $\text{Cl}^-$  tends to interfere with some of the species formed, leading to the formation of various radiolytic species. These radiolytic species produced under such conditions include  $\text{H}$ ,  $\text{OH}$ ,  $\text{e}_{\text{aq}}^-$ ,  $\text{ClO}^-$ ,  $\text{OH}^-$ ,  $\text{H}_2$ ,  $\text{H}_2\text{O}_2$ , and  $\text{ClO}_3^-$ . Some of these species further recombine on interactions with each other to form water. Some species are found to be dominant such as  $\text{H}_2$  and  $\text{H}_2\text{O}_2$  developing to a steady-state concentration [36].

The corrosion behavior of the cast A360.1 aluminum alloy in the presence of radiation is dependent on the amount of radiolytic species produced by irradiation of the ASW

solution. The presence of an oxidizing agent in seawater is increased with irradiation; consequently, the oxide deposit thickness on the cast alloy surface is increased [69]; at this stage, the transport of small ions through the oxide film became the only necessary process [70]. The density of corrosion products increases on continuous exposure in the presence of radiation, as shown in **Figure 4-12a** below.

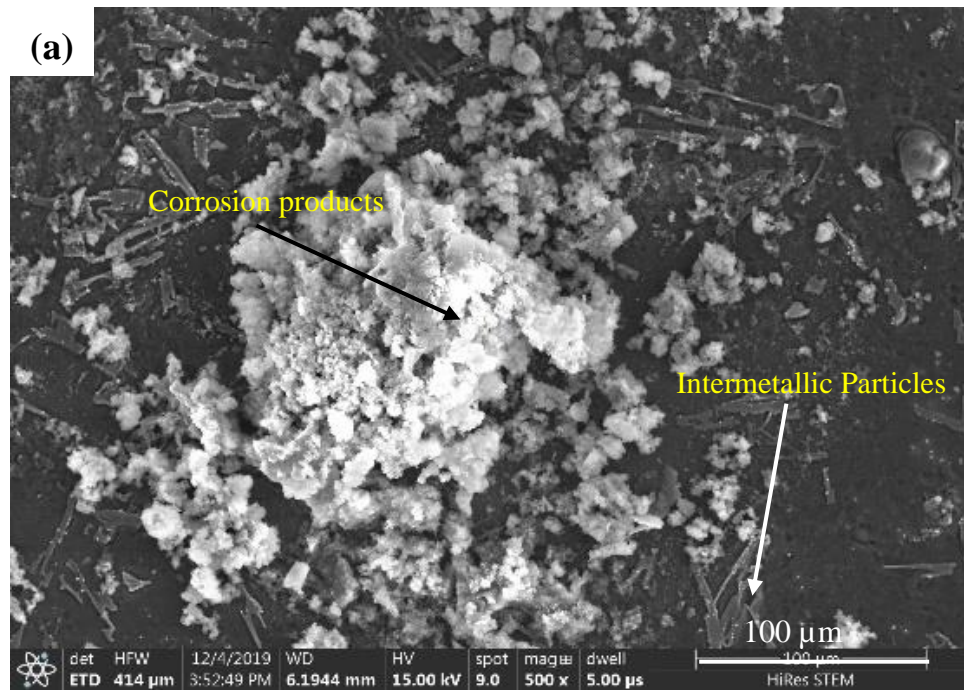
The SEM images show that massive corrosion product (CP) deposits cover a significant fraction of the sample's surface. The underlying microstructure of the alloy could not be seen to determine the interaction of increased radiolytic products with the alloy due to the thick CP deposit. The irradiated samples were descaled to investigate the underlying layer using the method described in section 3.4.3 above. After eliminating corrosion products, SEM images indicate the extent of localized corrosion, such as pitting corrosion and intragranular attack on cast A360.1 aluminum alloy.

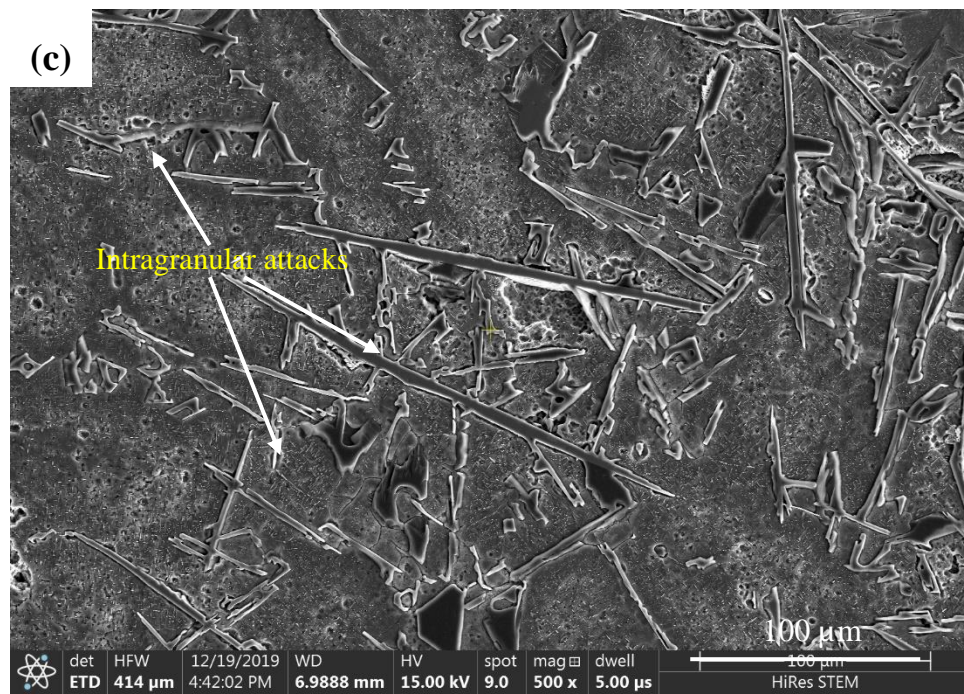
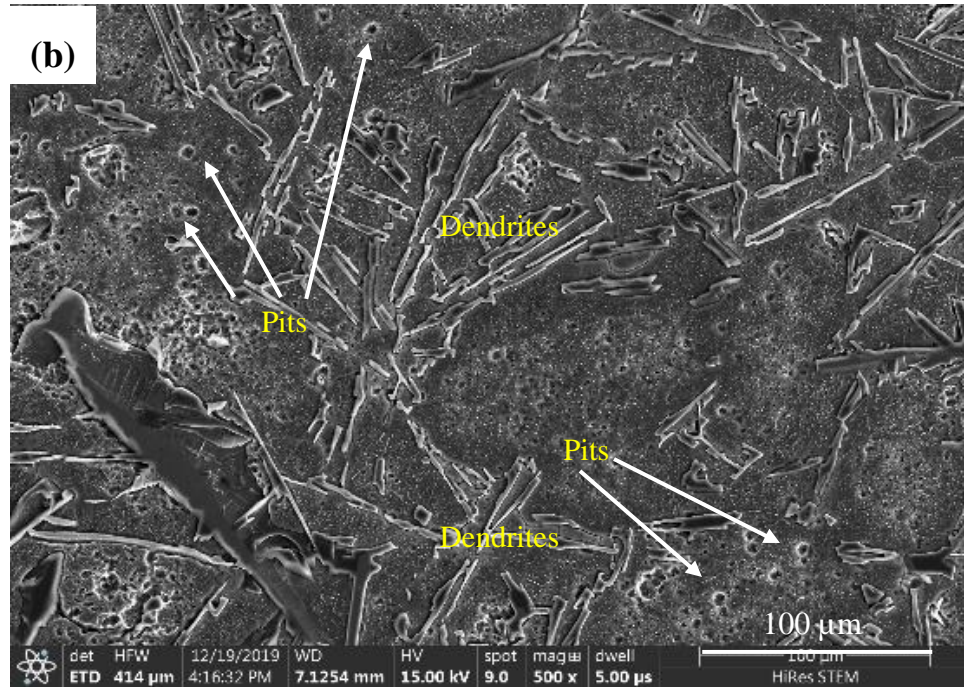
Pitting corrosion is considered as an autocatalytic process with the cathodic separation of water and the effusion of gaseous hydrogen, and anodic oxidation of aluminum. Pitting corrosion was accelerated due to radiolytic products, which was evident after the removal of CP. The CP formed on the alloy surface covered the tiny pits formed on the alloy surface, but after the removal of these corrosion products, the pits on the alloy surface became visible. Previous researchers have noted that pitting could be found beneath the CP deposits and can only be seen after descaling [71]. As shown in **Figure 4-12b**, increased pitting was noticed after removing the oxide deposit, which could be attributed to increased anoxic conditions formed under the oxide deposits.

The increased vulnerability of the cast A360.1 to pitting corrosion in the presence of gamma radiation is related to the presence of a high concentration of IMPs such as Mg.

Mg is known to exhibit continuous intragranular beta-phase ( $Al_8Mg_5$ ) precipitation along the grains, which are anodic to the aluminum-silicon-magnesium matrix leading to localized attacks such as pitting [61].

Preferential dissolution of cast A360.1 along the grain boundaries of IMP, as shown in **Figure 4-12c**, occurred because of the contributions of increased redox species made available by irradiation. The presence of a corrosive environment (seawater) and radiolytic effects on seawater increased redox species formation, further accelerating the intragranular attacks on the alloy surface, as seen after descaling. These intragranular attacks could not be seen without descaling because of the massive CP deposits on the alloy surface.





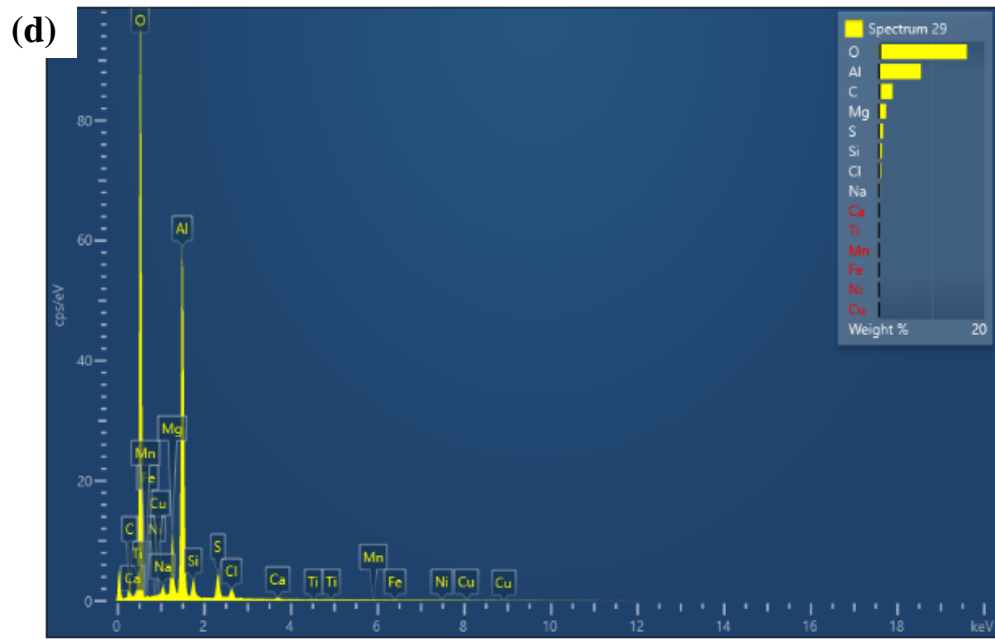


**Figure 4-12: SEM images of cast A360.1 exposed in the presence of radiation. (a) corrosion product deposit (b) result of descaled (a), (c) high magnification of intermetallic particles, (d) EDS results of cast A360.1 alloy.**

EDS analysis was carried out at specific areas on irradiated samples' surface, and the results indicate O, Al, C, Mg, S, Si, and  $\text{Cl}^-$  peaks. A representative EDS spectrum is shown in **Figure 4-12d**. EDS showed a high oxygen peak resulting from the high oxide deposit occurring due to redox species' presence in the solution. The segregation around the IMP could be attributed to the interaction of redox species with  $\text{Cl}^-$ . Also, an attack around the Si particles was noticed, new shallow pits were noticed around the  $\alpha$ -Al/Fe-rich interface.

#### **4.4.1 Surface Analyses of Irradiated cast A360.1 After Exposure Using XRD And Raman Spectroscopy.**

Further surface characterization was done using XRD and Raman spectroscopy. The diffraction peaks shown in **Figure 4-13a** belong to Al, Si, and  $\text{Na}_2\text{SO}_4$  as no  $\text{Mg}_2\text{Si}$  peaks

were identified in the sample. The presence of  $\text{Na}_2\text{SO}_4$  on the sample's surface can be attributed to salt deposit after exposure to the seawater solution used for this analysis. The intensity of other peaks decreased significantly after exposure to irradiated seawater due to an increased corrosion product deposit on the surface of the sample. Peaks of Al and Si were identified in different sections of the samples showing the distribution of both phases present in the sample. The peak intensity and broadening of the Al (111) and Si (111) appeared to be different, which can be ascribed to location effects. The peaks of Al appeared to be broader than the peaks of Si.

**Figure 4-13b** shows the Raman spectrum of the corrosion product deposit of irradiated cast A360.1 alloy after exposure to the ASW solution. The Raman spectrum showed a primary Raman shift at  $521/522\text{ cm}^{-1}$  (the prominent silicon peak is  $520\text{ cm}^{-1}$ ), which can be attributed to silicon or silicon dioxide films on the aluminum surface. The increase without a well-defined peak in the range of  $520 - 522\text{ cm}^{-1}$  could be associated with Si/SiO<sub>2</sub>. Silicon oxide shares the same peak position as silicon. As a result of oxide formation on the alloy surface, silicon oxides could be formed by interaction with oxygen present in the seawater solution [72]–[75]. **Figure 4-13b** shows that the Raman shift that appeared at  $960.1\text{ cm}^{-1}$  could be assigned to sulfate groups present in seawater solution containing sulfate ions [68].



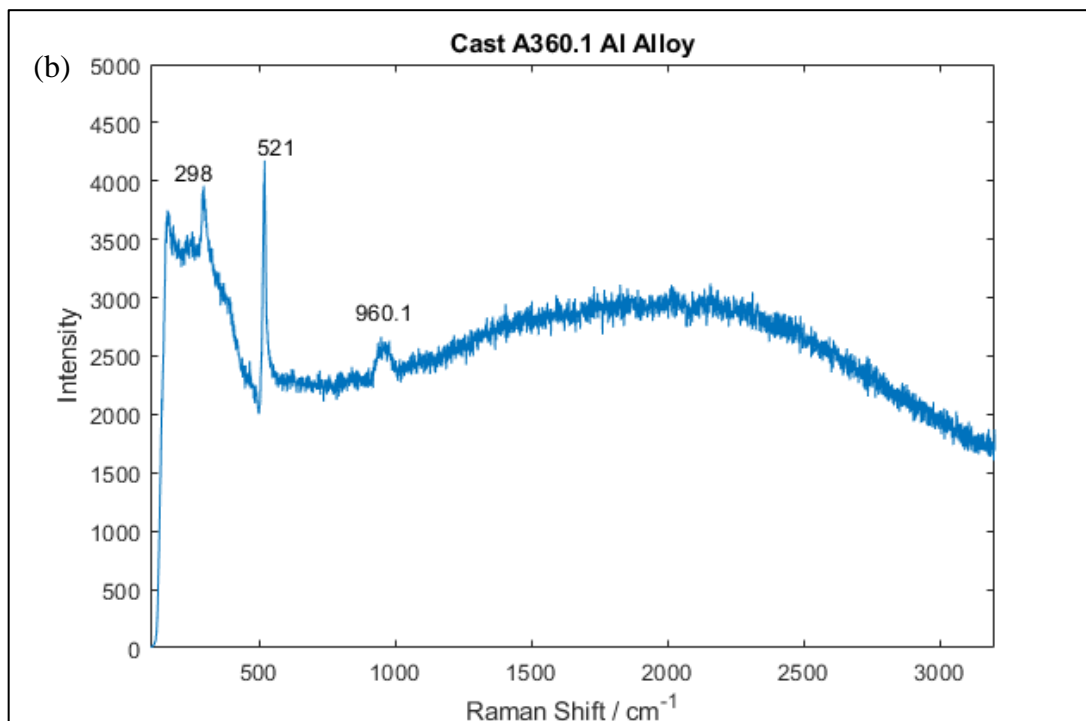
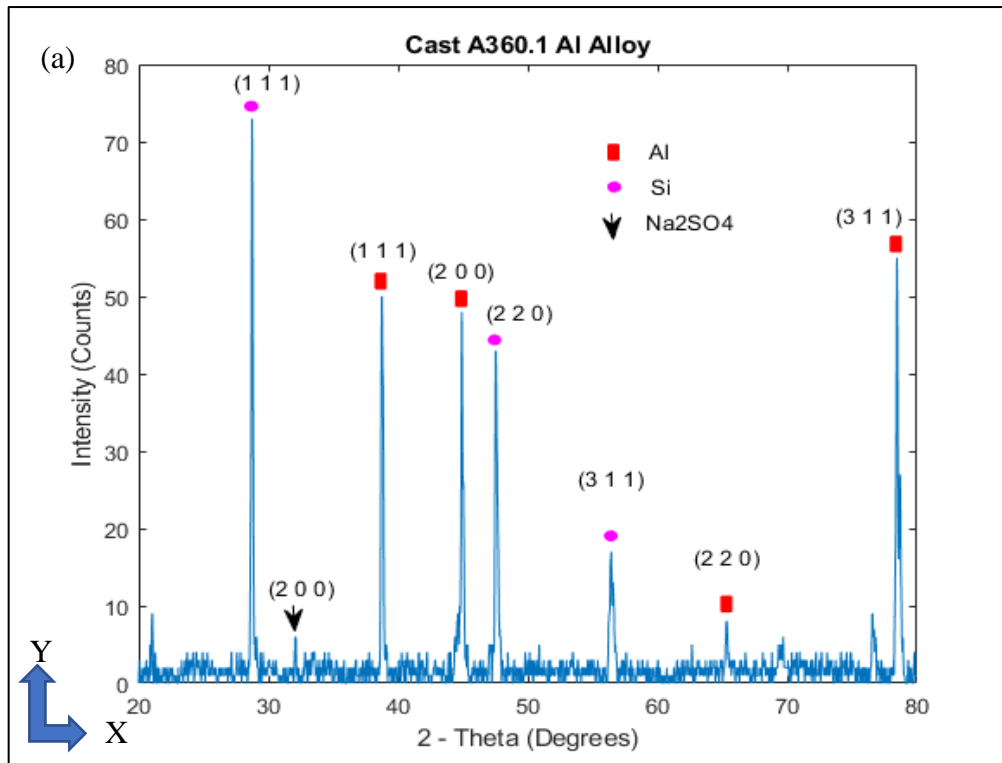
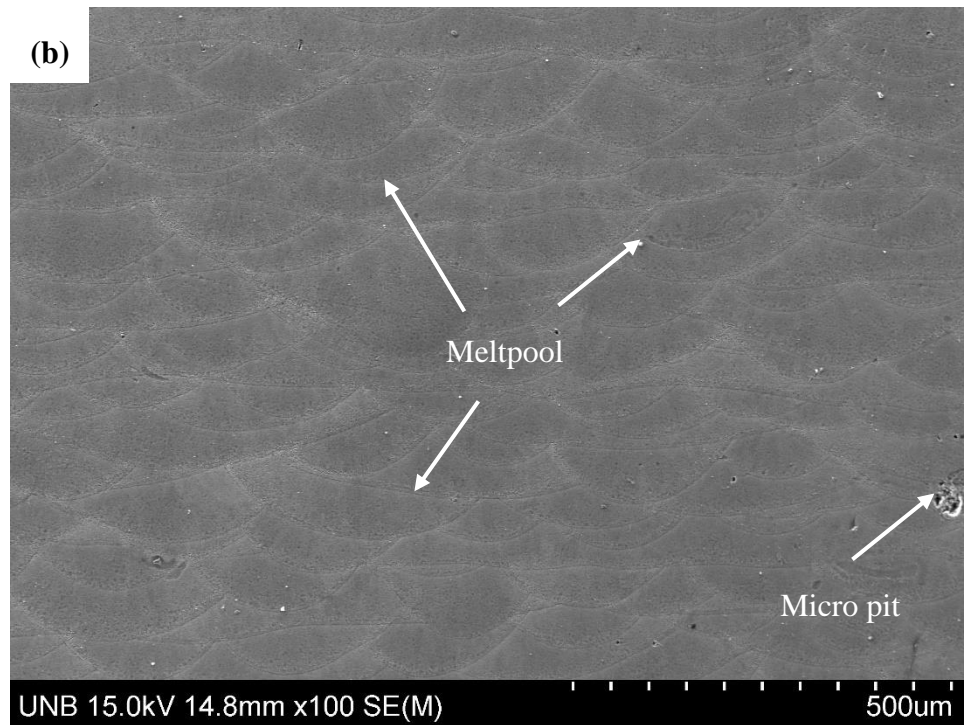
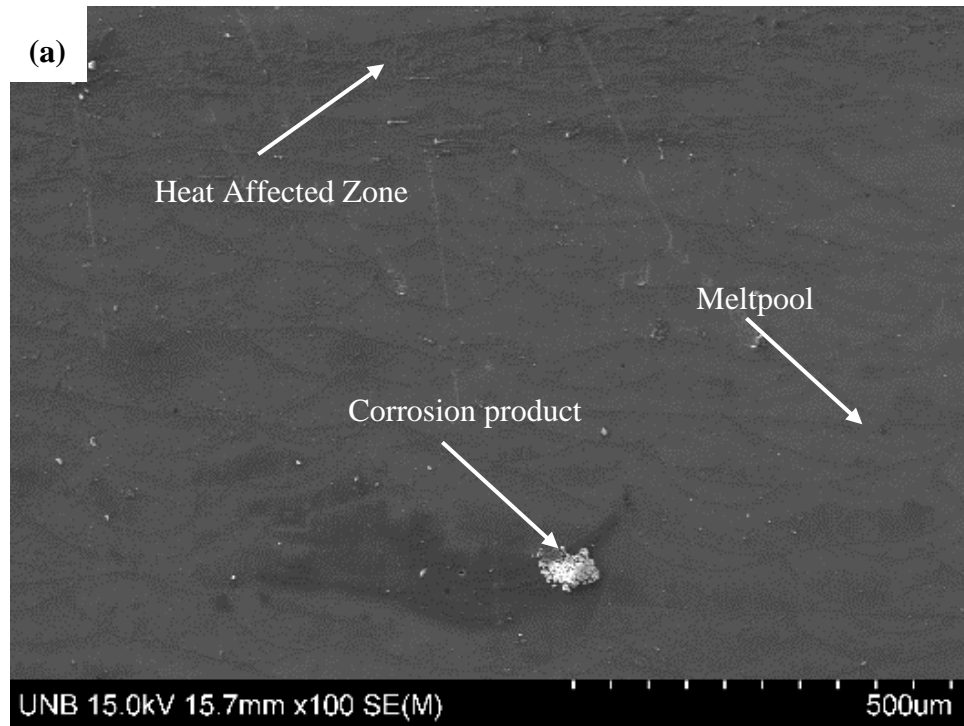


**Figure 4-13: Surface analyses (a) XRD pattern of irradiated cast A360.1 (b) Raman spectrum of the corrosion product deposit of irradiated cast A360.1.**

#### **4.5 Corrosion Behaviour of LPBF AlSi10Mg After Exposure in the Absence of $\gamma$ -Radiation.**

The surface morphology and chemical composition of the polished surface of LPBF alloys were investigated after exposure to the ASW solution in the absence of  $\gamma$ -radiation for 240 hours using SEM; the results are presented in **Figure 4-14** below. Immersion of samples to ASW showed the formation of a thin layer of corrosion products, as shown in **Figure 4-14a**, where similar selective corrosion attacks occurred all over the sample's surfaces. As the melt pools become visible, selective corrosion could be seen along the laser tracks and prone to corrosion attacks. Si-network is widely distributed on the microstructure of LPBF-AlSi10Mg and contains various zones such as coarse zone and heat-affected zones. The coarsening and splitting of these zones account for its behavior on exposure to an aggressive solution [1], [76].

A careful observation of the sample's surface at different exposure times shows an increased corrosion attack as exposure time increases. The result from SEM revealed localized forms of corrosion typical of Al alloys distributed on the surface of the melt pools. In contrast, the hidden melt pools are revealed, appearing as a semicircle shape. The samples were descaled utilizing the technique described in section 3.4.3 to determine the rate of an aggressive attack on the alloy surface. No significant pitting effect was observed on the sample's surface and around the melt pool boundaries. Little pores on the alloy surface after descaling resulted from manufacturing defects, but they can be sites for localized corrosion such as pitting corrosion.



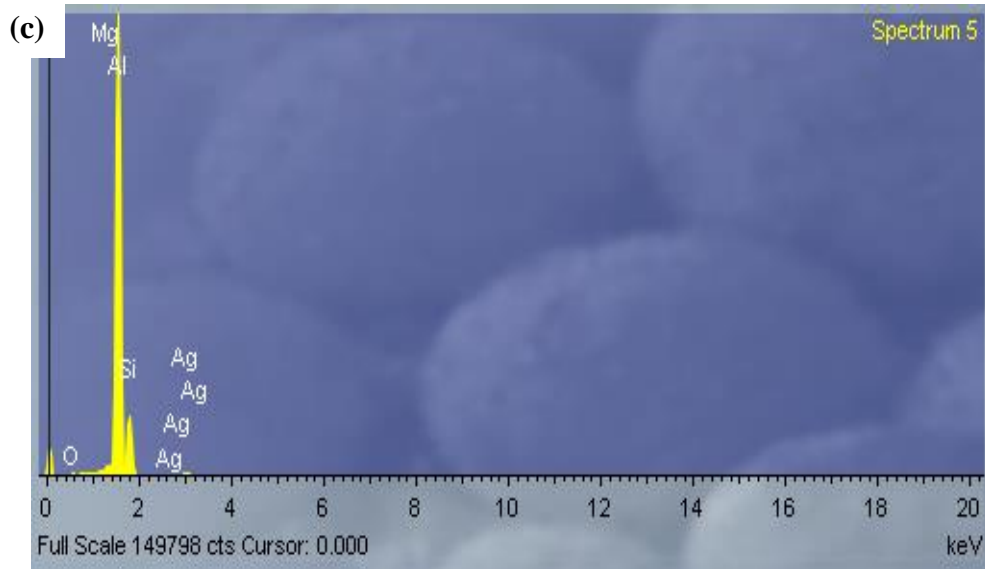


**Figure 4-14: SEM images of LPBF AlSi10Mg exposed in the absence of  $\gamma$ -radiation. (a) corrosion product deposit (b) result of descaled (a), (c) EDS results of LPBF AlSi10Mg alloy.**

The microstructure of LPBF AlSi10Mg described in section 4.1.2 is very fine and not the same as that of the cast alloys. The microstructure of the as polished LPBF samples was plain and featureless before exposure. However, after exposure, the surface revealed the matrix of  $\alpha$ -Al and interdendritic Si particles. The result of descaled samples revealed solidified meltpools as semicircular shapes reflecting the gaussian shape of laser beam power dispersion. The meltpools overlapped each other showing a total dissolution of the current layer combining with un-melted layer lines, thereby appearing as a continuous line, as shown in **Figure 4-14b**.

The  $\alpha$ -Al phase solidifies with different sizes in the melt pool, and due to the rapid hardening, the  $\alpha$ -Al phase remains supersaturated. This solidifying effect prevents the formation of Fe-rich and other IMPs. When formed, the dimensions are too small to influence the corrosion behavior of LPBF samples, thereby limiting the cathodic effects these IMPs have on the alloy. There was no trenching between the IMP interfaces and  $\alpha$ -

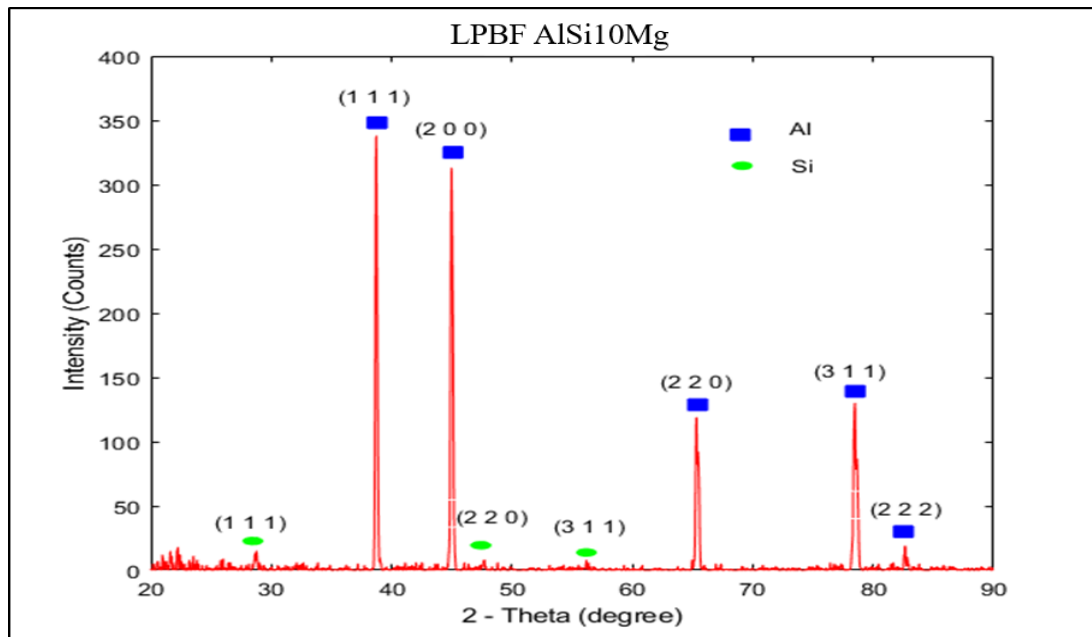
Al, increasing the corrosion resistance of the alloy when exposed to seawater solution. EDS analysis in **Figure 4-14c** shows peaks for Al, Si, and Mg prevalent in all the EDS spectra obtained for this sample. The results confirm that the cells resulting from the etching effect of aggressive ions in seawater are mainly made of the  $\alpha$ -Al and Si. At the same time, Si is preferentially precipitated around the cell limits and alloy surfaces. Another alloying element like magnesium is uniformly distributed in the alloy surface as compared to the Si. The less detrimental effect of this element on the alloy microstructure is because of its uniform distribution, high solidification, and minimum solute concentration [77].

#### **4.5.1 Surface Analyses of Non-Irradiated LPBF AlSi10Mg After Exposure Using XRD And Raman Spectroscopy.**

XRD analysis was carried out to determine the different phases inherent in the sample. The XRD patterns acquired from the exposed samples to the seawater solution is presented in **Figure 4-15**. The XRD patterns are identical to those obtained before exposure. In both cases, peak (111) corresponding to Al demonstrated the most intensity, followed by the Al (200) peak. The two other aluminum peaks, Al (220) and Al (311) are of lower intensity because of film development on the alloy surface after exposure to seawater. Comparing before and after exposure results, the pattern shows Si peaks decreased further because of the coarsening of the Si phase. However, further study is required to comprehend the crystal plane growth of this alloy fully.

Raman spectrum analysis was carried out to examine components of the passive film **Figure 4-15b** shows the Raman spectrum of the LPBF AlSi10Mg after exposure to ASW. The vibrational styles of aluminum species are reported in the literature [78], [79]. The

Raman spectrum of LPBF alloy after exposure show the presence of several Raman shifts at  $163.2\text{ cm}^{-1}$ ,  $291.7\text{ cm}^{-1}$ ,  $469.2\text{ cm}^{-1}$ ,  $515.7\text{ cm}^{-1}$ ,  $981.7\text{ cm}^{-1}$ , and  $2331\text{ cm}^{-1}$ . The new peak at  $291.7\text{ cm}^{-1}$  can be attributed to an aluminum chloride complex [80]. The chloride ions present in the seawater could be attached to the alloy matrix. The peak at  $515.7\text{ cm}^{-1}$  could be attributed to silicon in the Al alloy matrix, as silicon peaks have been identified at  $520\text{ cm}^{-1}$ . The peak shift at  $515.7\text{ cm}^{-1}$  might be because of the amorphous nature of the oxide deposits on the alloy surface, shifting the peaks to a new position [74]. The band at  $981.7\text{ cm}^{-1}$  stems from the presence of sulfate salts present in the seawater [68], while peak  $2330\text{ cm}^{-1}$  remains unidentified.



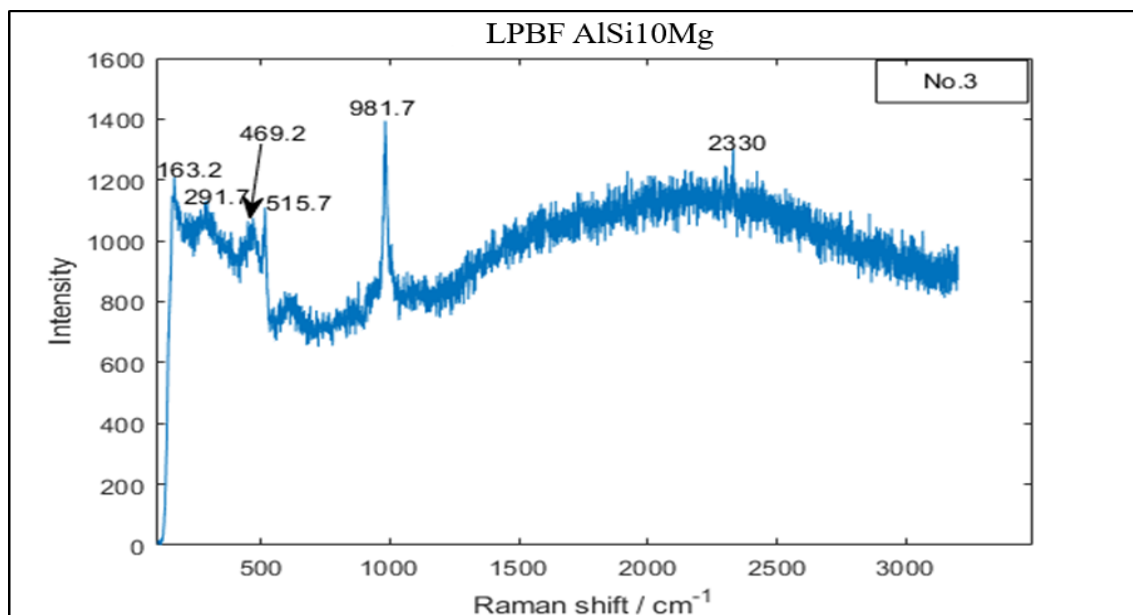


**Figure 4-15: Surface analyses (a) XRD of non-irradiated LPBF AlSi10Mg (b) Raman Spectrum of non-irradiated LPBF AlSi10Mg.**

#### **4.6 Corrosion Behaviour of LPBF AlSi10Mg After Exposure in the Presence of $\gamma$ -Radiation.**

The LPBF AlSi10Mg samples were exposed to low-dose gamma radiation to investigate how water radiolysis products from irradiation impact the sample's corrosion rate. The oxide film seen on the sample's surface is dependent on the composition of the material, distribution, and presence of macro defects (size and shape of IMP), and micro defects (pores and vacancies) and crystal structure, which are important factors controlling the rate of corrosion of the sample.

As described in section 4.2.2, radiation increases the weight loss of the LPBF sample. The increased weight loss is attributed to the presence of radiolytic products interacting with chloride ions found in the solution, thereby increasing the surface attacks compared with

the unirradiated plots. This interaction between water radiolysis products and aggressive ions results in the increased etching effects experienced by the aluminum alloys used for this study. The melt pools became visible in **Figure 4-16a** compared with unirradiated exposure. However, more oxide film patches could be seen on the sample, and a thin dark grayish film could be seen covering the sample and the semicircular melt pools. The films forming on the sample are less protective than the typical passive films forming on the aluminum alloys. Intensive localized corrosion attack such as pitting was not visibly present, but increased corrosion product deposits resulting from radiolytic species were evident.

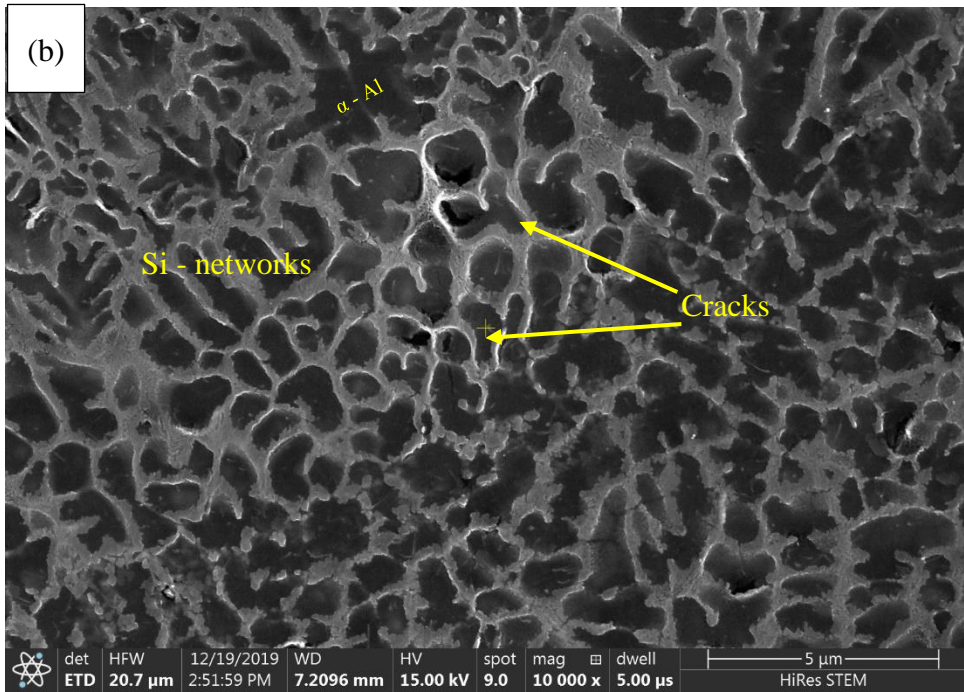
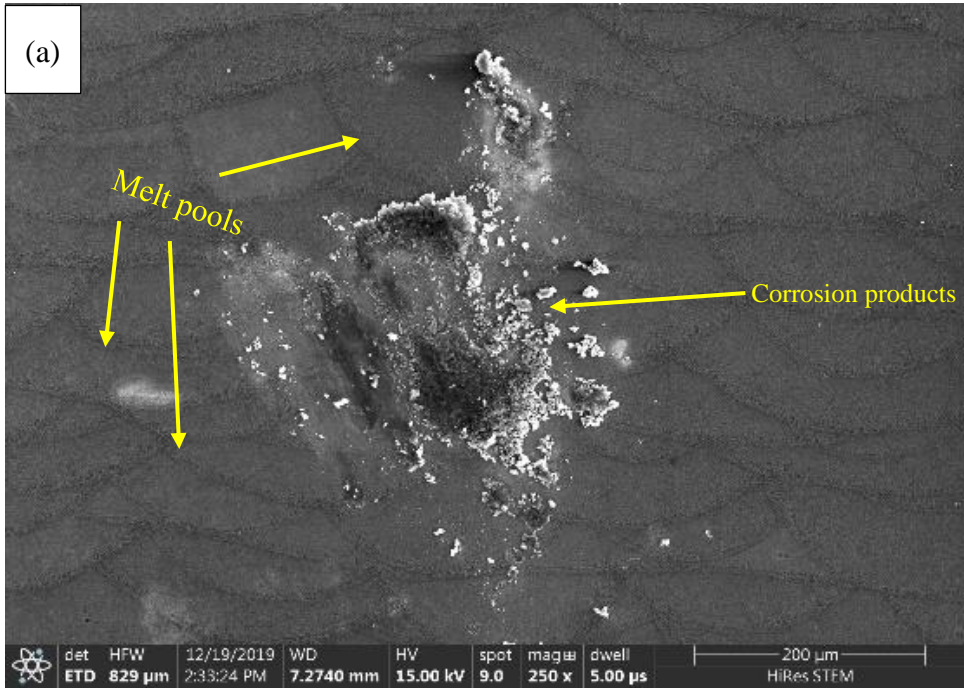
As described in section 4.1.2, the silicon crystal is widely distributed on the matrix of  $\alpha$ -Al cellular grains. Therefore, increasing radiolytic products coupled with aggressive ions exacerbates corrosive attack at the cells with an enriched Si phase. The coarsening and breaking of the Si network were detected, as shown in **Figure 4-16b**.

The increased coarsening of the Si phase can be ascribed to the nature of the nobility of Si comparative with the matrix of  $\alpha$ -Al resulting in trenching or breaking of the Si network along the coarse and heat-affected zones. The micro-galvanic corrosion occurs around the single Si shell regions, forming a small, compact white film on the Si network, as seen in **Figure 4-16b**, to protect the  $\alpha$ -Al matrix from corrosion.

Therefore, in the presence of radiation, the LPBF alloy exhibited a better corrosion resistance than its cast counterpart, which can be ascribed to the surface's coverage with Si network possessing a coarse dendritic structure. This hinders the quick dissolution of the metal matrix by the electrolyte, thereby making the transfer of  $\text{Al}^{3+}$  dissolving into the



electrolyte difficult. The thicker oxide deposit observed in its cast counterpart in the presence of radiation was absent in the LPBF alloys due to silicon.



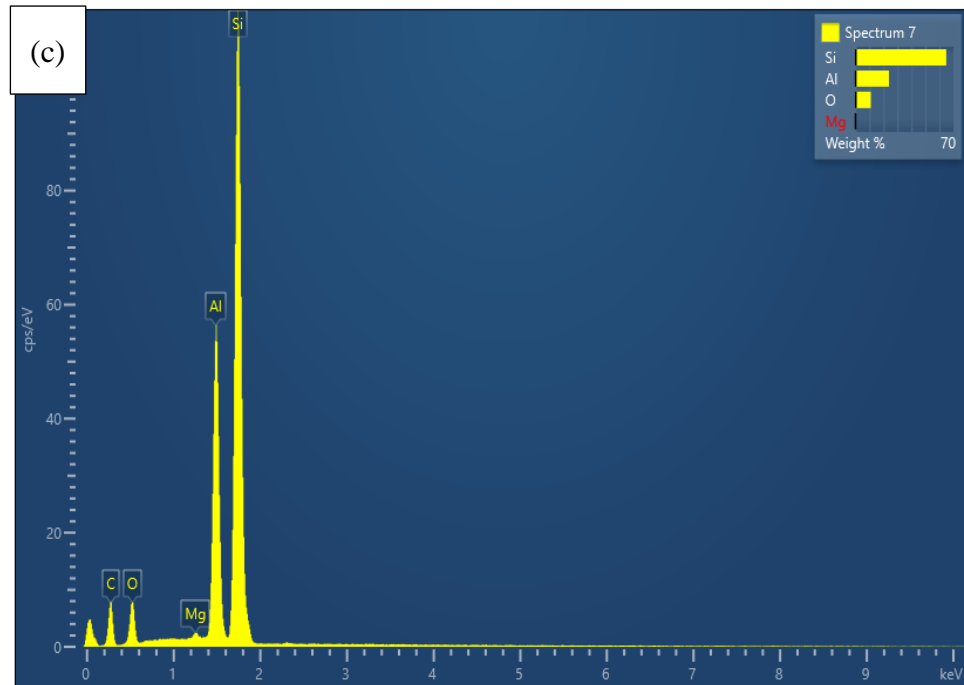


**Figure 4-16: SEM images of LPBF AlSi10Mg after exposure in the presence of  $\gamma$ -radiation. (a) corrosion product deposit (b) Si network decorating the Al matrix clearly visible after exposure (c) EDS results of the alloy after exposure.**

The two samples used in this study (cast A360.1 and LPBF AlSi10Mg) were manufactured using different processes but had very close chemical composition; the eutectic silicon particles assume various roles in corrosion reaction. Microscale eutectic particles of silicon are widely seen on the alloy surface, leading to the coupling on the alloy matrix, such as galvanic coupling. The oxide film on the alloy surface could be disordered because of the grain size of the eutectic silicon forming a free and permeable oxide layer on the alloy surface [53].

The weak oxide layer can provide an opportunity for the interaction of aggressive ions with the aluminum matrix, causing corrosion cracks on the Si network, as seen in **Figure 4-16b**. However, slight corrosion cracks around the aluminum matrix and the

silicon network were noticed on this alloy with no severe cracks. This behavior appeared strange because of the combined interaction of radiolytic products and aggressive ions in the solution forming oxidized chlorine; however, the dose rate is low. Therefore, no drastic impact of radiation is experienced on this alloy after exposure.

The EDS results shown in **Figure 4-16c** above confirmed the presence of Si peaks representing the silicon network covering the aluminum matrix, and oxygen peaks depicting the oxides formed on the silicon networks could also be seen. EDS maps [1] confirmed the preferential precipitation of Si phases on the aluminum matrix; Rosenthal et al. [57] identified the decoration of the aluminum matrix with the Si phase network. The silicon network protects the aluminum matrix from attacks by the reactions of radiolytic products with aggressive ions, accounting for the improved corrosion resistance of this alloy.

#### **4.6.1 Surface Analyses of Irradiated LPBF AlSi10Mg After Exposure Using XRD And Raman Spectroscopy.**

XRD spectrum of the irradiated LPBF AlSi10Mg immersed in ASW for 240 hours is presented in **Figure 4-17a**. The typical peaks for Al were seen at  $38.42^\circ$ ,  $44.66^\circ$ ,  $65.05^\circ$  with a reduced intensity as compared with XRD results before exposure. The aluminum peak originates from the underlying matrix or the partially oxidized layer not yet covered by oxide. Silicon peaks were also identified at  $28.40^\circ$ ,  $47.28^\circ$ ,  $56.07^\circ$  with low intensity. The reduced intensity could be attributed to the oxide film formed around the silicon network. There was no significant contrast between the XRD result of the irradiated and the non-irradiated samples aside from the difference in the peak intensities. The intensity

of irradiated peaks was higher than that of the unirradiated peaks due to increased etching effects on the substrate revealing the silicon networks and  $\alpha$ -aluminum matrix.

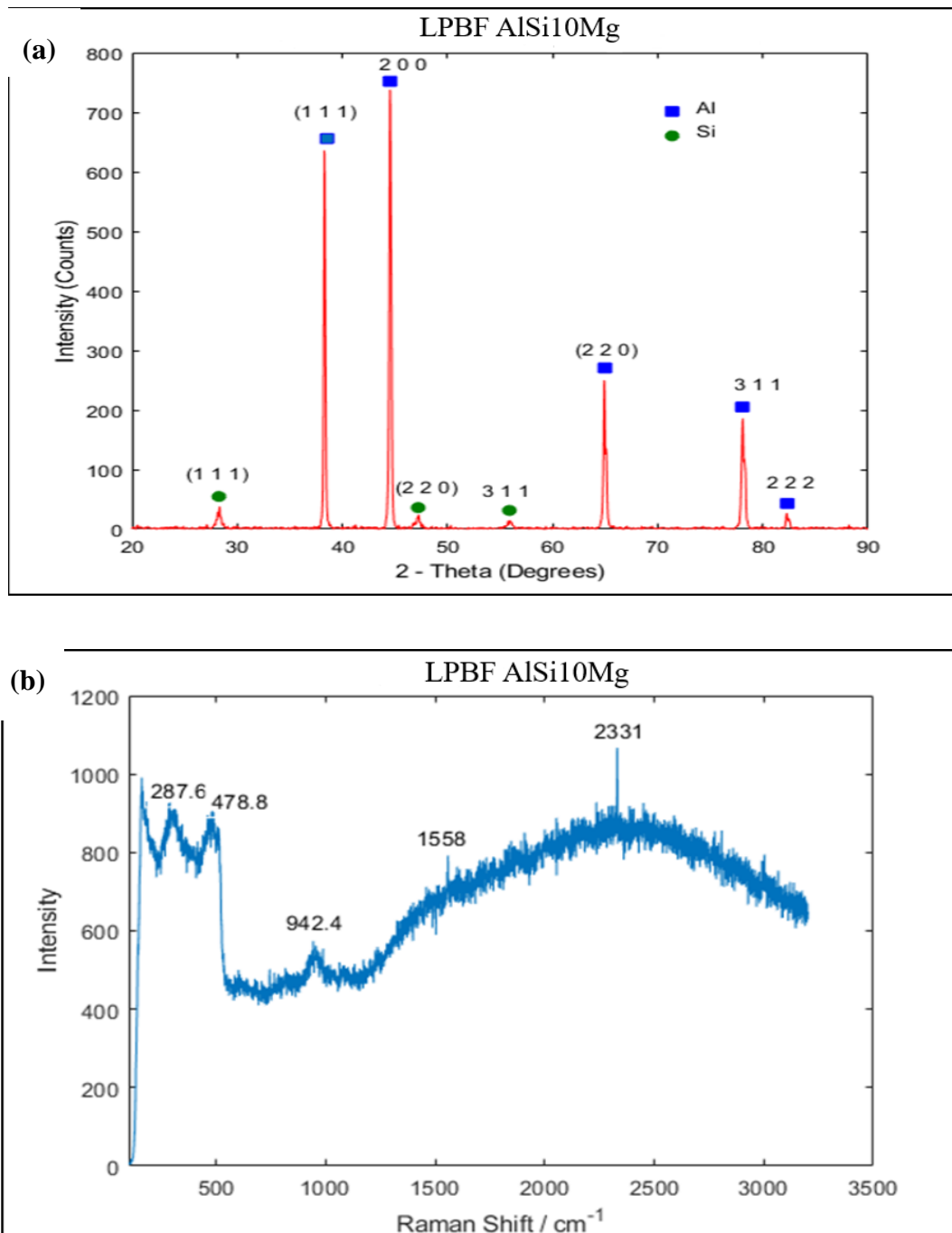


**Figure 4-17: Surface analyses (a) XRD of irradiated LPBF AlSi10Mg (b) Raman Spectrum of irradiated LPBF AlSi10Mg.**

**Figure 4-17b** shows the Raman spectrum of the irradiated LPBF alloys, deployed to identify the phase and chemical composition of oxides forming on the surface of the sample. In comparing the irradiated Raman spectra with the nonirradiated, the results displayed that similar peaks appeared in each exposure with some peak shifts in both spectra. The peak shifts and differences in the peak intensities of both exposures could be ascribed to the amorphous nature of the oxides or corrosion products depositing on the alloy surface. Various Raman shifts can be seen on the spectra above. Thomas et al. [81] assigned  $400 - 506 \text{ cm}^{-1}$  to isolated  $\text{AlO}_6$ , which shows the disparity in Al – O bond lengths;  $520 \text{ cm}^{-1}$  peaks have been assigned to the silicon group. The reduced intensity could be ascribed to corrosion products' deposition on the silicon network forming silicon oxide as they both share the same peak position [72]–[75].

The other peaks, such as  $942.4 \text{ cm}^{-1}$ , are attributed to sulfate groups, resulting from sulfate ions in seawater solution [68], while peak  $1558 \text{ cm}^{-1}$  is assigned to graphitic carbon. The graphitic carbon can result from the polishing dirt on the aluminum substrate [59], while peak  $2331 \text{ cm}^{-1}$  remains unidentified.

#### 4.7 Changes in pH During Corrosion of Aluminum Alloy at Room Temperature

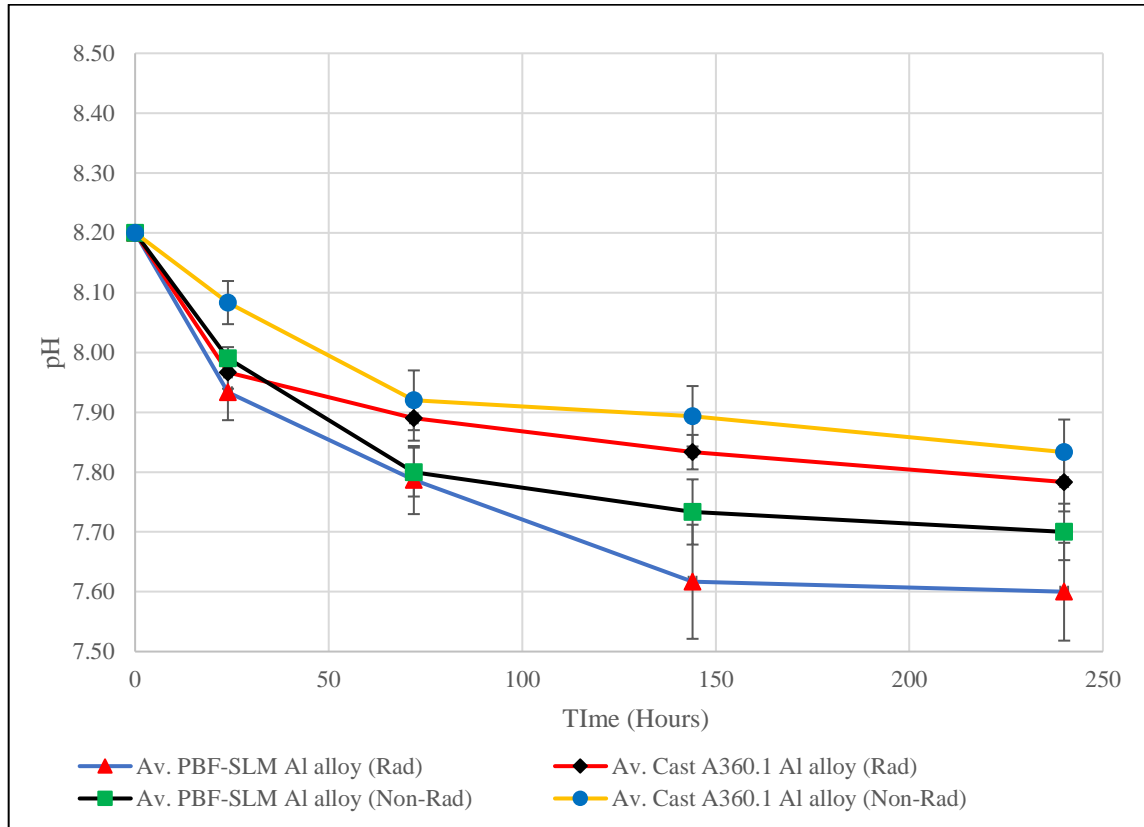


**Figure 4-18: The pH of seawater solution in the absence and presence of irradiation as a function of immersion time.**

Changes in pH against time curves are shown in **Figure 4-18**. Points shown on the plot represent an average of three experimental runs with their standard error bars showing the deviations. As widely reported in the literature, aluminum has the potential of forming oxides when exposed to the environment [62]. The resistance of aluminum to corrosion depends on the oxide film on the alloy controlled by the environment's pH.

The influence pH has on metals can be represented in a Pourbaix diagram, as shown in **Figure 2-6**. It shows aluminum forming a passive film at a pH range of roughly between 4 – 9, whereby the metal is covered with oxide deposits. The nature/behavior of oxide is

multifaceted and dependent on the alloying materials and the corrosion media, hence determining the corrosion behavior of aluminum in that environment [25].

The general E-pH diagram used for Al, as shown in **Figure 2-6**, does not represent the general behavior of aluminum when exposed to other corrosion media such as seawater. Seawater contains a lot of chloride ions and other constituents, which causes oxide defects on the alloy. Pitting corrosion, which is the most common form of localized corrosion in aluminum alloys, is not considered in this E-pH diagram [26]. Artificial seawater with a starting pH of 8.20 used for this experimental study showed a slow, steady decline in the pH of the corrosion media to an average final pH of 7.60. The decrease in pH in the absence of radiation, though at a slow rate, could be attributed to seawater interaction with carbon dioxide widely available in the atmosphere. This decrease in pH was confirmed with a trial test for several hours, where the ASW solution without any aluminum alloy immersed in it was exposed to the environment and sampled. The pH was obtained at different exposure hours, at 8 hours increasing intervals for seven (7) days, as shown in **Figure 4-19**.

The dissolution of carbon dioxide in seawater leads to the production of aqueous carbon dioxide; further reaction with seawater leads to the formation of carbonic acid ( $\text{H}_2\text{CO}_3$ ) in equation (4-1). An increased reaction leads to the production of bicarbonates ( $\text{HCO}_3^-$ ) and hydrogen ion by splitting carbonic acid, as shown in equation (4-2).

Bicarbonates are produced as a result of the disintegration of carbonic acid. It splits to form carbonate ions ( $\text{CO}_3^{2-}$ ) and hydrogen ion in equation (4-3). Seawater has a high tendency to buffer changes in pH, the concentration of carbonates formed is not too high, and hydrogen ions produced are small, hence the slight change in the pH from a start of

8.20 to an average of 7.60. Protons ( $H^+$ ) formed as a result of these reactions are known to lower the pH of the solution as it becomes acidic [82], [83], but in this case, the acid content is small as slight pH changes were noticed.



The pH changes as a result of the dissolution of carbon dioxide in seawater fall within the passive pH range of aluminum alloys (4 – 9), justifying the increased deposit of insoluble precipitates on the cast (A360.1) alloy as the carbonates formed by equation (4-3) combines with some of the cations present in seawater, such as (calcium, potassium, magnesium, etc.). The Raman spectra and XRD peaks above have identified salt deposit on the cast A360.1, which could be attributed to the combination of seawater constituents with by-products of  $CO_2$  interactions accounting for the presence of these compounds.

On the contrary, the LPBF AlSi10Mg exhibited a different behavior under this experimental condition, as the thick, insoluble oxide deposit found on its cast counterpart was absent on this alloy. For an LPBF AlSi10Mg alloy, a thin dark grayish oxide was found covering the alloy, which can be attributed to the different microstructure of this alloy. Due to this low formation of the passive film, this alloy experienced various forms of localized corrosion. The weight loss experienced by this alloy can be associated with the direct interaction of aggressive ions with the metal interface. Comparing the result of the descaled LPBF alloy with its cast counterpart, both exposed in the absence of radiation,



showed that the cast alloy corroded more than the descaled LPBF alloy after 240 hours exposure. We can accurately say that the difference in the corrosion behavior of both alloys could not be attributed to changes in pH. Repeating the experiment with a buffer solution to keep the pH steady will help determine the main effect of pH changes on these alloys under this condition.

In the presence of radiation, there was no significant difference in the pH changes, which looks strange due to the increased amounts of radiolytic products readily available in the solution, though at a low rate, impacting the pH. Due to the decomposition and recombination of water radiolysis products, the impact of radiation on the pH was small, with a ~1.3% decrease for the LPBF alloy and ~0.6% for the cast alloy. The pH of the LPBF appeared to be affected with irradiation more than its cast counterpart, thereby accounting for the increased weight loss experienced by this alloy in the presence of radiation. This decline in pH with time in the presence of radiation was confirmed by exposing ASW to the radiation source without the aluminum alloys immersed in it and pH determined at various hours to monitor the decline in pH with time, as shown in **Figure 4-19**.

Studies [84] have shown that aluminum hydroxide is formed on the alloy at neutral or alkaline pH according to the Pourbaix diagram of aluminum. This finding could not be proved here because no potential was applied to this experiment, so it is difficult to depict what is happening on the alloy surface based on pH alone. Therefore, it is difficult to attribute the decrease in pH to the corrosion of Al alloys, especially in the presence of  $\gamma$ -radiation. The formation of nitric acid when unbuffered water and the air is irradiated has

the tendency to alter the pH of the solution [85]. However, the concentration of nitric acid was not measured in this analysis.

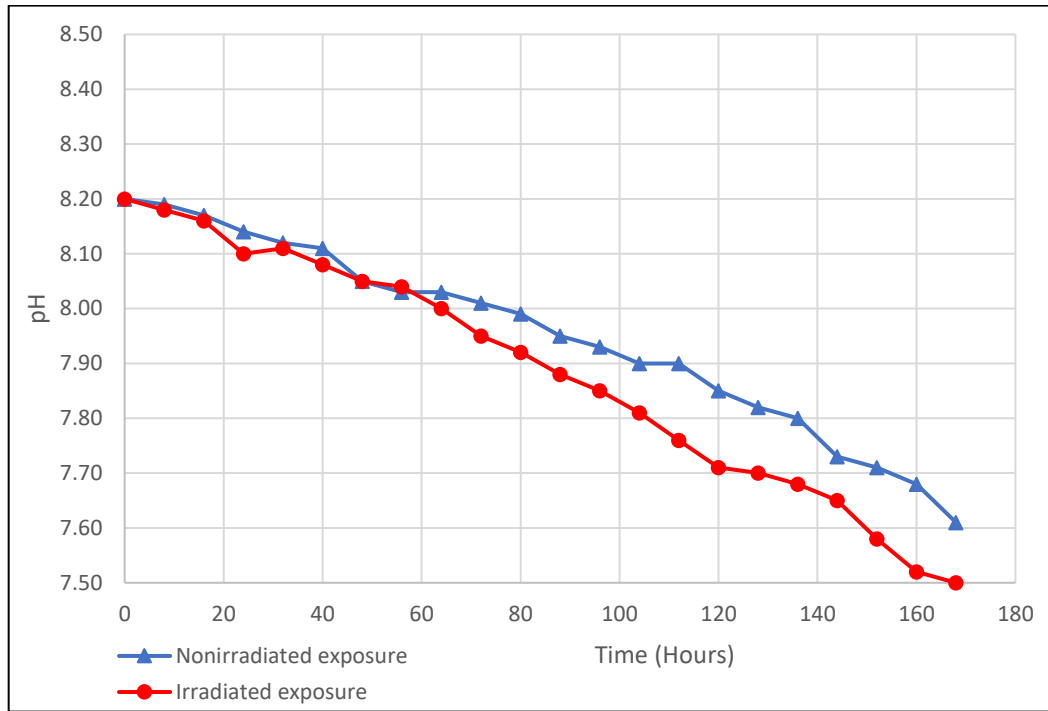


**Figure 4-19: Changes in pH exposed to the environment without any aluminum sample in the presence and absence of  $\gamma$ -radiation.**

#### **4.8 The Effect of Gamma Radiation on Aluminum Alloy Corrosion at Room Temperature**

The impact of radiation on the corrosion behavior of materials is dependent on the intensity of the incident radiation. The radiation source for this experiment is cobalt 60 with a strength of 4  $\mu\text{Ci}$ , which interacts with the test medium leaving a track of ions as the radiation reacts with the solution. The quantity of radiation absorbed is dependent on the thickness of the sample and the length traversed in the solution. The amount absorbed by the medium determines the rate of interaction between the corrosion medium and the

samples. The amount of radiation absorbed could be determined from the interaction between the gamma source and the test medium because not all gamma emitted will be detected by the detector.

In determining the rate of absorption, an initial count is first obtained by measuring the activity absorbed by the detector without any material between the detector and the gamma source. The activity of the radioactive source can be obtained using the formula below:

$$A = \frac{R}{\varepsilon_{peak} \frac{\Delta\Omega}{4\pi} B} \quad (4-4)$$

Where A is the activity, R is the photon detection rate,  $\varepsilon_{peak}$  is the efficiency of the detector, which relates to the number of photons within a specific peak  $N_{Peak}$  to the total number of peaks generated striking the detector  $N_{Total}$ ,  $\varepsilon_{peak} = \frac{N_{peak}}{N_{tot}}$ . The peak efficiency is best calculated by utilizing the Monte Carlo code to transport radiation through a detector material.

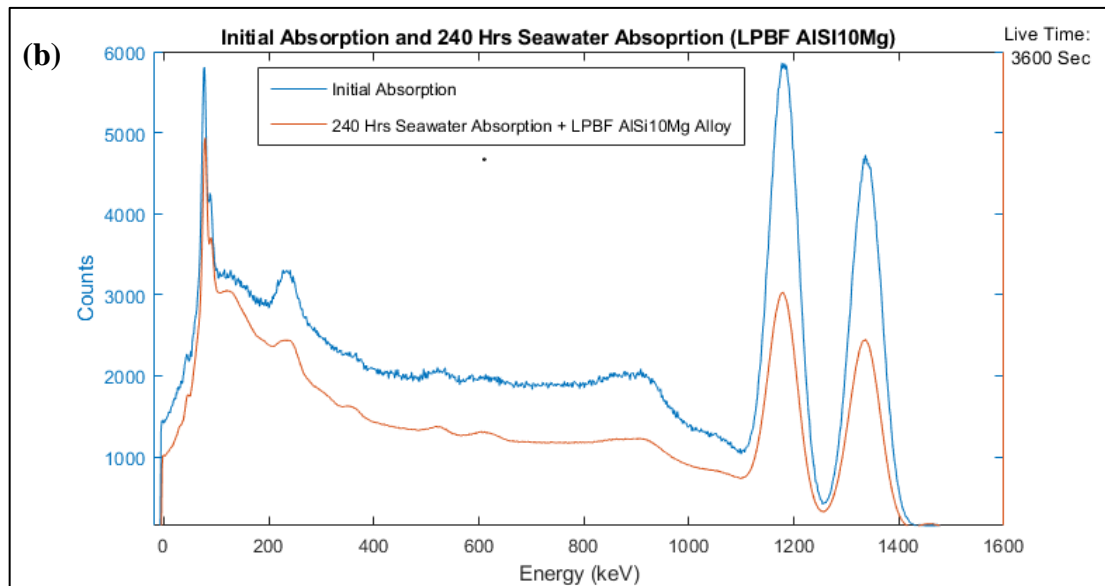
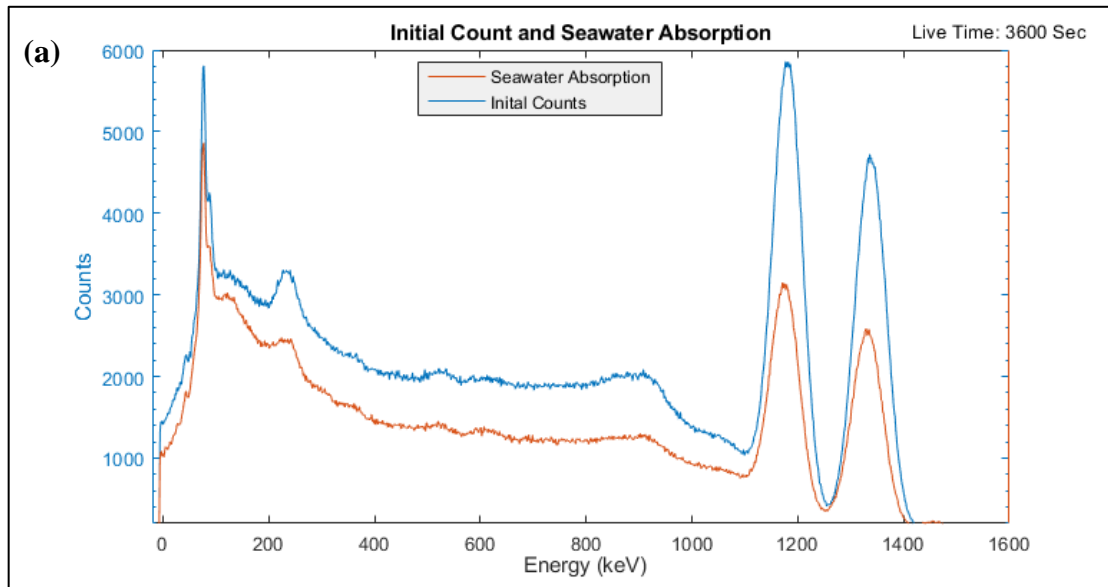
Several codes could be used for this analysis, such as PENELOPE [86], GEANT3 [87], [88]. The GEANT3 code was applied to the 3" x 3" NaI(Tl) detector having an aluminum window with a thickness of 0.05 cm to obtain the peak efficiencies of cobalt 60 with energy levels 1173.2 keV and 1332.5 keV [88].  $\frac{\Delta\Omega}{4\pi}$  is the geometric acceptance defined by the angle between the radiation source and the detector. The results obtained from the source activity model equation (4-4), can help determine the source strength [88]. The amount absorbed can be calculated from the difference between the initial source intensity and the absorption test section, as shown in **Figure 3-3**. The amount absorbed describes

the interaction of photons with water molecules. The plots in Figure 4-20a show that the initial source strength is low. Therefore, the number of absorbed photons will be low, so there is no extensive effect of radiation on the sample.

As the radiation transmits through the water medium, the energy lost is being absorbed by the solution giving rise to a trail of excited and ionized molecules and atoms along the particle pathways. The concentration of the species produced in a track determines the type of chemical reaction observed in the solution. The results obtained from **Figure 4-20** show the initial exposure with a rate of 5861 and 4723 counts per hour under their respective energy levels of 1173.2 and 1332.5 keV. Then, when the seawater solution is the absorber showed a reduced count rate of 3129 and 2557 counts per hour under the energy levels of 1173.2 and 1332.5 keV, as shown in **Figure 4-20a**. When three (3) LPBF aluminum alloys were used for this analysis and immersed in ASW in the presence of  $\gamma$ -radiation, a reduced count rate of 3033 and 2449 counts per hour was recorded, as shown in **Figure 4-20b**. The exposure with four (4) cast A360.1 aluminum alloys to ASW in the presence of  $\gamma$ -radiation showed a further reduced count rate of 2970 and 2399 counts per hour for the energy levels 1173.2 and 1332.5 keV, respectively, as shown in **Figure 4-20c**. The rate of absorption is low; therefore, the extent of gamma interaction will be short; any form of ionization resulting from this will be around the ground state, thereby forming clusters of ionized or excited species within the same locality.

On continuous exposure to radiation for about 96 hours with aluminum sample and seawater as absorbers, some of the excited species might have enough energy to move farther from the ground state forming their tracks depending on the intensity of the incoming photon. The behavior of these excited molecules, ions, and free radicals formed

from radiation exposure leads to various chemical changes. The linear energy transfer rate determines the energy deposited in a medium when ionizing radiation traverses the medium. The amount of energy deposited at various parts of the medium differs because photons tend to slow down as they pass through a medium.



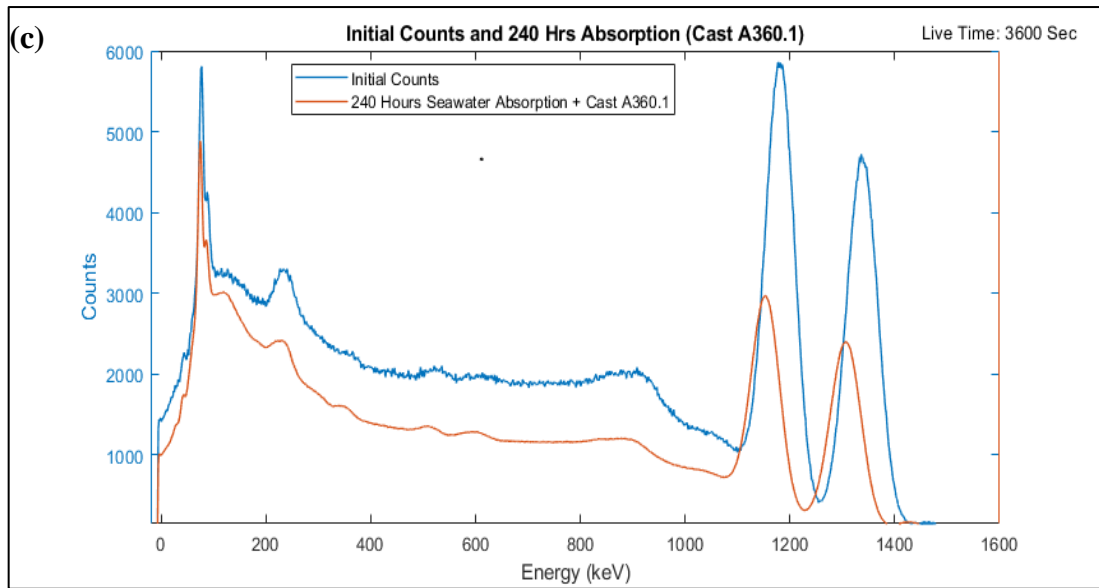
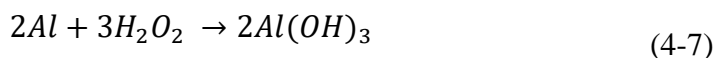


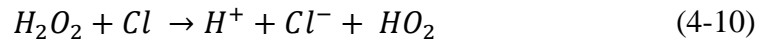
**Figure 4-20: Radiation counts for gamma rays as a function of energy. (a) Initial counts and seawater absorption (b) Initial counts and LPBF AlSi10Mg + seawater absorption (c) Initial counts and cast A360.1 + seawater absorption**

The overall effect of radiation on metals (aluminum alloys) relates to the effect these radiolytic products have on the protective layer (oxide film) and the corrodent (seawater) as the transient species recombine to form water. These products of water radiolysis react with atomic aluminum causing them to be oxidized to aluminum oxides, which tends to form a shielding layer on the alloy surface, preventing further corrosion:

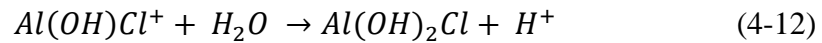
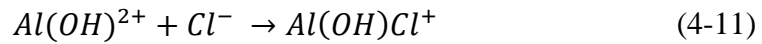


The presence of these oxides should prevent the increased corrosion noticed after descaling. However, aggressive ions present in the solution increased the corrosion of the samples as they tend to diffuse through the oxide layers to attack the metal matrix. EDS

results from **Figure 4-12d**, and **Figure 4-14c** confirmed the presence of oxygen on the alloy surface, which could form various compounds of aluminum. However, XRD and Raman results did not prove this due to the amorphous nature of the oxide film. Also, water radiolysis products tend to recombine to form water. However, the presence of aggressive ions in ASW, for example, chloride ions, tends to interfere with these recombination reactions by reacting with the radicals, as shown below [89].



Radiolysis of water tends to produce per hydroxyl in situ, which has a high oxidizing nature, and short-lived. It can be present on the alloy surface close to the intermetallic particles, especially for the cast A360.1 forming the hydroxides shown in equation (4-5) and (4-7), which can react with some of the aggressive ions present in ASW such as  $Cl^{-}$  forming the chloride complexes shown below:



This explains the continuous attack on the surface of the alloy, as the oxide film formed on the A360.1 was not enough to stop the migration of aggressive ions to the metal's surface. After descaling, there was an increased form of corrosion attack around the intermetallic particles on the cast A360.1 alloy. The LPBF AlSi10Mg alloys, which formed a thin film dark grayish layer on the alloy surface, suffered from uniform weight

loss. Therefore, both alloys corroded more in the presence of radiation due to increasing oxidizing agents available in the solution as a result of radiation, which looks strange considering the low intensity of interacting photons. Further studies should consider repeating this experiment at a higher dose rate to determine the contribution of radiation to the corrosion behavior of these alloys.

## **4.9 Relevance to Nuclear Powered Systems**

As discussed in chapter 1, the objective of this work is specific; there is a need to discuss the relevance of this work to the nuclear-powered reactors. Regrettably, there are very few literature data on the irradiation-assisted corrosion of containment materials such as aluminum alloys that occur in reactor containment building and may be exposed to radioactive emergency coolant LOCA. Some aspects of this experiment differ from what is experienced in an actual reactor, for example, the coolant used and the dose rate observed in an actual reactor condition. Two significant areas will be discussed: the dose rate and how it applies to what is obtainable in the reactor condition, secondly how the application of LPBF alloy can help mitigate the clogging of sump strainers better than cast alloy.

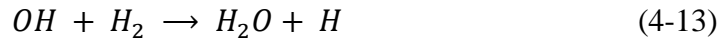
### **4.9.1 Dose Rate**

The impact of gamma radiation on the corrosion of aluminum alloys has been examined in this work using a low dose rate of 0.58  $\mu\text{Gy/hr}$  measured using a NaI detector and calculated using Monte Carlo GEANT3 code [88]. This dose is low to be compared with any operation in a real reactor. However, it can act as a starting point for understanding how ionizing radiation in the reactor containment building affects aluminum alloys. The dose rate used in this study is different from the dose found in an actual reactor



environment; therefore, this has a different effect on the corrosion of aluminum alloys, yield, and nature of radiolysis products.

The dominant species formed after steady-state irradiation is  $H_2O_2$ . It can be suppressed by the presence of molecular hydrogen occurring in the solution where OH radical is reduced before the formation of  $H_2O_2$  [90].



The concentration of OH strongly depends on the dose rate. In contrast, the concentration of molecular hydrogen relies upon the pH of the solution and radiation dose as hydrogen is liberated during radiation interaction.

At the low dose used in this experiment, the product of equation (4-14) is low, which is indicated by the thin dark grayish layer on the exterior of the LPBF alloy, while the products of equation (4-13) continue to increase based on the irradiation time as recombination reactions continue to occur. One can conclude that at a low dose rate, the available molecular hydrogen did not suppress radiolysis products' formation as different effects of radiation were seen on the different aluminum alloys used for this experiment. This is due to the presence of oxygen, leading to increased oxide deposits in the presence of radiation than those in the absence of radiation.

The cast A360.1 showed increased corrosion product deposits in the presence of radiation as compared with the absence of radiation, while the LPBF showed a darker grayish layer on the alloy surface in the presence of radiation as compared with the absence of radiation, which can all be ascribed to the presence of  $H_2O_2$  in the experimental test cell. Adding hydrogen gas could be a possible way to suppress the water dissociation and remove

oxygen but can have various effects. A high concentration of hydrogen increases the pH of the water, forming ammonia as air containing nitrogen could be introduced into the system. Also, high oxygen concentration relative to hydrogen decreases the pH of water, as seen in **Figure 4-19**, as nitric acid is formed. The presence of nitric acid in the solution was not confirmed but could be one of the contributing factors to the decline in pH aside from CO<sub>2</sub> decomposition.

A higher dose rate experiment should be performed to determine if the phenomena observed in the low dose rate samples are still present at a dose rate one order of magnitude higher. Some of the irradiation effects found in this study may be available in the containment building relying upon the temperature differences, higher dose rate, and pH of the solution/coolant used.

#### **4.9.2 Longer Operating Time**

It is useful to envision the applicability of this work to prolonged corrosion times. The samples studied in this experiment were exposed to seawater for corrosion for 24 – 240 hours, but aluminum alloys occurring in the containment exposed to recirculating treated water may be in operation longer than 240 hours.

The results obtained in this work have shown that irradiation impacts the corrosion behavior of the aluminum alloys in seawater with similar compositions but manufactured using different manufacturing processes. At this short time, different forms of corrosion products were formed because of ionizing radiation. At longer irradiation time, the thickness of the corrosion product deposit would probably increase, covering the entire

surface of the alloy; this can be seen in **Figure 4-12b**, which showed an increased corrosion product deposit in the presence of radiation.

The presence of increased corrosion product deposits can limit the interaction of aggressive ions such as chloride ions from electrical cable insulators or other ions present in the solution and/or coolant from corroding the metal matrix. Hence, reducing the corrosion rate as the aggressive ions find it difficult to penetrate through the thick oxide films. Also, spallation of the corrosion product deposits can occur at a longer operating time combining with other precipitates in the sump to clog the strainers, thereby leading to significant head loss across the recirculation pump, therefore leading to the failure of ECCS.

#### **4.9.3 Summary of the Relevance of this Research to Nuclear Powered Systems**

The dose rates used in this study are lower than what can occur under specific scenarios in an existing reactor condition but may occur in containments during normal operation or even shutdowns. Limited evidence suggests that irradiation increases the corrosion product deposits of aluminum alloys at a higher dose rate and longer exposure time. Previous studies have suggested an increase in the corrosion potential of other materials such as stainless steel [91], Inconel 600 [92], and carbon steel [93]. Based on these studies combined with the experience gained in this study, we can assume a continuous corrosion product deposit on alloy surfaces leading to spallation effects and increasing the clogging effect of sump strainers.

These effects occur if seawater is used as extra cooling when ECCS runs short of recirculating treated water. However, this study serves as a starting point in studying the

effect of ionizing radiation on aluminum alloys in a containment building. Future work will require repeating this experiment with a borate solution typically used in the containment building to verify if these effects occur on the alloys. This could help mitigate the clogging of sump strainers if effects were noticed when a borate solution was used as the coolant.

## 5. Conclusions and Future Work

### 5.1 Conclusions

This thesis examined the corrosion behavior and microstructure of two aluminum alloys (cast A360.1 and LPBF AlSi10Mg) and how gamma radiation affects the corrosion process of these two Al alloys in seawater. It revealed that  $\gamma$ -radiation had an effect on the oxidation of aluminum alloys.

In comparing the irradiated and unirradiated cast A360.1 samples' weight changes, the result obtained showed that gamma radiation caused a significant variation in the nature and amount of the oxide film produced. The irradiated cast A360.1 Al alloy showed a higher weight gain than its non-irradiated counterpart. Also, the LPBF AlSi10Mg alloy followed similar behavior as there was significant variation between the weight changes of the irradiated and non-irradiated. The LPBF AlSi10Mg showed a weight loss, and when exposed to gamma radiation, the irradiated showed a higher weight loss than that of non-irradiated. The results from descaling the irradiated LPBF AlSi10Mg have a more significant standard error in their weight changes than those of the non-irradiated counterpart. Therefore, the oxidation of aluminum alloys is a complex process, and interpreting the weight changes resulting from oxidation should be done with caution. However, the weight variations detected in this study can stand as a guide, though limited, to irradiation's overall effect on the corrosion behavior of the aluminum alloys.

Combining surface examination techniques has provided us with insight into the elemental species and enabled us to observe the oxide and structure composition with corrosion. The results showed the IMPs inherent in the cast A360.1 alloy could be trenced from the

metal matrix as the alloy interacts with seawater solution while the Al-Si matrix is somehow retained. An oxide film formed on the cast alloy surface, and at the short exposure time (240 hours), the composition of the outer oxide surface was identified by EDS surface analysis to contain O, Al, Si, and Mg. The presence of oxygen on the surface can depict the formation of aluminum oxide on the inner surface or outer surface, but XRD results on the cast A360.1 showed Al and Si peaks' presence. Peaks of sodium sulfate result from the seawater solution concentrated in the oxide films, mainly the outer layer in the localized patches, while no aluminum oxide peak was noticed.

On the other hand, the LPBF AlSi10Mg alloy exhibited a different behavior due to the absence of IMP in the alloy owing to its perfect solidification and cooling characteristics. The oxide films formed on this alloy are compact, thin, and appeared with a dark grayish coloration on the alloy surface with few patches of white oxide deposit in the presence of radiation resulting from the presence of  $H_2O_2$ , which is an oxidizing species present in the solution at a steady state. The EDS and XRD results showed the presence of Al and Si peaks with no other element present in the microstructure.

The LPBF alloy showed a better resistance than its cast counterpart in the presence and absence of radiation in seawater; this shows that the silicon network limits the ability of  $Al^{3+}$  ions to be transferred to the solution, as the metal matrix interacts with the solution. There was a 29% increase in the corrosion of LPBF samples in the presence of radiation compared with the nearly 40% increase in cast A360.1 aluminum samples' corrosion. The excellent corrosion characteristics of LPBF alloy could be attributed to the presence of Si network and the near absence of second phase IMP in the alloy microstructure, reducing the detrimental effect these IMPs have on the alloy. This attribute eliminates the trenching

effect of Fe-bearing IMP, which could be released into the coolant contributing to the clogging of the sump strainers. Therefore, the LPBF alloys manufactured using the additively manufacturing procedure stands as a better replacement component than the conventionally manufactured cast A360.1 alloy in the containment building.

Irradiation caused an increase in oxide deposits: corrosion product deposits were evident on all irradiated samples more than the unirradiated samples. The presence of these corrosion products on the sample surface detected using SEM shows the dissociation and ionization of water. The Pourbaix diagram can be used to examine the corrosion process or oxide type occurring on the alloy surface. However, the absence of measured potential limited the ability to identify the type and nature of the oxide and phase boundaries. Exposure to irradiated water containing solutes for more extended times causes an increased oxide deposit leading to a spalling of outer oxide deposit. Loss of passive behavior in the cast alloys contributes to the increased debris amount released into the coolant, thereby exacerbating sump strainers' clogging.

Radiolysis was found to be the main driver of irradiation-accelerated corrosion as non-irradiated samples showed a porous layer with tiny patches of corrosion product deposits

The microstructure and the way an alloy is processed can impact the corrosion characteristics. This thesis provides a roadmap to a good understanding of the microstructural corrosion relationship of cast A360.1 and LPBF AlSi10Mg in the presence of ionizing radiation. This will guide nuclear material scientists in modifying the microstructure for alloying to produce high-quality alloys to reduce susceptibility to corrosion and contribution to clogging of the sump strainers.

The work's principal objective was to know the corrosion of aluminum alloys manufactured using different procedures and the influence of ionizing radiation on the corrosion process in an electrolyte. We have accomplished this objective and demonstrated that the presence of ionizing radiation influences aluminum alloys' corrosion behavior.

## **5.2 Future Work**

This study provided an understanding of the corrosion behavior of aluminum alloys in a radiation environment. The aluminum alloys used were produced using different manufacturing procedures, which yielded different microstructures, as corrosion is affected by the processing method and microstructure.

In order to understand the corrosion behavior of aluminum alloys in a radiolytic environment using the gravimetric method, it is imperative to design an electrochemical experiment that can study the interaction of corrosion rate and radiation chemistry yields on the surface of the alloys. In a radiolytic system, the presence of radiolysis species tends to affect the corrosion behavior of the alloy. Studying how they affect corrosion behavior changes will contribute significantly to our knowledge of how radiation affects corrosion of both alloys and provide useful data into using LPBF alloys as a replacement component in a containment inundated with radioactive emergency coolant.

The consequence of alloying components on the passivation and localized corrosion, focusing on the effect of water radiolysis, should be investigated. The cast A360.1 contains several shapes and sizes of the second phase intermetallic particles; the electrochemical behavior of these phases in the presence of radiation should be



investigated. In contrast, the Si-network behavior on the LPBF alloy should be investigated to identify its contribution to the deterioration of the alloy and how different zones found on this alloy contributes to the corrosion behavior of the alloy.

Borate solution is a standard coolant used in the containment building under post – LOCA events where aluminum alloys contact radioactive emergency coolants forming corrosion products. The surface assimilation of borate anions on the aluminum interface can affect the film formation on the alloy surface. Corrosion of aluminum in borate solution should be compared with that of seawater, which contains a high amount of chloride and other aggressive ions that can undergo radiolysis in high and low gamma radiation.

The presence of radiation at a higher dose can increase the hydrogen in the seawater solution leading to hydrogen-assisted intragranular corrosion, especially for the cast alloy containing several intermetallics. Also, there is a high tendency of hydrogen ion formation at the bottom of the pit, thereby increasing the hydrogen effusion zone. Hydrogen generation should be investigated to determine its contribution to the corrosion behavior of the alloys.

## References

- [1] P. Fathi, M. Mohammadi, X. Duan, and A. M. Nasiri, “A comparative study on corrosion and microstructure of direct metal laser sintered AlSi10Mg\_200C and die-cast A360.1 aluminum,” *J. Mater. Process. Technol.*, vol. 259, no. October 2017, pp. 1–14, 2018, doi: 10.1016/j.jmatprotec.2018.04.013.
- [2] K. J. Howe, L. Mitchell, S. J. Kim, E. D. Blandford, and E. J. Kee, “Corrosion and solubility in a TSP-buffered chemical environment following a loss of coolant accident: Part 1 - Aluminum,” *Nucl. Eng. Des.*, vol. 292, pp. 296–305, Oct. 2015, doi: 10.1016/j.nucengdes.2014.11.021.
- [3] S. Guo, B. Dsouza, Y. Xie, A. Leong, J. J. Leavitt, and J. Zhang, “Aluminum corrosion in reactor containment environment following a loss of coolant accident (LOCA): High-temperature flow loop tests,” *Corros. Sci.*, vol. 151, pp. 122–131, May 2019, doi: 10.1016/j.corsci.2019.02.021.
- [4] US NRC, “NRC: Bulletin 96-03: Potential Plugging of Emergency Core Cooling Suction Strainers by Debris in Boiling-Water Reactors,” *NRC LIBRARY*, 1996. [Online]. Available: <https://www.nrc.gov/reading-rm/doc-collections/gen-comm/bulletins/1996/bl96003.html>. [Accessed: 27-May-2020].
- [5] E. C. Beahm, C. F. Weber, T. S. Kress, and G. W. Parker, “Iodine Chemical Forms in LWR Severe Accidents Final Report,” Tennessee, USA, 1992.
- [6] D. Chen *et al.*, “Experimental analysis of the aqueous chemical environment following a loss-of-coolant accident,” *Nucl. Eng. Des.*, vol. 237, no. 20–21, pp. 2126–2136, Nov. 2007, doi: 10.1016/j.nucengdes.2007.02.010.
- [7] C. H. Delegard *et al.*, *Evaluation of Chemical Effects Phenomena in Post-LOCA Coolant - Final Report*. Richland, Washington: U.S Nuclear Regulatory Commission, 2009.

- [8] C. B., Bahn, K. E. Kasza, W. J. Shack, K. Natesan, and P. Klein, "Evaluation of precipitates used in strainer head loss testing. Part I. Chemically generated precipitates," *Nucl. Eng. Des.*, vol. 239, no. 12, pp. 2981–2991, Dec. 2009, DOI: 10.1016/j.nucengdes.2009.09.023.
- [9] J. Huang, D. Lister, S. Uchida, and L. Liu, "The corrosion of aluminum alloy and release of intermetallic particles in nuclear reactor emergency core coolant: Implications for clogging of sump strainers," *Nucl. Eng. Technol.*, vol. 51, no. 5, pp. 1345–1354, Aug. 2019, doi: 10.1016/j.net.2019.02.012.
- [10] Dave Lochbaum, "Reactor Core Cooling," *Union of Concerned Scientists*, 2011. [Online]. Available: <https://allthingsnuclear.org/dlochbaum/reactor-core-cooling>. [Accessed: 21-May-2020].
- [11] J. R. Davis, "Aluminum and aluminum alloys," *ASM International*, 1999. [Online]. Available: [https://books.google.ca/books/about/Aluminum\\_and\\_aluminum\\_alloys.html?id=G49UAAAAMAAJ&redir\\_esc=y](https://books.google.ca/books/about/Aluminum_and_aluminum_alloys.html?id=G49UAAAAMAAJ&redir_esc=y). [Accessed: 16-Mar-2020].
- [12] J. G. Kaufman and E. L. Rooy, *Aluminum Alloy Castings: Properties, Processes, and Applications.*, First Edit. OHIO: ASM International, 2004.
- [13] P. N. H. Nakashima, "The Crystallography of Aluminum and Its Alloys," in *Encyclopedia of Aluminum and Its Alloys*, CRC Press, 2019.
- [14] S. R. S. B.D., Cullity, *Elements of X-Ray Diffraction*, vol. 108, no. 2. 2014.
- [15] M. Tilli and A. Haapalinna, "Properties of Silicon," in *Handbook of Silicon-Based MEMS Materials and Technologies: Second Edition*, Elsevier Inc., 2015, pp. 3–17.
- [16] S. Ikhmayies, "Phase Diagrams of Al-Si System," in *Minerals, Metals and Materials Series*, 2019, pp. 231–237, DOI: 10.1007/978-3-030-06209-5\_24.
- [17] W. Li *et al.*, "Effect of heat treatment on AlSi10Mg alloy fabricated by selective laser melting: Microstructure evolution, mechanical properties, and fracture mechanism," *Mater. Sci. Eng. A* vol. 663, pp. 116–125, Apr. 2016, doi: 10.1016/J.MSEA.2016.03.088.

- [18] J. D. G. R. William D. Callister, *Materials Science and Engineering: An Introduction*, Ninth. Wiley, 2013.
- [19] D. Manfredi *et al.*, “From Powders to Dense Metal Parts: Characterization of a Commercial AlSiMg Alloy Processed through Direct Metal Laser Sintering,” *Materials (Basel)*, vol. 6, no. 3, pp. 856–869, Mar. 2013, doi: 10.3390/ma6030856.
- [20] C. K. Baxter, “Mechanical Characterization and Constitutive Modelling of Additively,” *Masters Thesis, Univ. New Brunswick, Canada*, 2018.
- [21] A. Sola and A. Nouri, “Microstructural porosity in additive manufacturing: The formation and detection of pores in metal parts fabricated by powder bed fusion,” *J. Adv. Manuf. Process.*, vol. 1, no. 3, Jul. 2019, doi: 10.1002/amp2.10021.
- [22] J. R. Davis, *ASM Handbook Aluminum, and Aluminum Alloys*. ASM International, 1993.
- [23] A. Jordan, “Microstructure Characterization and Corrosion Properties of Two Recycled Aluminium Alloys AA5050 and AA5011,” *Ph.D.Thesis, Manchester Univ. UK*, 2016.
- [24] C. Y. Chao, “A Point Defect Model for Anodic Passive Films,” *J. Electrochem. Soc.*, vol. 128, no. 6, p., 1187, 1981, DOI: 10.1149/1.2127591.
- [25] M. Pourbaix, “Atlas of electrochemical equilibria in aqueous solutions. Houston: NACE International,” *Mater. Sci. Forum*, pp. 43–54, 1974, DOI: 10.4028/www.scientific.net/msf.251-254.143.
- [26] P. Gimenez, J. J. Rameau, and M. C. Reboul, “Experimental pH Potential Diagram of Aluminum for Seawater.,” *Corrosion*, vol. 37, no. 12, pp. 673–682, 1981, DOI: 10.5006/1.3577557.
- [27] C. Vargel, M. Jacques, and M. P. Schmidt, *Corrosion of aluminum*. Elsevier, 2004.
- [28] B. Zaid, D. Saidi, A. Benzaid, and S. Hadji, “Effects of pH and chloride concentration on pitting corrosion of AA6061 aluminum alloy,” *Corros. Sci.*, vol. 50, no. 7, pp. 1841–1847, 2008, doi: 10.1016/j.corsci.2008.03.006.

- [29] Z. Szklarska-Smialowska, "Pitting corrosion of aluminium," *Corros. Sci.*, vol. 41, no. 9, pp. 1743–1767, 1999, doi: 10.1016/S0010-938X(99)00012-8.
- [30] S. Gustafsson, "Corrosion properties of aluminum alloys and surface treated alloys in tap water," *Sapa Technol.*, 2011.
- [31] M. Liang, R. Melchers, and I. Chaves, "Corrosion and pitting of 6060 series aluminum after two years exposure in seawater splash, tidal and immersion zones," *Corros. Sci.*, vol. 140, pp. 286–296, Aug. 2018, doi: 10.1016/j.corsci.2018.05.036.
- [32] D. . Lide, "CRC Handbook of Chemistry and Physics: A Ready-Reference of Chemical and Physical Data, 85th ed Edited by David R. Lide (National Institute of Standards and Technology). CRC Press LLC: Boca Raton, FL. 2004. 2712 pp. \$139.99. ISBN 0-8493-0485-7.," *J. Am. Chem. Soc.*, vol. 127, no. 12, pp. 4542–4542, Mar. 2005, doi: 10.1021/ja041017a.
- [33] K. Daub and J. C. Wren, "A Study of Gamma Radiation-Induced Carbon Steel Corrosion," *Ph.D. Thesis, Univ. West. Ontario, Canada*, 2013.
- [34] J. W. T. Spinks and R. J. Woods, *An introduction to radiation chemistry*, Third Edit. Toronto: John Wiley & Sons, Inc., 1990.
- [35] M. Behazin, "Radiation-Induced Corrosion of Stellite-6," *Electron. Thesis Diss. Repos. 2434.*, no. October p. 310, 2014.
- [36] A. O. Allen, C. J. Hochanadel, J. A. Ghormley, and T. W. Davis, "Decomposition of water and aqueous solutions under mixed fast neutron and gamma radiation," *J. Phys. Chem.*, vol. 56, no. 5, pp. 575–586, 1952, doi: 10.1021/j150497a007.
- [37] M. T. Simnad, "Influence of radiation upon corrosion and surface reactions of metals and alloys," *Gen. At. Div., Gen. Dyn. Corp., San Diego, Calif.*, 1957.
- [38] F. H. Krenz, "Corrosion of Aluminum-Nickel Type Alloys In High-Temperature Aqueous Service," *Corrosion*, vol. 13, no. 9, pp. 43–49, Sep. 1957, DOI: 10.5006/0010-9312-13.9.43.

- [39] B. Borasky, R; Mastel, “Surface structure of pile, irradiated 2S Aluminum (Technical Report) | OSTI.GOV,” *Hanford Atomic Products Operation, Richland, Wash.*, 1957. [Online]. Available: <https://www.osti.gov/biblio/4349002>. [Accessed: 30-Apr-2020].
- [40] J. J. Stobbs and A. J. Swallow, “Effects of Radiation on Metallic Corrosion,” *Metall. Rev.*, vol. 7, no. 1, pp. 95–132, 1962, DOI: 10.1179/mtrl.1962.7.1.95.
- [41] K. Kanjana, P. Ampornrat, and J. Channuie, “Gamma-radiation-induced corrosion of aluminum alloy: Low dose effect,” *J. Phys. Conf. Ser.*, vol. 860, no. 1, p. 12041, 2017, DOI: 10.1088/1742-6596/860/1/012041.
- [42] M. Kawaguchi, K. Ishigure, N. Fujita, and K. Oshima, “Effect of radiation on the release of corrosion products in a high-temperature aqueous system,” *Radiat. Phys. Chem.*, vol. 18, no. 3–4, pp. 733–740, Jan. 1981, DOI: 10.1016/0146-5724(81)90196-5.
- [43] K. Ishigure, N. Fujita, T. Tamura, and K. Oshima, “Effect of Gamma Radiation on the Release of Corrosion Products From Carbon Steel and Stainless Steel in High-Temperature Water.,” *Nucl. Technol.*, vol. 50, no. 2, pp. 169–177, 1980, doi: 10.13182/NT80-A32543.
- [44] K. Ishigure, H. Ikuse, K. Oshima, N. Fujita, and S. Ono, “The effect of radiation on the release of corrosion products from 304 stainless steel in high-temperature water—II,” *Radiat. Phys. Chem.*, vol. 21, no. 3, pp. 281–287, Jan. 1983, doi: 10.1016/0146-5724(83)90156-5.
- [45] S. Guo, J. J. Leavitt, X. Zhou, E. Lahti, and J. Zhang, “Corrosion of aluminum alloy 1100 in post-LOCA solutions of a nuclear reactor,” *RSC Adv.*, vol. 6, no. 50, pp. 44119–44128, 2016, doi: 10.1039/c6ra07440e.
- [46] J. C. Griess and A. L. Bacarella, “Nuclear Technology The Corrosion of Materials in Reactor Containment Spray Solutions.,” 2017, DOI: 10.13182/NT71-A16264.

- [47] H. Asgari, C. Baxter, K. Hosseinkhani, and M. Mohammadi, "On microstructure and mechanical properties of additively manufactured AlSi10Mg\_200C using recycled powder," *Mater. Sci. Eng. A* vol. 707, pp. 148–158, Nov. 2017, doi: 10.1016/J.MSEA.2017.09.041.
- [48] Pamela A. Yakabuskie, "The Influence of Long-Term Gamma-Radiation and Initially Dissolved Chemicals on Aqueous Kinetics and Interfacial Processes," Ph.D. Thesis, The University of Western Ontario, 2015.
- [49] S. S. Raiman, "Irradiation accelerated corrosion of 316L stainless steel in simulated primary water," *IOSR J. Econ. Financ.*, vol. 3, no. 1, p. 56, 2016, DOI: <https://doi.org/10.3929/ethz-b-000238666>.
- [50] R. Arrabal, B. Mingo, A. Pardo, M. Mohedano, E. Matykina, and I. Rodríguez, "Pitting corrosion of rheocast A356 aluminum alloy in 3.5 wt.% NaCl solution," *Corros. Sci.*, vol. 73, pp. 342–355, Aug. 2013, doi: 10.1016/J.CORSCI.2013.04.023.
- [51] N. Birbilis and R. G. Buchheit, "Electrochemical Characteristics of Intermetallic Phases in Aluminum Alloys," *J. Electrochem. Soc.*, vol. 152, no. 4, p. B140, Mar. 2005, doi: 10.1149/1.1869984.
- [52] S. G. Shabestari, "The effect of iron and manganese on the formation of intermetallic compounds in aluminum-silicon alloys," *Mater. Sci. Eng. A* vol. 383, no. 2, pp. 289–298, Oct. 2004, doi: 10.1016/J.MSEA.2004.06.022.
- [53] P. Fathi, M. Rafieezad, X. Duan, M. Mohammadi, and A. M. Nasiri, "On microstructure and corrosion behavior of AlSi10Mg alloy with low surface roughness fabricated by direct metal laser sintering," *Corros. Sci.*, vol. 157, pp. 126–145, Aug. 2019, doi: 10.1016/j.corsci.2019.05.032.
- [54] L. Thijs, K. Kempen, J.-P. Kruth, and J. Van Humbeeck, "Fine-structured aluminum products with controllable texture by selective laser melting of pre-alloyed AlSi10Mg powder," *Acta Mater.*, vol. 61, no. 5, pp. 1809–1819, Mar. 2013, doi: 10.1016/J.ACTAMAT.2012.11.052.

- [55] J. Pakkanen *et al.*, “On the Selective Laser Melting (SLM) of the AlSi10Mg Alloy: Process, Microstructure, and Mechanical Properties,” *Materials (Basel)*., vol. 10, no. 1, p. 76, 2017, DOI: 10.3390/ma10010076.
- [56] X. Liu, C. Zhao, X. Zhou, Z. Shen, and W. Liu, “Microstructure of selective laser melted AlSi10Mg alloy,” *Mater. Des.*, vol. 168, p. 107677, Apr. 2019, doi: 10.1016/J.MATDES.2019.107677.
- [57] I. Rosenthal, A. Stern, and N. Frage, “Microstructure and Mechanical Properties of AlSi10Mg Parts Produced by the Laser Beam Additive Manufacturing (AM) Technology,” *Metallogr. Microstruct. Anal.*, vol. 3, no. 6, pp. 448–453, Dec. 2014, doi: 10.1007/s13632-014-0168-y.
- [58] C. Yan, L. Hao, A. Hussein, P. Young, J. Huang, and W. Zhu, “Microstructure and mechanical properties of aluminum alloy cellular lattice structures manufactured by direct metal laser sintering,” *Mater. Sci. Eng. A* vol. 628, pp. 238–246, Mar. 2015, doi: 10.1016/j.msea.2015.01.063.
- [59] A. M. Ahern, P. R. Schwartz, and L. A. Shaffer, “Characterization of Conversion-Coated Aluminum Using Fourier Transform Infrared and Raman Spectroscopies,” *Appl. Spectrosc.*, vol. 46, no. 9, pp., 1412–1419, 1992, DOI: 10.1366/0003702924123764.
- [60] R. H. Brown, B. E. Roetheli, and H. O. Forrest, “The Initial Corrosion Rates of Metals,” *Ind. Eng. Chem.*, vol. 23, no. 4, pp. 350–352, Apr. 1931, doi: 10.1021/ie50256a002.
- [61] H. Ezuber, A. El-Houd, and F. El-Shawesh, “A study on the corrosion behavior of aluminum alloys in seawater,” *Mater. Des.*, vol. 29, no. 4, pp. 801–805, Jan. 2008, DOI: 10.1016/j.matdes.2007.01.021.
- [62] Z. Szklarska-Smialowska, “Insight Into the Pitting Corrosion Behavior of Aluminium Alloys,” *Corrosion Sci.*, vol. 33, no. 8, pp. 1193–1202, 1992, DOI: 10.1016/0010-938X(92)90130-U.



- [63] R. T. Loto and A. Adeleke, “Corrosion of Aluminum Alloy Metal Matrix Composites in Neutral Chloride Solutions,” *J. Fail. Anal. Prev.*, vol. 16, no. 5, pp. 874–885, 2016, DOI: 10.1007/s11668-016-0157-3.
- [64] R. E. Melchers, “Bi-modal trend in the long-term corrosion of aluminum alloys,” *Corros. Sci.*, vol. 82, pp. 239–247, May 2014, doi: 10.1016/j.corsci.2014.01.019.
- [65] A. V. Byalobzheskii, “Radiation corrosion / [by] A. V. Byalobzheskii; translated from Russian [by A. Aladjem]. - Version details - Trove,” *Jerusalem : Israel Program for Scientific Translations ; [available from U.S. Dept. of Commerce, Clearinghouse for Federal Scientific and Technical Information, Springfield, Va.], 1970,1970.*[Online].Available:<https://trove.nla.gov.au/work/21288525?selectedversion=NBD114179>. [Accessed: 20-Apr-2019].
- [66] K. A. Yasakau, M. L. Zheludkevich, S. V. Lamaka, and M. G. S. Ferreira, “Role of intermetallic phases in localized corrosion of AA5083,” *Electrochim. Acta*, vol. 52, no. 27, pp. 7651–7659, Oct. 2007, doi: 10.1016/J.ELECTACTA.2006.12.072.
- [67] S. Jain and Syadwad, “Corrosion and protection of heterogeneous cast Al-Si (356) and Al-Si-Cu-Fe (380) alloys by chromate and cerium inhibitors,” *ProQuest Diss. Theses; Thesis (Ph.D.)--The Ohio State Univ. 2006.; Publ. Number AAI3217380; ISBN 9780542687150; Source Diss. Abstr. Int. Vol. 67-05, Sect. B. Page 2779.; 301 p., 2006.*
- [68] K. Ben Mabrouk, T. H. Kauffmann, H. Aroui, and M. D. Fontana, “Raman study of cation effect on sulfate vibration modes in solid-state and in aqueous solutions,” *J. Raman Spectrosc.*, vol. 44, no. 11, pp. 1603–1608, Nov. 2013, doi: 10.1002/jrs.4374.
- [69] N. C. Sindelar, R.L.; Lam, P.S.; Louthan, M.R. Jr.; Iyer, “Corrosion of metals and alloys in high radiation fields,” *Mater. Charact.*, vol. 43, no. 22, 1999.
- [70] I. G. Draganić and Z. D. Draganić, *The radiation chemistry of water*, 1st Editio. New York: Academic Press, 1971.

- [71] R. E. Melchers, *Modelling The Long Term Atmospheric Corrosion Of Aluminium Alloys*. Australia: Centre for infrastructure performance and reliability, 2010.
- [72] F. L. Galeener and J. C. Mikkelsen, “Raman studies of the thermal oxide of silicon,” *Solid State Commun.*, vol. 37, no. 9, pp. 719–723, 1981, doi: 10.1016/0038-1098(81)91085-1.
- [73] D. M. Popovic, V. Milosavljevic, A. Zekic, N. Romcevic, and S. Daniels, “Raman scattering analysis of silicon dioxide single crystal treated by direct current plasma discharge,” *Appl. Phys. Lett.*, vol. 98, no. 5, pp. 13–16, 2011, doi: 10.1063/1.3543838.
- [74] M. M. Khayyat, G. K. Banini, D. G. Hasko, and M. M. Chaudhri, “Raman microscopy investigations of structural phase transformations in crystalline and amorphous silicon due to indentation with a Vickers diamond at room temperature and at 77 K,” *J. Phys. D. Appl. Phys.*, vol. 36, no. 11, pp. 1300–1307, 2003, doi: 10.1088/0022-3727/36/11/310.
- [75] P. Borowicz, A. Taube, W. Rzodkiewicz, M. Latek, and S. Gierabtowska, “Raman Spectra of High- $\epsilon$  Dielectric Layers Investigated with Micro-Raman Spectroscopy Comparison with Silicon Dioxide,” *Sci. World J.*, vol. 2013, 2013, doi: 10.1155/2013/208081.
- [76] R. I. Revilla, J. Liang, S. Godet, and I. De Graeve, “Local Corrosion Behavior of Additive Manufactured AlSiMg Alloy Assessed by SEM and SKPFM,” *J. Electrochem. Soc.*, vol. 164, no. 2, pp. C27–C35, 2016, DOI: 10.1149/2.0461702jes.
- [77] A. Pardo, M. C. Merino, A. E. Coy, R. Arrabal, F. Viejo, and E. Matykina, “Corrosion behavior of magnesium/aluminum alloys in 3.5 wt.% NaCl,” *Corros. Sci.*, vol. 50, no. 3, pp. 823–834, 2008, DOI: 10.1016/j.corsci.2007.11.005.
- [78] T. Schram, “Nondestructive Optical Characterization of Chemical Conversion Coatings on Aluminum,” *J. Electrochem. Soc.*, vol. 145, no. 8, p. 2733, 1998, DOI: 10.1149/1.1838706.

- [79] N. J. Cherepy, T. H. Shen, A. P. Esposito, and T. M. Tillotson, “Characterization of an effective cleaning procedure for aluminum alloys: Surface-enhanced Raman spectroscopy and zeta potential analysis,” *J. Colloid Interface Sci.*, vol. 282, no. 1, pp. 80–86, Feb. 2005, DOI: 10.1016/j.jcis.2004.08.064.
- [80] N. J. Cherepy, T. H. Shen, A. P. Esposito, and T. M. Tillotson, “Characterization of an effective cleaning procedure for aluminum alloys: Surface-enhanced Raman spectroscopy and zeta potential analysis,” *J. Colloid Interface Sci.*, vol. 282, no. 1, pp. 80–86, Feb. 2005, DOI: 10.1016/j.jcis.2004.08.064.
- [81] P. V. V. Thomas, V. Ramakrishnan, and V. K. K. Vaidyan, “Oxidation studies of aluminum thin films by Raman spectroscopy,” *Thin Solid Films*, vol. 170, no. 1, pp. 35–40, Mar. 1989, doi: 10.1016/0040-6090(89)90619-6.
- [82] P. Brewer and K. Hester, “Ocean Acidification and the Increasing Transparency of the Ocean to Low-Frequency Sound,” *Oceanography*, vol. 22, no. 4, pp. 86–93, Dec. 2009, DOI: 10.5670/ocean.2009.99.
- [83] R. S. Hoffman, M. A. Howland, H. N. Kamerow, and L. R. Goldfrank, “Comparison of titratable acid/alkaline reserve and ph in potentially caustic household products,” *Clin. Toxicol.*, vol. 27, no. 4–5, pp. 241–261, 1989, DOI: 10.3109/15563658908994421.
- [84] J. Zhang, M. Klasky, and B. C. Letellier, “The aluminum chemistry and corrosion in alkaline solutions,” *J. Nucl. Mater.*, vol. 384, no. 2, pp. 175–189, 2009, doi: 10.1016/j.jnucmat.2008.11.009.
- [85] E. C. Beahm, R. A. Lorenz, and C. F. Weber, “NUREG/CR-5950, ‘Iodine Evolution and pH Control,’” TN, 1992.
- [86] F. Salvat, J. M. Fernández-Varea, J. Baró, and J. Sempau, “PENELOPE, an algorithm and computer code for Monte Carlo simulation of electron-photon showers,” *Inf. Técnicos Ciemat 799*, 1996.
- [87] R. Brun., *et al.*, “GEANT: Detector Description and Simulation Tool,” 1993, DOI: 10.17181/CERN.MUHF.DMJ1.

- [88] L. Peralta, "Measuring the activity of a radioactive source in the classroom," *J. Phys.*, vol. 25, pp. 211–219, 2004, DOI: 10.1088/0143-0807/25/2/008.
- [89] L. C. Brown and G. E. Boyd, "Production of perchlorate and chlorite ions in crystalline potassium chlorate irradiated with cobalt-60  $\gamma$  rays," *J. Phys. Chem.*, vol. 73, no. 2, pp. 396–400, 1969, doi: 10.1021/j100722a022.
- [90] K. Bobrowski, K. Skotnicki, and T. Szreder, "Application of radiation chemistry to some selected technological issues related to nuclear energy development," *Topics in Current Chemistry*, vol. 374, no. 5. Springer Verlag, pp. 1–48, 18-Aug-2016, doi: 10.1007/s41061-016-0058-7.
- [91] G. P. Marsh, K. J. Taylor, G. Bryan, and S. E. Worthington, "The influence of radiation on the corrosion of stainless steel," *Corros. Sci.*, vol. 26, no. 11, pp. 971–982, Jan. 1986, doi: 10.1016/0010-938X(86)90087-9.
- [92] A. Y. Musa and J. C. Wren, "Combined effect of gamma-radiation and pH on corrosion of Ni–Cr–Fe alloy Inconel 600," *Corros. Sci.*, vol. 109, pp. 1–12, Aug. 2016, doi: 10.1016/j.corsci.2016.03.015.
- [93] K. Daub, X. Zhang, J. J. Noël, and J. C. Wren, "Gamma-radiation-induced corrosion of carbon steel in neutral and mildly basic water at 150°C," *Corrosion Science*, vol. 53, no. 1. Pergamon, pp. 11–16, 01-Jan-2011, doi: 10.1016/j.corsci.2010.09.048.

## Appendix A: Gravimetric Analysis of cast A360.1 and LPBF AlSi10Mg

The results presented in **Table 2** contain the values obtained during the experimental runs, as explained in the gravimetric analysis section 4.2. The cast and LPBF aluminum samples are denoted by various letters (L, H, T, F, etc.) and were weighed before exposure, depicted as the 0 Hrs in **Table 2** under a controlled weighing condition using an analytical balance at the UNB surface science lab. The samples were weighed multiple times to determine the actual weight of the sample, reduce weighing errors, and the average used for analysis. The weight changes of all samples were measured using a Mettler Toledo standard analytical balance with an accuracy of  $\pm 0.05$  mg accuracy. The samples were reweighed after exposure to seawater solution at successive 24, 72, 144, and 240 hours.

The experiment was repeated three times (1<sup>st</sup>, 2<sup>nd</sup>, and 3<sup>rd</sup> run) for both samples (cast and LPBF Al alloys) in the presence and absence of radiation. After all experimental runs, the results obtained from the weighings were analyzed, and the values plotted in **Figure 4-8** and **Figure 4-9**. Each of the samples, either "L" or "H," was analyzed by subtracting the initial weight from the final weight divided by the specific sample area to obtain the total corrosion in  $\text{mg}/\text{cm}^2$ , as shown in **Eq. 1**. The results presented in section 4.2 are obtained by plotting the averages of the three experimental runs in the presence and absence of radiation.

$$\text{Total corrosion} = \frac{\Delta W \text{ (mg)}}{A \text{ cm}^2} \quad \text{Eq. 1}$$

After obtaining the corrosion data at the end of each experimental run of 240 hours, the samples were descaled at 240 hours to determine the sample's corrosion attack rate. This

was done using the method described in section 3.4.3; after that, the sample was reweighed to obtain a new weight, as presented in **Table 2**.

In analyzing the descale data, the following parameters were used;

Weight before exposure =  $W_o$  (mg)

Surface area =  $A$  ( $cm^2$ )

Final weight after corrosion exposure =  $W_1$  (mg)

New descaled final weight =  $W_2$  (mg)

The total corrosion at this stage is obtained by using the expression below

$$\left(\frac{W_o - W_2}{A}\right) \frac{mg}{cm^2} \quad \text{Eq. 2}$$

A blank sample is inserted into the descaling solution along with the corroded samples during descaling, and the blank correction applied to the samples using the formula below

$$\frac{\Delta W_b}{A_b} \frac{(mg)}{cm^2} \quad \text{Eq. 3}$$

Where  $\Delta W_b$  is the blank weight change, and  $A_b$  is the surface area of the blank. Therefore, the blank correction is applied to the corroded sample using the formula below

$$\left(\frac{W_o - W_2}{A}\right) - \left(\frac{\Delta W_b}{A_b}\right) \quad \text{Eq. 4}$$

This blank correction was applied for all the samples and all experimental runs, then the averages of the experimental run plotted in **Figure 4-8** and **Figure 4-9**.

For non-irradiated LPBF AlSi10Mg 1<sup>st</sup> Run for "L" sample; descaling gives

$$\left(\frac{4021.4-4023.7}{11.77}\right) - \left(\frac{2156.3-2156.5}{9.72}\right) = -0.1748 \frac{mg}{cm^2}$$

Inserting the obtained values in Error! Reference source not found. to **Eq. 4** for the first run of the LPBF samples gives the result of descaling for L = -0.1748 mg/cm<sup>2</sup>, T = -0.1663 mg/cm<sup>2</sup>, and J = -0.1714 mg/cm<sup>2</sup>, then an average of these three samples gives -0.1708 mg/cm<sup>2</sup> for the 1<sup>st</sup> run, the 2<sup>nd</sup> run has an average of -0.1385 mg/cm<sup>2</sup> and the 3<sup>rd</sup> run has an average of -0.1281 mg/cm<sup>2</sup>. The total averages for the three runs give an average of -0.1458 mg/cm<sup>2</sup> for the LPBF AlSi10Mg alloy, which is plotted in **Figure 4-9** with the dashed blue line.





2 <sup>nd</sup> Run		NON-IRRADIATED EXPOSURE																			
		0 Hrs			24 Hrs			72 Hrs			144 Hrs			240 Hrs							
	L(mg)	J(mg)	T(mg)	L(mg)	J(mg)	T(mg)	L(mg)	J(mg)	T(mg)	L(mg)	J(mg)	T(mg)	L(mg)	J(mg)	T(mg)	L(mg)	J(mg)	T(mg)			
<b>LPBF</b>	3636.7	2329.8	2641.1	3636.4	2329.5	2641.0	3636.1	2329.3	2640.7	3635.8	2329.0	2640.4	3635.4	2328.8	2640.1						
<b>AISI10</b>	3636.7	2329.8	2641.2	3636.4	2329.5	2641.0	3636.0	2329.2	2640.6	3635.7	2329.1	2640.5	3635.4	2328.8	2640.1						
<b>Mg</b>	3636.7	2329.8	2641.3	3636.4	2329.5	2641.0	3636.2	2329.2	2640.8	3635.7	2328.9	2640.4	3635.4	2328.8	2640.1						
	3636.7	2329.8	2641.3	3636.4	2329.5	2641.0	3636.0	2329.3	2640.7	3635.8	2328.8	2640.4	3635.4	2328.8	2640.1						
	3636.7	2329.8	2641.3	3636.4	2329.5	2641.0	3636.1	2329.3	2640.7	3635.7	2329.0	2640.5	3635.4	2328.8	2640.1						
	3636.7	2329.8	2641.3	3636.4	2329.5	2641.0	3636.1	2329.3	2640.7	3635.7	2329.0	2640.4	3635.4	2328.8	2640.1						
	<b>H(mg)</b>	<b>X(mg)</b>	<b>F(mg)</b>	<b>Y(mg)</b>	<b>H(mg)</b>	<b>X(mg)</b>	<b>F(mg)</b>	<b>Y(mg)</b>	<b>H(mg)</b>	<b>X(mg)</b>	<b>F(mg)</b>	<b>Y(mg)</b>	<b>H(mg)</b>	<b>X(mg)</b>	<b>F(mg)</b>	<b>Y(mg)</b>	<b>H(mg)</b>	<b>X(mg)</b>	<b>F(mg)</b>		
	4357.2	4500.2	3876.3	3814.9	4356.6	4499.6	3875.6	3814.5	4358.3		4501.2	3877.1	3816.1	4359.2	4502.5	3878.7	3817.8	4360.5	4505.3	3879.5	3819.3
	4357.2	4500.2	3876.3	3814.9	4356.6	4499.6	3875.6	3814.5	4358.3	4501.2	3877.1	3816.1	4359.3	4502.7	3878.8	3817.7	4360.7	4505.3	3879.5	3819.3	
<b>Cast</b>	4357.2	4500.2	3876.3	3814.9	4356.6	4499.6	3875.6	3814.5	4358.3	4501.2	3877.1	3816.1	4359.2	4502.2	3878.7	3817.6	4360.4	4505.3	3879.5	3819.3	
<b>A360.1</b>	4357.2	4500.2	3876.3	3814.9	4356.6	4499.6	3875.6	3814.5	4358.3	4501.2	3877.1	3816.1	4359.3	4502.3	3878.6	3817.7	4360.5	4505.3	3879.5	3819.3	
	4357.2	4500.2	3876.3	3814.9	4356.6	4496.6	3875.6	3814.5	4358.3	4501.2	3877.1	3816.1	4359.0	4502.6	3878.5	3817.8	4360.5	4505.3	3879.5	3819.3	
	4357.2	4500.2	3876.3	3814.9	4356.6	4499.6	3875.6	3814.5	4358.3	4501.2	3877.1	3816.1	4359.2	4502.5	3878.8	3817.9	4360.5	4505.3	3879.5	3819.3	
<b>Dimensions</b>	<b>L</b>	<b>J</b>	<b>T</b>	<b>Blank</b>	<b>H</b>	<b>X</b>	<b>F</b>	<b>Y</b>	<b>Blank</b>	<b>H</b>	<b>X</b>	<b>F</b>	<b>Y</b>	<b>Blank</b>							
	H(mm)	39.79	39.67	39.57	39.61	36.95	37.87	38.73	41.03	38.74											
	L(mm)	9.05	8.76	8.68	9.42	9.51	9.72	9.62	9.59	9.72											
	W(mm)	3.90	2.63	3.04	2.19	5.04	4.76	4.08	3.74	4.40											
	D(mm)	2.5	2.5	2.19	2.5	2.5	2.5	2.5	2.5	2.5											

NON-IRRADIATED EXPOSURE																
3 <sup>rd</sup> Run	0 Hrs			24 Hrs			72 Hrs			144 Hrs			240 Hrs			
	L(mg)	J(mg)	T(mg)	L(mg)	J(mg)	T(mg)	L(mg)	J(mg)	T(mg)	L(mg)	J(mg)	T(mg)	L(mg)	J(mg)	T(mg)	
	3451.2	2122.9	2446.8	3451.0	2122.7	2446.6	3450.8	2122.5	2446.3	3450.5	2122.2	2446.1	3450.2	2122.0	2445.9	
	3451.2	2122.9	2446.8	3451.0	2122.7	2446.6	3450.8	2122.5	2446.3	3450.5	2122.2	2446.1	3450.2	2122.0	2445.9	
<b>LPBF</b>	3451.2	2122.9	2446.8	3451.0	2122.7	2446.6	3450.8	2122.5	2446.3	3450.5	2122.2	2446.1	3450.2	2122.0	2445.9	
<b>ALSi10</b>	3451.2	2122.9	2446.8	3451.0	2122.7	2446.6	3450.8	2122.5	2446.3	3450.5	2122.2	2446.1	3450.2	2122.0	2445.9	
<b>Mg</b>	3451.2	2122.9	2446.8	3451.0	2122.7	2446.6	3450.8	2122.5	2446.3	3450.5	2122.2	2446.1	3450.2	2122.0	2445.9	
	3451.2	2122.9	2446.8	3451.0	2122.7	2446.6	3450.8	2122.5	2446.3	3450.5	2122.2	2446.1	3450.2	2122.0	2445.9	
	3451.2	2122.9	2446.8	3451.0	2122.7	2446.6	3450.8	2122.5	2446.3	3450.5	2122.2	2446.1	3450.2	2122.0	2445.9	
	<b>H(mg)</b>	<b>X(mg)</b>	<b>F(mg)</b>	<b>Y(mg)</b>	<b>H(mg)</b>	<b>X(mg)</b>	<b>F(mg)</b>	<b>Y(mg)</b>	<b>H(mg)</b>	<b>X(mg)</b>	<b>F(mg)</b>	<b>Y(mg)</b>	<b>H(mg)</b>	<b>X(mg)</b>	<b>F(mg)</b>	<b>Y(mg)</b>
	4119.0	4258.8	3650.9	3592.2	4118.8	4258.6	3650.7	3591.9	4119.6	4259.2	3651.4	3593.0	4120.8	4260.8	3653.1	3594.1
	4119.0	4258.8	3650.9	3592.2	4118.8	4258.6	3650.7	3591.9	4119.6	4259.2	3651.4	3593.0	4120.8	4260.8	3653.1	3594.1
<b>Cast</b>	4119.0	4258.8	3650.9	3592.2	4118.8	4258.6	3650.7	3591.9	4119.6	4259.2	3651.4	3593.0	4120.8	4260.8	3653.1	3594.1
<b>A360.1</b>	4119.0	4258.8	3650.9	3592.2	4118.8	4258.6	3650.7	3591.9	4119.6	4259.2	3651.4	3593.0	4120.8	4260.8	3653.1	3594.1
	4119.0	4258.8	3650.9	3592.2	4118.8	4258.6	3650.7	3591.9	4119.6	4259.2	3651.4	3593.0	4120.8	4260.8	3653.1	3594.1
	4119.0	4258.8	3650.9	3592.2	4118.8	4258.6	3650.7	3591.9	4119.6	4259.2	3651.4	3593.0	4120.8	4260.8	3653.1	3594.1
<b>Dimensions</b>	<b>L</b>	<b>J</b>	<b>T</b>	<b>Blank</b>	<b>H</b>	<b>X</b>	<b>F</b>	<b>Y</b>	<b>Blank</b>							
	H(mm)	39.63	39.35	39.25	39.60	36.64	37.59	38.27	40.91	38.69						
	L(mm)	8.86	8.50	8.51	9.40	9.38	9.55	9.49	9.40	9.62						
	W(mm)	3.79	2.52	2.92	2.17	4.87	4.61	3.95	3.59	4.32						
	D(mm)	2.5	2.5	2.5	2.5	2.5	2.5	2.5	2.5	2.5						

WEIGHTS OF DESCALED NON-IRRADIATED SAMPLES												
	1 <sup>st</sup> Run				2 <sup>nd</sup> Run				3 <sup>rd</sup> Run			
	L(mg)	J(mg)	T(mg)	Blank (mg) initial final	L(mg)	J(mg)	T(mg)	Blank (mg) initial final	L(mg)	J(mg)	T(mg)	Blank (mg) initial final
<b>LPBF</b>	4021.4	2760.0	3052.7	2156.4 2156.2	3634.9	2328.3	2639.7	2130.9 2130.6	3449.4	2121.6	2445.3	2123.2 2123.0
	4021.4	2760.1	3052.8	2156.5 2156.3	3634.8	2328.3	2639.5	2130.9 2130.7	3449.4	2121.6	2445.3	2123.2 2123.0
	4021.5	2760.0	3052.9	2156.6 2156.3	3634.9	2328.5	2639.7	2130.9 2130.6	3449.4	2121.6	2445.3	2123.2 2123.0
	4021.4	2760.1	3052.5	2156.5 2156.2	3634.9	2328.3	2639.7	2130.9 2130.7	3449.4	2121.6	2445.3	2123.2 2123.0
	4021.5	2759.9	3052.6	2156.5 2156.3	3634.7	2328.4	2639.6	2130.9 2130.6	3449.4	2121.6	2445.3	2123.2 2123.0
	4021.4	2759.9	3052.5	2156.5 2156.2	3634.9	2328.2	2639.7	2130.9 2130.7	3449.4	2121.6	2445.3	2123.2 2123.0
<b>Cast</b>	4897.2	4882.8	4332.4	4145.2 3292.1 3292.0	4350.9	4493.4	3870.3	3808.3 3291.9 3291.5	4112.7	4252.3	3644.8	3586.2 3283.9 3283.6
	4897.2	4882.6	4332.5	4145.2 3292.2 3291.8	4350.8	4493.7	3870.4	3808.5 3291.9 3291.5	4112.7	4252.3	3644.8	3586.2 3283.9 3283.6
	4897.2	4882.7	4332.6	4145.3 3292.1 3291.9	4350.9	4493.5	3870.2	3808.3 3291.9 3291.5	4112.7	4252.3	3644.8	3586.2 3283.9 3283.6
	4897.4	4882.8	4332.4	4145.3 3292.2 3291.9	4350.9	4493.7	3868.9	3808.5 3291.9 3291.5	4112.7	4252.3	3644.8	3586.2 3283.9 3283.6
	4897.2	4882.9	4332.4	4145.2 3292.1 3291.7	4350.7	4493.9	3870.2	3808.8 3291.9 3291.5	4112.7	4252.3	3644.8	3586.2 3283.9 3283.6
<b>A360.1</b>	4897.2	4882.7	4332.4	4145.2 3292.1 3291.9	4350.7	4493.7	3870.3	3808.5 3291.9 3291.5	4112.7	4252.3	3644.8	3586.2 3283.9 3283.6

		IRRADIATED EXPOSURE																													
1 <sup>st</sup> Run		0 Hrs						24 Hrs						72 Hrs						144 Hrs						240 Hrs					
		L(mg)	J(mg)	T(mg)	L(mg)	J(mg)	T(mg)	L(mg)	J(mg)	T(mg)	L(mg)	J(mg)	T(mg)	L(mg)	J(mg)	T(mg)	L(mg)	J(mg)	T(mg)	L(mg)	J(mg)	T(mg)	L(mg)	J(mg)	T(mg)						
	<b>LPBF</b>	3398.8	2090.6	2406.9	3398.5	2090.4	2406.6	3398.2	2090.1	2406.3	3397.8	2089.9	2405.9	3397.2	2089.3	2405.4															
	<b>AlSi10</b>	3398.9	2090.7	2406.9	3398.6	2090.4	2406.6	3398.2	2090.1	2406.3	3397.9	2090.0	2406.0	3397.2	2089.3	2405.4															
	<b>Mg</b>	3398.9	2090.7	2407.0	3398.6	2090.4	2406.6	3398.2	2090.1	2406.3	3397.8	2089.9	2405.9	3397.2	2089.3	2405.4															
	<b>Cast</b>																														
	<b>A360.1</b>	3953.6	4063.4	3452.9	3954.5	4064.9	3454.5	3955.3	4066.8	3456.6	3957.3	4069.1	3459.3	3959.7	4072.1	3462.8	3953.6	4063.4	3452.9	3954.5	4064.9	3454.5	3955.3	4066.8	3456.6	3957.3	4069.1	3459.3	3959.7	4072.1	3462.8
		3953.5	4063.4	3452.9	3954.5	4064.9	3454.5	3955.3	4066.8	3456.6	3957.3	4069.1	3459.3	3959.7	4072.1	3462.8	3953.6	4063.4	3452.8	3954.5	4064.9	3454.5	3955.3	4066.8	3456.5	3957.3	4069.1	3459.3	3959.7	4072.1	3462.8
		3953.6	4063.4	3452.8	3954.5	4064.9	3454.5	3955.3	4066.8	3456.5	3957.3	4069.1	3459.3	3959.7	4072.1	3462.8	3953.6	4063.4	3452.8	3954.5	4064.9	3454.5	3955.3	4066.8	3456.5	3957.3	4069.1	3459.3	3959.7	4072.1	3462.8
	<b>Dimension</b>	<b>L</b>	<b>J</b>	<b>T</b>	<b>Blank</b>	<b>H</b>	<b>X</b>	<b>F</b>	<b>Y</b>	<b>Blank</b>	<b>H</b>	<b>X</b>	<b>F</b>	<b>Y</b>	<b>Blank</b>																
		H(mm)	39.59	39.31	39.17	39.22	36.25	37.28	37.80	40.68	38.00																				
		L(mm)	8.84	8.41	8.43	9.08	9.28	9.46	9.29	9.22	9.59																				
		W(mm)	3.73	2.49	2.87	2.14	4.80	4.48	3.79	3.25	4.29																				
		D(mm)	2.5	2.5	2.5	2.5	2.5	2.5	2.5	2.5	2.5																				

**IRRADIATED EXPOSURE**

2 <sup>nd</sup> Run	0 Hrs			24 Hrs			72 Hrs			144 Hrs			240 Hrs				
	L(mg)	J(mg)	T(mg)	L(mg)	J(mg)	T(mg)	L(mg)	J(mg)	T(mg)	L(mg)	J(mg)	T(mg)	L(mg)	J(mg)	T(mg)		
LPBF AISI10 Mg	3297.9	2016.0	2327.4	3297.6	2015.7	2327.2	3297.2	2015.3	2326.8	3296.9	2015.1	2326.6	3296.5	2014.9	2326.3		
	3297.9	2016.0	2327.5	3297.6	2015.7	2327.2	3297.2	2015.3	2326.8	3296.9	2015.1	2326.6	3296.5	2014.9	2326.3		
	3297.9	2016.0	2327.5	3297.6	2015.7	2327.2	3297.2	2015.3	2326.8	3296.9	2015.1	2326.5	3296.5	2015.0	2326.4		
Cast A360.1	H(mg)	X(mg)	F(mg)	Y(mg)	H(mg)	X(mg)	F(mg)	Y(mg)	H(mg)	X(mg)	F(mg)	Y(mg)	H(mg)	X(mg)	F(mg)	Y(mg)	
	3809.4	3923.1	3305.5	2425.8	3810.1	3924.1	3306.7	2426.2	3810.9	3925.3	3307.9	2427.3	3814.2	3928.1	3310.4	2429.5	3816.2
	3809.4	3923.2	3305.5	2425.7	3810.1	3924.1	3306.7	2426.3	3810.9	3925.3	3307.9	2427.3	3814.1	3928.2	3310.4	2429.5	3816.3
	3809.3	3923.2	3305.4	2425.7	3810.1	3924.1	3306.7	2426.3	3810.8	3925.3	3307.9	2427.3	3814.2	3928.2	3310.4	2429.5	3816.3
Dimensions	L	J	T	Blank	H	X	F	Y	Blank								
	H(mm)	39.44	39.10	39.04	39.17	35.95	37.13	37.61	31.01	37.57							
	L(mm)	8.75	8.31	8.37	9.05	9.15	9.27	9.17	9.17	9.70							
	W(mm)	3.66	2.44	2.79	2.09	4.71	4.41	3.71	3.25	4.04							
	D(mm)	2.5	2.5	2.5	2.5	2.5	2.5	2.5	2.5	2.5	2.5	2.5	2.5	2.5	2.5	2.5	2.5

<b>IRRADIATED EXPOSURE</b>																				
<b>3<sup>rd</sup> Run</b>	<b>0 Hrs</b>			<b>24 Hrs</b>			<b>72 Hrs</b>			<b>144 Hrs</b>			<b>240 Hrs</b>							
	<b>L(mg)</b>	<b>J(mg)</b>	<b>T(mg)</b>	<b>L(mg)</b>	<b>J(mg)</b>	<b>T(mg)</b>	<b>L(mg)</b>	<b>J(mg)</b>	<b>T(mg)</b>	<b>L(mg)</b>	<b>J(mg)</b>	<b>T(mg)</b>	<b>L(mg)</b>	<b>J(mg)</b>	<b>T(mg)</b>					
<b>LPBF</b>	3189.5	1899.7	2233.9	3189.2	1899.3	2233.4	3188.9	1899.1	2233.2	3188.4	1898.9	2233.0	3188.2	1898.7	2232.7					
<b>AISI10</b>	3189.5	1899.8	2233.9	3189.4	1899.5	2233.6	3188.9	1899.1	2233.2	3188.6	1898.8	2233.0	3188.1	1898.4	2232.8					
<b>Mg</b>	3189.5	1899.5	2233.9	3189.1	1899.3	2233.7	3188.9	1899.1	2233.2	3188.7	1898.7	2233.0	3188.2	1898.6	2232.8					
	<b>H(mg)</b>	<b>X(mg)</b>	<b>F(mg)</b>	<b>Y(mg)</b>	<b>H(mg)</b>	<b>X(mg)</b>	<b>F(mg)</b>	<b>Y(mg)</b>	<b>H(mg)</b>	<b>X(mg)</b>	<b>F(mg)</b>	<b>Y(mg)</b>	<b>H(mg)</b>	<b>X(mg)</b>	<b>F(mg)</b>	<b>Y(mg)</b>				
<b>Cast</b>	3632.8	3789.3	3184.5	2316.4	3633.1	3789.7	3184.9	2316.8	3634.1	3790.8	3185.8	2317.7	3637.2	3794.0	3189.0	2319.8	3639.6	3796.4	3191.1	2321.7
<b>A360.1</b>	3632.7	3789.3	3184.5	2316.4	3633.1	3789.7	3184.9	2316.8	3634.1	3790.9	3185.8	2317.8	3637.2	3794.0	3189.0	2319.8	3639.5	3796.4	3191.1	2321.7
	3632.7	3789.3	3184.5	2316.4	3633.1	3789.6	3184.9	2316.8	3634.2	3790.8	3185.7	2317.8	3637.1	3794.1	3189.1	2319.7	3639.6	3796.3	3191.1	2321.6
<b>Dimensions</b>	<b>L</b>	<b>J</b>	<b>T</b>	<b>Blank</b>	<b>H</b>	<b>X</b>	<b>F</b>	<b>Y</b>	<b>Blank</b>	<b>H</b>	<b>X</b>	<b>F</b>	<b>Y</b>	<b>Blank</b>						
	H(mm)	39.33	38.88	38.93	39.08	35.83	36.73	37.30	30.65	37.29										
	L(mm)	8.65	8.15	8.24	9.01	9.00	9.17	8.95	9.04	9.65										
	W(mm)	3.60	2.33	2.75	2.06	4.50	4.34	3.67	3.19	3.54										
	D(mm)	2.5	2.5	2.5	2.5	2.5	2.5	2.5	2.5	2.5										



## Appendix B: pH of solutions containing cast A360.1 and LPBF AlSi10Mg

pH of Non-irradiated Exposure									
1 <sup>st</sup> Run	Time	pH	2 <sup>nd</sup> Run	Time	pH	3 <sup>rd</sup> Run	Time	pH	
LPBF AlSi10Mg	0	8.20	LPBF AlSi10Mg	0	8.20	LPBF AlSi10Mg	0	8.20	
	24	8.03		24	7.99		24	7.95	
	72	7.85		72	7.70		72	7.85	
	144	7.80		144	7.60		144	7.80	
	240	7.80		240	7.60		240	7.70	
Cast A360.1	0	8.20	Cast A360.1	0	8.20	Cast A360.1	0	8.20	
	24	8.15		24	8.00		24	8.10	
	72	7.96		72	7.80		72	8.00	
	144	7.96		144	7.77		144	7.95	
	240	7.90		240	7.70		240	7.90	
pH of Irradiated Exposures									
1 <sup>st</sup> Run	Time	pH	2 <sup>nd</sup> Run	Time	pH	3 <sup>rd</sup> Run	Time	pH	
LPBF AlSi10Mg	0	8.20	LPBF AlSi10Mg	0	8.20	LPBF AlSi10Mg	0	8.20	
	24	7.98		24	7.82		24	8.00	
	72	7.90		72	7.66		72	7.80	
	144	7.85		144	7.50		144	7.50	
	240	7.80		240	7.50		240	7.50	
Cast A360.1	0	8.20	Cast A360.1	0	8.20	Cast A360.1	0	8.20	
	24	8.00		24	7.90		24	8.00	
	72	7.95		72	7.80		72	7.92	
	144	7.90		144	7.78		144	7.82	
	240	7.90		240	7.75		240	7.70	



## Appendix C: NaI(Tl) Detector Peak Efficiency

**Table 3: Peak efficiency of a 3” x 3” NaI(Tl) detector**

Energy (keV)	Source-detector distance (cm)						
	0.1	1	3	5	10	20	30
15	0.996	0.993	0.989	0.987	0.990	0.991	0.991
20	0.990	0.986	0.980	0.982	0.985	0.987	0.988
30	0.974	0.972	0.967	0.969	0.975	0.980	0.980
33	0.872	0.863	0.869	0.873	0.881	0.884	0.886
35	0.837	0.828	0.828	0.835	0.841	0.844	0.848
40	0.831	0.829	0.838	0.842	0.851	0.857	0.857
50	0.840	0.851	0.861	0.864	0.877	0.880	0.882
60	0.853	0.867	0.879	0.887	0.897	0.903	0.905
70	0.867	0.885	0.894	0.899	0.910	0.917	0.920
80	0.882	0.897	0.899	0.903	0.917	0.926	0.929
90	0.891	0.903	0.903	0.908	0.921	0.933	0.936
100	0.899	0.907	0.902	0.904	0.917	0.934	0.939
150	0.908	0.886	0.841	0.849	0.879	0.911	0.924
200	0.881	0.809	0.756	0.761	0.808	0.864	0.885
300	0.735	0.636	0.578	0.596	0.657	0.726	0.760
400	0.587	0.496	0.451	0.468	0.532	0.600	0.638
500	0.485	0.404	0.364	0.383	0.437	0.503	0.538
600	0.407	0.339	0.308	0.323	0.377	0.436	0.463
700	0.351	0.291	0.267	0.283	0.327	0.382	0.411
800	0.316	0.256	0.239	0.253	0.290	0.338	0.368
900	0.283	0.229	0.211	0.225	0.264	0.310	0.336
1000	0.256	0.210	0.191	0.205	0.239	0.281	0.303
1100	0.236	0.191	0.178	0.190	0.221	0.260	0.280
1200	0.222	0.178	0.161	0.176	0.208	0.244	0.259
1300	0.201	0.168	0.152	0.160	0.191	0.223	0.245
1400	0.186	0.155	0.142	0.153	0.181	0.214	0.229
1500	0.180	0.145	0.131	0.138	0.168	0.202	0.218

Source: L Peralta [88].

## Curriculum Vitae

**Candidate's full name:** Victor Udochukwu Okoro

**Universities attended:** University of New Brunswick January 2021  
MSc.E Chemical Engineering (Nuclear option)

University of Lagos April 2014  
PgD., Chemical Engineering

Abia State University Sep. 2009  
BSc., Industrial Chemistry

### Publications:

V.U Okoro., D.H. Lister, L.Liu., and M. Mohammadi., Effect of  $\gamma$ -radiation on the corrosion of cast A360.1 versus selective laser melted (SLM) AlSi10Mg. (Poster and Paper), Proceedings of the 44<sup>th</sup> Annual Conference of the Canadian Nuclear Society, Saint John, NB, June 1 – 5, 2020. Virtual conference due to COVID-19.

V.U Okoro., D.H. Lister, L.Liu., and M. Mohammadi., Irradiation assisted corrosion of cast A360.1 and additively manufactured AlSi10Mg aluminum alloys in seawater environments. (In progress).

### Teaching Experience

UNB: Department of Chemical Engineering 2017 – 2020  
Instructed laboratory sessions for first and second-year undergraduate students in material science and unit operations (CHE 2506 and CHE 3434). Developed experimental runs, marked students' reports, supervision and grading.

### Industrial Experience

ORION Energy Services Limited. Lagos, Nigeria 2015 – 2016.  
Drug and Healthcare Limited Lagos, Nigeria 2013 – 2015.  
Neimeth International Pharm. Plc (formerly Pfizer Nigeria) Lagos, Nigeria  
2010 – 2012.  
Reservoir Fluid Laboratory (sub - Chevron Nigeria Ltd) Rivers, Nigeria 2008 – 2008.

## **Membership**

National Association of Corrosion Engineers (NACE).

Engineer-in-Training (EIT), Association of Professional Engineers and Geoscientists of New Brunswick (APEGNB).

Canadian Nuclear Society (CNS).

Toastmasters International.